N.Essaf

A case study of Pb-scaling in a geothermal project in the West Netherlands Basin

A case study of Pb-scaling in a geothermal project in the West Netherlands Basin

By

Najoua Essaf

in partial fulfilment of the requirements for the degree of

Master of Science
in Applied Earth Sciences

at the Delft University of Technology,
to be defended publicly on Thursday February 23th, 2023 at 14:00.

Supervisors:	Dr.ir. A.A.A. Hussain	
	Dr. J.S. Claringbould(Veegeo)	
	Prof. dr. K.H.A.A. Wolf	
Thesis committee:	Dr.ir. A.A.A. Hussain	TU Delft
	Dr. J.S. Claringbould,	Veegeo
	Prof. dr. K.H.A.A. Wolf	TU Delft
	Prof. dr. D.F. Bruhn	TU Delft

An electronic version of this thesis is available at http://repository.tudelft.nl/.

TU Delft

Acknowledgement

In my final years as a Master student at Delft University of Technology I spoke to several people in order to find a suitable MSc research project. I would like to thank prof. dr. Karl-Heinz Wolf for introducing me to such an interesting topic and providing me an opportunity to work at Veegeo.
I offer my sincerest gratitude to dr.ir. Ahmed Hussain for his constant and invaluable guidance during these period.
My great thankfulness to my thesis supervisors Prof. dr. Karl-Heinz Wolf, dr. Han Claringbould and dr.ir. Ahmed Hussain for their invaluable guidance and for reviewing my thesis. I am also very grateful to Ayla Reerink for her guidance and generous help in providing process data and sharing her knowledge. In addition, I am grateful to prof. dr. D.F. Bruhn who is a committee member of my MSc defense for reviewing my thesis and giving valuable comments.
Finally, I would like to express my appreciation to my parents, family and friends for their support during these years.

N.Essaf
Delft, February 2023

Abstract

This research was done in the framework of the RVO project on Development of a well impairment model for predicting geothermal clogging (DIMOPREC) .

The importance of developing new energy sources with lower carbon emissions than conventional hydrocarbon based energy sources has been globally recognized (Andrews-Speed, 2016). Geothermal energy is a lower carbon energy source, which can be used for both electricity production and for direct heat use (Fridleifsson, 2001).

However, radioactive mineral scaling can accumulate in filters and tubing of the geothermal facilities, which can be an operational hurdle as this scale needs to be removed with necessary caution. The problem is not only the riskiness of being exposed to radioactive elements, but also the rise in pressure caused by scale accumulation. This occurs at the filters resulting in more process stops. Another problem with the scaling is that it causes increasing injection pressure. Since there is a regulatory limit to this pressure, an increase in injectivity is not preferable. Here, a case of a low-enthalpy geothermal project is discussed where very limited radioactive galena, PbS, is found.

This geothermal system is modelled in the geochemical software package PHREEQC. The PHREEQC model shows that a fraction (78 wt.%) of the collected galena is produced in solid phase from the reservoir, and a smaller fraction (22 wt.%) is formed after the heat exchanger. Gamma ray logs analyses and sedimentation history are presented to find potential sources of Pb and S ions. With the geological history and literature study it is found that the radioactive Pb could be originated from the Zechstein and Rotliegend where it attaches strong to the Copper shale formations. Scale and water analysis show that most of the captured galena is transported in a solid phase into the geothermal facility.

In the second part we discuss the development of a SKID for scaling determination during geothermal production. It is proposed to design a new SKID with additional measurement and monitoring options, which is able to provide the requested input parameters for the PFREEQC model. Requested data acquisition for long term monitoring includes fluid pressure, flowrate, temperature and pH values. The mobile function makes it possible to sample at several surface locations along the line of the geothermal facility. The obtained and stored data can be analyzed and compared to other locations in order to find out whether or not the brine and its composition change, and if so, how it changes

In order to reduce the amount of radioactive PbS in the filters of the geothermal system, it could be considered to acidify the brine to a level where the minerals are dissolved. In addition, increasing the facility pressure and/or increasing the minimum brine temperature after the heat exchanger, could reduce the amount of galena precipitation captured in the filters of the geothermal facility.

Contents

Symbol list

Symbol	Unit	Explanation
A,B,C,D	-	Reactant species, only in eq, 1, 2, and 4
a,b,c and d	-	stoichiometric coefficients
l and m	-	Ionic charge
K_{sp}	-	Equilibrium solubility product
SI	-	Saturation index
IAP	-	Ion Activity Product
ΔG	J/mol	Gibbs free energy
R	8.314 J/mol·K	Gas constant
T	K	Temperature
E_a	J/mol	Activation energy
A	s^{-1}	Pre-exponential factor
k	s^{-1}	Reaction rate
P	bar	pressure
n	mole	Amount of moles
N_a	$6.022 \cdot 10^{23}$ $mole^{-1}$	Avogadro constant
ρ	g/cm^3	density
V	m/s	velocity
D	m	Inner diameter
μ	kg m^{-1} s^{-1}	Dynamic viscosity
C	mg/kg	Silica concentration
Re	-	Reynolds number
A_{bq}	s^{-1}	radiation
$t_{\frac{1}{2}}$	s	Half life

Table list

Figure list:

1. Introduction

1.1 Introduction into geothermal operations

The importance of exploiting energy sources with lower carbon emissions has been highlighted by the recognition of greenhouse gas emissions as a global security issue (Andrews-Speed, 2016). In the Netherlands, geothermal energy is an energy source with a total CO_2 (produced by pumps , gas flaring and in the water) emission estimated to be 80% lower in comparison to the use of a domestic gas boiler (Dijkstra et al., 2020). In the West Netherlands Basin, see Figure 1, during the period 2011 – 2021, geothermal energy exploration and development has grown and is providing heat to different purposes like the greenhouses. Oil and gas have been produced since the 1950s from Upper Jurassic to Lower Cretaceous strata. Now these formations with the Middle and Lower North sea group are targeted for geothermal exploitation (Willems et al., 2020).

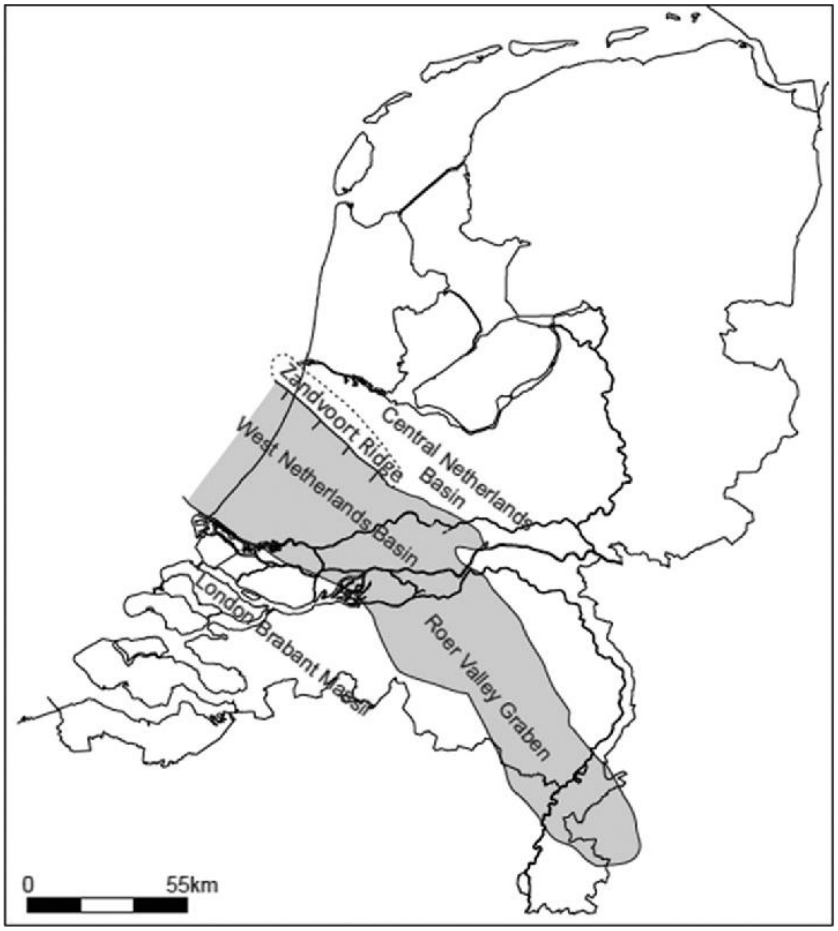

Figure 1: Geological setting of the West Netherlands Basin (Willems et al., 2020)

With geothermal-energy exploitation relatively warm water is produced from the subsurface, its heat is extracted by use of a heat-exchanger and the cooled water is re-injected. Geothermal energy is a renewable energy source because the re-injected colder water is heated by the internal heat flow inside the Earth. Due to its way of heating up the water it is at the same time a green and sustainable energy source. There is also a difference between high and low enthalpy geothermal systems. With low enthalpy geothermal systems water is at a temperature between 70 - 150°C, usually from formations shallower than 3 km (Martín-Gamboa et al., 2015). The extracted heat can be used for

several purposes, such as: heating buildings and heating bathing facilities. In the Netherlands it is mainly used to heat greenhouses although one project delivers heat to residential buildings (Haagse Aardwarmte Leyweg) (Bayer et al., 2012). A high enthalpy geothermal system refers to energy, which is generated from a depth over 3000m and a temperature over 150°C (Scott et al., 2016). These systems can be used to generate in a cascade electricity and heat. Low enthalpy geothermal systems are considered in this study.

As the produced water flows from the subsurface to the wellhead it undergoes a pressure decrease that result in expanding gas desorbing out of the solution, by that increasing the pH of the water. This process is intensified when the brine goes through the degasser (Andritsos et al., 2002). Subsequently the heat will be extracted from the produced water with the use of a heat exchanger, resulting in a lower water temperature. This change in temperature and pH can be a driver for several chemical reactions to occur in wells, surface facilities and near well bore areas (e.g., dissolution or precipitation of minerals). The forming of mineral scale can decrease the efficiency of geothermal operations (in the wells, surface facilities, tubing, heat exchanger or degasification sites)(Andritsos et al., 2002). A schematic overview of the geothermal facility can be seen in Figure 2.

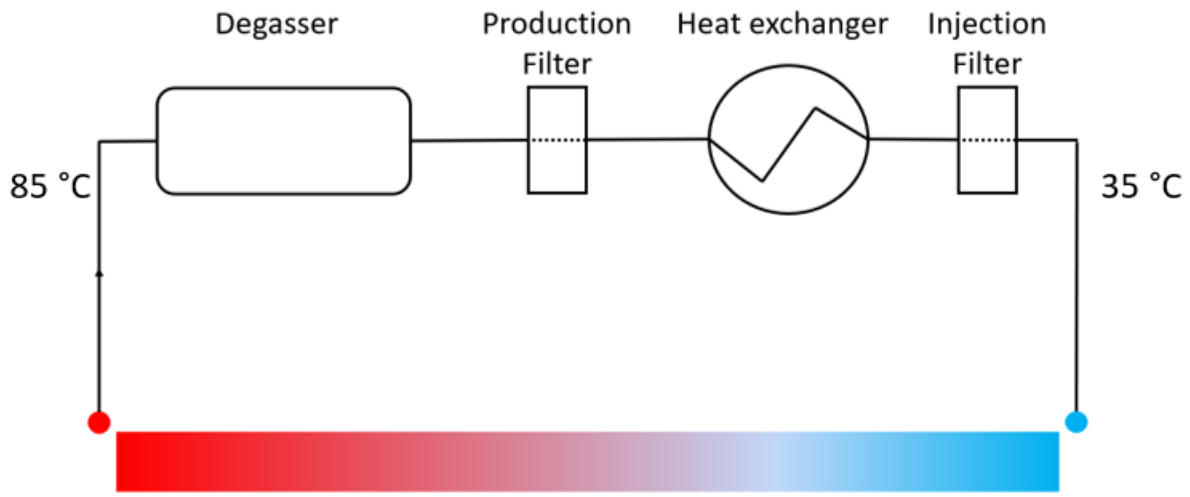

Figure 2: Schematic overview of geothermal process and facility.

On the red side of the figure, the hot brine water is pumped up from the reservoir. By extracting hot brine (85 °C), also some gas is transported to the surface. The gas will be removed with the use of the degasser. Afterwards it goes through the production filter bags, which filters out the solid parts larger than 5-micron meters. The heat exchanger then extracts the heat from the brine where after the cold brine goes through a second pair of “bag filters” (5 µm) and “injection candle filters” (1 µm) before being pumped back into the reservoir.

Mineral scaling has been recognized as a major obstacle in development of geothermal energy (Andritsos et al., 2002). Scaling can cause pore-blocking or narrowing of flow paths. Therefore, to maintain the desired injection flow rate the injection pressure needs to be increased, leading to more energy needed, and by that to higher pumping costs and possibility of error regarding the regulatory limitations of the injection pressure. Scaling in geothermal projects decreases the net amount of extracted energy and leads to the loss of power generation due to shutdowns. It can also lead to

additional expenses for solids/deposits removal and disposal or even abandoning a production or reinjection well due to clogging (Andritsos et al., 2002; V.N. Kashpura, V.V. Patopov, 2001).

Galena is a Pb-mineral that also may co-host various types of isotopes. Its' scale on well-tubing and in filter bags emits radioactive radiation (gamma ray), which must be limited under the regulations of the Dutch Environmental management activities scheme (*The System of Environmental Regulations in the Netherlands*, 2020). According to government regulations radioactive radiation needs to be below 1 kilo becquerel per kilogram (kBq/kg), and therefore radioactive scale needs to be removed frequently to stay below this limit.

Instead of only monitoring this scale and water flow at certain points of the surface facility, it would be exploratory to monitor with a mobile tool at several points. This is done by using the newly developed SKID. This SKID is connected parallel to the main flow system in the ground installation by means of a tubing branch; it consists of a frame, piping and a pump with various options to add measurement tools for physio-chemical data-acquisition, i.e., temperature, fluid flow (differential) pressure, conductivity, particle size analysis, etc. When doing theoretical modelling on fluid/tubing behavior it can be brought into practice with the SKID to see whether the model is in line with the practical results. In addition, small changes on tubing and tools can be implemented to monitor parameters which could not be measured at the regular facility monitor points. The SKID can be placed in the main line, in between the production and injection well, at various connection points.

1.2 Research questions, objectives and hypotheses

In this research the first focus will be on lead-scaling, specifically galena (lead (II) sulfide, PbS), which has been observed at a low-enthalpy geothermal plant in the production filters, injection filters and the injection tubing. The aim is to understand where it comes from and to develop a strategy to reduce radioactive lead scaling in a geothermal facility.

Therefore, the following question need to be answered:

How can lead-scaling (PbS) in the geothermal project of interest be mitigated?

I aim to confirm or reject the following hypothesis: a portion of the galena collected in the surface facility is transported from the reservoir into the facility in solid form and another portion of the collected galena is formed in the surface facility.

In order to do so, I investigate the significant sources of galena in the geothermal facility of interest:

1. Literature study: description of galena and the relevant geological history and genesis for lead oxides, lead sulfides and lead carbonites accumulation in the case-study area.
    a. What are the physical and chemical properties of galena?
    b. Regional geology/tectonics, reservoir geology and reservoir specific petrography/mineralogy
    c. Heavy metals association in the region: where has it been found before and how it is associated according to the literature.
    d. Indications of galena formation from the geological history of the case study area.
    e. Indications of radioactive lead and galena accumulation in the different reservoir formations.
    f. Can the weathering products of Galena be available in the closed system?

2. Geochemical modelling: what is the amount of galena produced within the facility and how to mitigate or reduce the amount of galena production in the facility
    a. What proportion of galena, collected in the surface facility, is transported from the original reservoir in solid phase?
    b. What is the impact of different processing parameters on galena precipitation and dissolution in the processing facility?
    c. Mitigation strategies based on influencing the reaction kinetics by changing the following parameters:
        i. pH upstream and downstream of the heat exchanger
        ii. Temperature of the re-injected water
        iii. Other chemical concentrations, upstream and downstream of the heat exchanger
        iv. Extracting the solid chemical formations by placing filters at several places in the model.
    d. Mitigation strategies based on filtration techniques or methods to physically isolate the relevant material
        i. What is the impact of filtering the geothermal water further upstream installation?
        ii. What is the impact of different filter mesh sizes on the collection of galena?
3. What is the correlation between the mineralogy of the reservoir formations and the mineral composition of the collected scale in relation to the physical and chemical properties, under pressure, volume, temperature, of the brine?

In order to recognize mineralization, a model needs to be made for changing pressure, temperature and pH values. The modelling software PHREEQC, which is used as the standard software within the Dimoprec project, can be used for the theoretical approach. In this study the system is a closed system, where cooling down takes place and radioactive scale occurs at filters and tubing.

The second focus, the practical approach, is placed on a tool to recognize the physio-chemical properties of the water; the SKID.

a. What are the specifications needed to measure the quality of brine at given temperatures?
b. What measurement features are needed?
c. How are the measurements done?
d. How are the measurements processed?
e. Are the outcomes in line with the PHREEQC model? If not, what causes the difference?

1.3 Thesis outline

This thesis consists of seven chapters, starting with chapter 1 as the introduction. In chapter 2, I present a literature study on scaling in geo-energy projects and the geological history of the case-study reservoir.

In chapter 3, I present the analyses of petrophysical logs, process and filter data. Gamma-ray logs are used to find indications for the layers from which the relevant species could be originated. In addition, I use the process and filter data from the geothermal plant at the surface to find out the amount of filtered scale and their composition at different locations along the line from the production to the injection well. Water analyses are also used as a start for water composition related mineral modelling in PHREEQC.

In chapter 4, I present my geochemical model of the geothermal case study by using PHREEQC. Here the geothermal case study is simulated to have a better overview and understanding regarding “if and where” minerals are created.

Chapter 5 presents the SKID and its applications: how to use it; what are the steps that need to be taken regarding the p, T-environment of measurements, and the specific dimensions and equipment to connect it to the tubing system.

In chapter 6 I compiled all the results of the different chemical and mineralogical analysis, geological history and the PHREEQC study. The simulations are also used to investigate different mitigation strategies. This is followed by the discussion in chapter 7.

In chapter 8 I present the conclusions and propose several mitigation strategies to reduce the amount of galena captured in the filters.

2. Literature study

2.1 Theory

Mineral dissolution and precipitation reactions occur simultaneously. A general form for a dissolution or a precipitation reaction is given in Eq 1. In this equation A and B are the reactant species, and AB is the product. C and d are the stoichiometric coefficients, and l and m are the ionic charges.

$$cA^{l+} + dB^{m-} \leftrightarrow A_cB_d(s) \qquad \text{Eq 1}$$

The equilibrium solubility product, *Ksp*, is the distribution at equilibrium of species which are stated on the right and left side of the reaction as stated in Eq 2 :

Eq 2

$$K_{sp} = \frac{[C]^c\,[D]^d}{[A]^a\,[B]^b}$$

The equilibrium solubility product is also an application of the law of mass action where the activity of a solid is equal to one (Appelo & Postma, 2005). Ion Activity Product, IAP, is the product of free ion species activities (Appelo & Postma, 2005);

Eq 3

$$SI = Log(\frac{IAP}{K_{sp}})$$

The Saturation index, SI, is a number to determine whether the water is corrosive or scaling. There are several possible outcomes for SI:

- If IAP< *Ksp* then SI is negative and it is thermodynamically favorable for the mineral to dissolve.
- If IAP>*Ksp* then SI is positive and it is thermodynamically favorable for the mineral to precipitate.
- If IAP= *Ksp* then SI is zero and the mineral is in equilibrium with solution.

The thermodynamic driving force for mineral precipitation is the change of Gibbs free energy of transfer from the supersaturated state to equilibrium (Eq 4).

$$\Delta G = RT * \ln\left[\frac{(A^{l+})^c(B^{m-})^{d\cdot}}{K_{sp}}\right]^{\frac{1}{c+d}} = RT\left[\frac{IAP}{K_{sp}}\right]^{\frac{1}{c+d}} \qquad \text{Eq 4}$$

Here *ΔG* is the Gibbs free energy [J/mol], *R* is the gas constant [8.314 J/mol·K] and *T* is the fluid temperature [K].

Mineral precipitation may occur whenever the ionic activity product of a solute exceed its equilibrium solubility product (Thomas & Gudmundsson, 1989). Here Eq 4 is used to calculate the super-saturation ratio of a dissolved mineral as a function of the *IAP* and K_{sp}. If the super-saturation ratio of a dissolved mineral, is higher than one, scale formation can occur (Andritsos et al., 2002)

In geothermal energy projects the water temperature decreases in the processing facility and impacts the reaction rates as described in Eq 5:

$$\log k = \left(-\frac{E_a}{R}\right)\left(\frac{1}{T}\right) + lnA \qquad \text{Eq 5}$$

Here k is the reaction rate [s^{-1}] ,E_a is the activation energy [kJ/mol] and A is a pre-exponential factor [s^{-1}] .This can be rewritten to Eq 6:

$$\log\left(\frac{k1}{k2}\right) = \left(-\frac{E_a}{2.303R}\right)\left(\frac{1}{T2} - \frac{1}{T1}\right) \qquad \text{Eq 6}$$

Where k_1 is the reaction rate at T_1 and k_2 is the reaction rate at T_2.

Besides, the solution composition and temperature, scaling reactions can be influenced by metal in contact with the solution. Well-tubing corrosion occurs when the casing material is steel (Hartog et al., 2002).

$$Fe \rightarrow Fe^{2+} + 2e^- \qquad \text{Eq 7}$$

Eq 7 shows the half reaction of iron oxidation. This Fe^{2+}-ion can both be originated from the geothermal aquifer and the casing. Fe^{2+} can further be oxidized by water to form, for example, iron minerals as shown:

$$Fe^{2+} \rightarrow Fe^{3+} + e^- \qquad \text{Eq 8}$$

When considering the presence of lead as ions and minerals it might react to other ions such as carbonate due to the free electrons. The free electrons of iron react with hydrogen ions and may create hydrogen gas. If lead-ions are present in the brine, then a competition reaction may create lead scale. Controlling corrosion, by using inhibitors, can mitigate a part of the problem with the piping system (Andritsos et al., 2002; Hartog et al., 2002).

Due to decrease of pressure and temperature during production, precipitation of galena may occur by super-saturation of PbS in H_2S bearing production fluids. Precipitation of metallic Pb is an electrochemical process, associated with corrosion of steel from production facilities. In this process, Pb^{2+} ions from production fluids react with electrons, liberated by dissolution of iron from steel installation parts. Corrosion potentials of $Pb^{2+}$and Fe^{2+} strongly depend, among others, on temperature and salinity of production fluids.

The main problem of the found scaling in this report is not only the lead scaling itself, but also the radioactive radiation it emits. A material containing unstable nuclei is considered to be radioactive.

The radioactive decay is the process by which an unstable atomic nucleus loses energy by radiation. Uranium is an element that decays into Thorium Radium, Polonium isotopes alternating to lead isotopes as can be seen in Figure 3 Other isotope series involves the decay of Potassium to Argon and Rubidium-Strontium. In essence, the unstable isotopes of these elements proceed the decay based on the half lifetime of the elements, resulting into production of α and β radiation. The radiation is measured and quantified in Becquerel. In order to have an overview of the radioactive weight percentage of these elements present in the analyzed filter-residues, the molar volumes representing the radioactive parts are calculated. This is based on a radiation-equation: $A_{bq} = n * N_a * \frac{ln2}{t_{\frac{1}{2}}}$, where A is the radiation [s-1], n represents the moles, N_a is the Avogadro constant [per mole] and $t_{1/2}$ is the half-life in seconds.

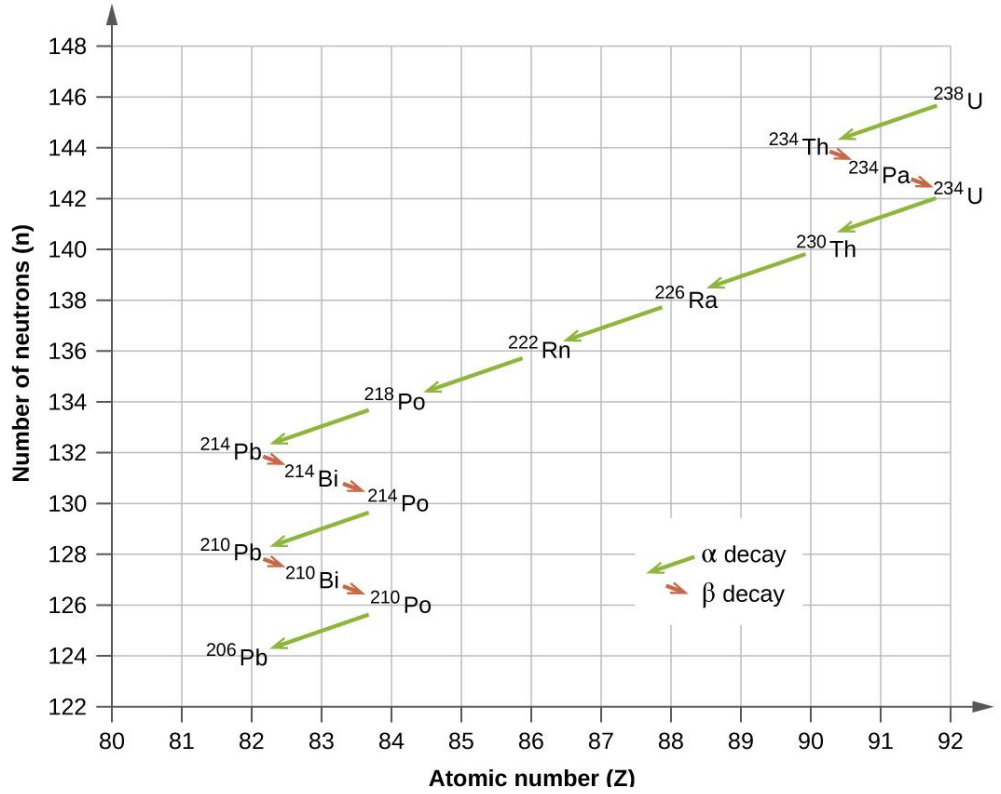

Figure 3: Radioactive decay series of Uranium to Lead (Paul Flowers, 2019)

- Several scale compositions might be generated, especially with a saltwater brine. Scale is positively influenced by pressure change, temperature changes and the presence of dissolved ions.

Table 1 presents the solubility of cations in water with the presence of anions. The degree of solubility of cations in water with dissolved anions is indicated with:

- B (bad), when the solubility is lower than 0.01 mol/L.
- M(moderate), when the solubility is between 0.1 and 0.01 mol/L.
- G (good), when the solubility is higher than 0.1 mol/L.

Table 1: Solubility degree of cations in water with dissolved anions (J.H.M. Beerens, 2015).

	OH^-	O^{2-}	CL^-	Br^-	I^-	S^{2-}	NO_3^-	CO_3^{2-}	SO_4^{2-}	PO_4^{3-}
Ag^+	-	B	B	B	B	B	G	B	M	B
Al^{3+}	B	B	G	G	G	-	G	-	G	B
Ba^{2+}	G	-	G	G	G	M	G	B	B	B
Ca^{2+}	M	-	G	G	G	M	G	B	M	B
Cu^{2+}	B	B	G	G	-	b	G	B	G	B
Fe^{2+}	B	B	G	G	G	B	G	B	G	B
Fe^{3+}	B	B	G	G	-	B	G	-	G	B
Hg^{2+}	-	B	G	M	B	B	g	B	-	B
K^+	G	-	G	G	G	G	G	G	G	G
Mg^{2+}	B	B	G	G	G	G	G	G	G	G
Na^+	G	-	G	G	G	G	G	G	G	G
NH_4^+	-	-	G	G	G	-	G	-	G	-
Pb^{2+}	B	B	M	M	B	B	G	B	B	B
Sn^{2+}	B	B	G	G	G	B	-	-	G	B
Zn^{2+}	B	B	g	G	G	B	G	B	G	B

There are different flow formulas that can be used to understand the flow pattern in the installation. Since most scaling can occur in bends of the installation, it is important to find out whether the flow is laminar, turbulent or in-between. The production brine in this report transports with a velocity of 6 m/s through the tubing, or, as can be said; with a velocity that we have a turbulent flow. However, with the following formula and the dimensionless Reynolds number, it can be determined whether it is laminar or turbulent. The flow state is also important for the SKID, since the flow inside the SKID tubing needs to be the same as in the installation in order to monitor differing circumstances. Otherwise, it may result in the generation of non-reliable measurements.
The formula used to calculate the Reynolds number:

Eq 9

$$Re = \frac{V * D * \rho}{\mu}$$

Here V is the velocity [m/s], ρ is the density [kg/m^3], D is the inner diameter [m] of the tube and μ is the dynamic viscosity [kg m^{-1} s^{-1}].

The Reynolds number has three ranges representing the state of flow:

- If Re ≤ 3000, then the flow is laminar.
- If 3000 ≤ Re ≤ 6000, then it is in transition area where both laminar and turbulent flow are present.
- If Re ≥ 6000, then the flow is turbulent.

2.2 Case studies

Several papers have been published on case-studies with scale deposition in geothermal reservoirs and geothermal plants. They can be used to be used to analyze the data for this case study (Andritsos et al., 2002; Thomas & Gudmundsson, 1989; Wanner et al., 2017) and to develop a specific theory for this site. In sections 2.2.1 to 2.2.4 carbonate, silica, sulfide and lead scaling case studies will be discussed in order to make an overview of scaling in general. Thereafter I will zoom in into specific lead scaling and relevant properties or aspects that affect development, i.e., precipitation/corrosion dependent pH values, temperature, ion concentrations and mineral related reaction rates.

The complexity of scale formation mostly depends on concentration fluctuations in aquifer water, rock compositions, facility compositions (tubing, filters, etc.), and process conditions (Hartog et al., 2002) .

Here we discuss the main contributors to scale formation, i.e., carbonates, sulfides and silica.

2.2.1 Carbonate scaling

Reservoir water interacts with reservoir minerals, where the minerals dissolve until reaching chemical equilibrium. The most common carbonate mineral-scales in geothermal projects are magnesium and calcium carbonate, mostly calcite, dolomite magnesite, and siderite (García et al., 2006). In smaller amounts, Whiterite and Strontianite, respectively the barium and strontium carbonate modifications, may be present. Eq 10 shows the equilibrium equation for the most occurring mineral calcium carbonate regarding its dissolution and mineralization:

$$CaCO_3(s) + H_2O + CO_2(g/aq) \leftrightarrow Ca^{2+}(aq) + 2HCO_3^-(aq) \qquad \text{Eq 10}$$

At the production well the pressure decreases, resulting in CO_2 gas desorption from solution, resulting in an increase of the pH, which stimulates calcite precipitation. In such a case, calcium-ions need little time to oversaturate, resulting into deposition of calcium oxide or calcite (Brown, 2013).

Overall, there are three basic methods for calcite scaling mitigation, i.e.:

- Calcite anti-scalant chemicals: anti-scalants react with calcium ions to make them less available to form calcite (Brown, 2013). Typical anti-scalants are polyacrylates, polymaleates, polycarboxylics, polyphosphonates, co-polymers or mixtures of these compounds depending on the chemistry of the brine. For these chemicals to work effectively, they must be present in the single-phase geothermal brine before it loses CO_2 (calcite starts to form). This method is therefore only used in the installation before degasification. It has no significant effect when injected into reservoir formation, where multiple phases (rock, gas and liquid) are present.

- Mechanical removal: this method can be used when scaling occurs in the production and injection wells. If it is possible to clean the facility tubing it is also possible in the processing plant. Periodic maintenance stops are needed in order to clean out the well casing and remove calcite deposition. This is done by scraping the tubing and mechanically removing the rubble from the wells. This method increases the borehole diameter, reduces the resistivity of the walls and by that improves flow rates. It is less cost effective than the use of an anti-scalant because of a temporary stopover.

- Controlling pH value: this includes lowering the pH value by adding additives and limiting pH changes on the processing facility. Lowering the pH can be done by acidifying the solution. It is mostly used as a reservoir stimulation method in calcite rich reservoirs. Calcite dissolution is promoted by a lower pH, for which hydrochloric acid is commonly used (Brown, 2013). However, the use of this mitigation method requires specialized equipment. It is also possible to control the pH by limiting the extent of degassing (Thomas & Gudmundsson, 1989).

2.2.2. Carbonate scaling: Examples from geology

Calcite in the Bavarian Molasse Basin

From 1995 to 2014 the Bavarian Molasse Basin, a clastic area in southern Germany, has become a popular spot for geothermal power production, having 22 geothermal power plants (Mayrhofer et al., 2014). The thermal reservoir for these plants is the Upper Malm aquifer in the Upper Jurassic age, having a maximum reservoir temperature of 150 °C at 4-5 km depth. Despite the favorable reservoir conditions, challenges occur because of calcite scaling ($CaCO_3$) in the wells and at the heat exchangers. It is found that decompression with degasification of mainly CO_2 resulted in a higher pH value, which lowers the calcite solubility significantly. In this case, the conditions for scaling have been found near the downhole pump (Wanner et al., 2017).Since minor calcite scaling have been triggered by fluid decompression within the production well, it is concluded that the abundant scaling along the pump casing is due to cavitation induced by operating the pump at high production rates. Lowering the production rates would affect efficiency but decrease scaling along the pomp casing.

Calcite precipitation at the Kızıldere Geothermal Power Plant

The fluid chemistry at the Kizildere power station in Turkey shows that if the water is allowed to degas, the produced water becomes supersaturated with calcite. The area is a sedimentary basin in a graben structure, heated by a granite intrusion. The main reservoir includes carbonate rich shale zones and fractured marble. It was found that cooling the water under higher pressure can prevent super saturation of calcite (Thomas & Gudmundsson, 1989). From a field test it was found that adding phosphonate inhibitor with a concentration in the range of 10 ppm to 200 ppm in the brine could control the calcite precipitation (Thomas & Gudmundsson, 1989, Pierie et al. 1989).

2.2.3 Silica-scaling

Production water is cooled down, degassed and re- injected, when it flows again through reservoir rocks, warms up, and is eventually produced again at the production well. During reheating, the increase in temperature may result in a change of solubility for several minerals. Many reservoir rocks consist (partly) of sandstones and shales, containing different silica minerals, such as quartz, feldspar, illite, kaolinite and smectite. The most common sandstone mineral is quartz. Quartz dissolves in water and forms silicic acid (H_4SiO_4) at higher temperatures. The reaction describing the equilibrium equation of dissolving/precipitating quartz is:

$$SiO_2(s) + 2H_2O \leftrightarrow H_4SiO_4(aq), \quad \text{Eq 11}$$

where silicic acid can dissociate into hydrated ions:

$$H_4SiO_4(aq) \leftrightarrow H_3SiO_4^- + H^+ \quad \text{Eq 12}$$

The solubility of quartz between 20 to 340°C has been described by Fournier (1986) in the following equation, where T stands for temperature in Kelvin, and C for silica concentration (mg/kg):

$$T = -42.196 + 0.28831 * C - 3.6685x10^{-4} * C^2 + 3.1665x10^{-7} * C^3 + 77.034 * \log C \quad \text{Eq 13}$$

Silica precipitation at the surface often occurs as an amorphous state, which highly soluble when compared to solid crystalline quartz (Brown, 2013). The solubility of amorphous silica is described as:

$$\log C = -\frac{731}{T} + 4.52 \quad \text{Eq 14}$$

To predict silica scaling, the silica saturation index (SSI, present silica concentration divided by equilibrium concentration) is used; for SSI<1.0 no silica scaling will occur. Silica deposits can be formed within minutes or hours after supersaturation conditions are reached. Moreover, the deposition of amorphous silica-hydrates is controlled by polymerization kinetics of silicic acid (Rimstidt, 2014).

Mitigation strategies for silica scaling in high enthalpy geothermal operations.

Two mitigation strategies are:

1. The key for preventing or decreasing silica precipitation when performing high-enthalpy geothermal operations is to keep the brine temperature high (T>171 °C) or separate the geothermal fluid above this temperature before going through the heat exchanger.
2. By extracting the silica from the liquid phase of the geothermal fluid, the productivity increases of the heat carrier as well as reduction of solid deposition growth rate in geothermal installations or wells (Kashpura, Patopov, 2001).

2.2.4 Silica scaling: Examples from geology

Verkhne-Mutnovsk geothermal power station

The high temperature reservoir is situated in an active volcanic sub-arctic region on the Kamtsjatka peninsula – Russia. Instead of keeping the temperature high (T>80 °C) to favor solubility, it is also possible to do the exact opposite. In the geothermal power station, the precipitation of silica from the geothermal brine was controlled by freezing it to approximately 5°C locally by using a snow cover. By using this method silica occurs within a designated section of the facility, where it is collected and removed from the installation (Mroczek et al., 2017). Afterward, the produced water is injected again.

Wairakei and Ohaaki Geothermal Fields in New Zealand

These fields are in an active volcanic region at two extending plate margins on the north island of New Zealand. In these fields cooling and aging of silica saturated geothermal water is done with the intention of controlling silica scaling. Several experiments were undertaken to measure the silica scaling and to find safe disposal options. At the Wairakei geothermal field injection of cold, 30 °C, geothermal water was undertaken. Their experiment showed a decrease of silica precipitation by cooled separated geothermal water at the analyzed locations. The geothermal water in Ohaaki was

cooled more rapidly in comparison with Wairakei, however, more silica scaling was observed in Ohaaki. After this result, the injection trial was only done at Wairakei. Their injectivity index did not change over a the period of testing, indicating that scaling did not occur within the injection well and near wellbore area during injection (Ed Mroczek et al., 2017).

2.2.5 Sulfide / sulfate scaling

Sulfide bounded scale formation is encountered at various geothermal projects (Andritsos et al., 2002). It is found in a smaller mass quantity than carbonate scale, however, compared to carbonate scale, it may cause more problems because sulfides bond with heavy metals such as lead. Heavy metals in large amounts can be toxic and harmful for people, animals and soil. Significant quantities of heavy metal sulfide scales are commonly (not only) seen as a result of fast pressure reduction (Owen & Michels, 1984). Metal sulfide scales are soluble at high temperatures, high pressures, and low pH values (Saidoun et al., 2016). Because of the fast pressure reduction, degasification of the produced water results in removal of CO_2 and H_2S, and by that causing an increase of the pH value of the solution (Andritsos & Karabelas, 1991; Brown, 2013; Owen & Michels, 1984).

The sulfides can also react with iron of the well casing and tubing, where the following half reaction can occur:

Eq 15

$$Fe^{2+} + HS^{-} \rightarrow FeS + H^{+}$$

In addition, oxidation of sulfides may induce reactions with heavy metals, such as radioactive lead.

2.2.6 Sulfide/sulfate scaling: Examples from geology

The Milos plant in Greece

The Milos Plant uses a low enthalpy volcanic geothermal reservoir. The reservoir water mostly consists of original seawater and volcanic fluids. Geothermal brine with seawater flows through the volcanic reservoir, which is full of minerals. Due to convection of warm seawater with deep fluids, leaching of rocks, seawater ions and the subsurface salts dissolve and flow with the produced water to the surface.

In this plant the solubility of galena (PbS) decreased by approximately 50 times as a result of decreasing the pH value with one order of magnitude (Helgeson, 1969). Harrar (1981) shows the relation between pH reduction of the Milos geothermal brine and the solubility of metal sulfides in high salinity solutions. This relation is illustrated in Figure 4 and shows that the solubility decreases with an increasing pH and decreasing temperature for ZnS and PbS. The solubility of FeS does stay constant with changing temperature. Copper is often a major component in sulfide scaling and in association with minor amounts of zinc and lead as sulfides it can be economical for mining (Brown, 2013). Anhydrite ($CaSO_4$) scaling has also been observed in production wells as a result from mixing of deeper high calcium containing brines with shallower sulfate-rich fluid (Brown, 2013).

4A

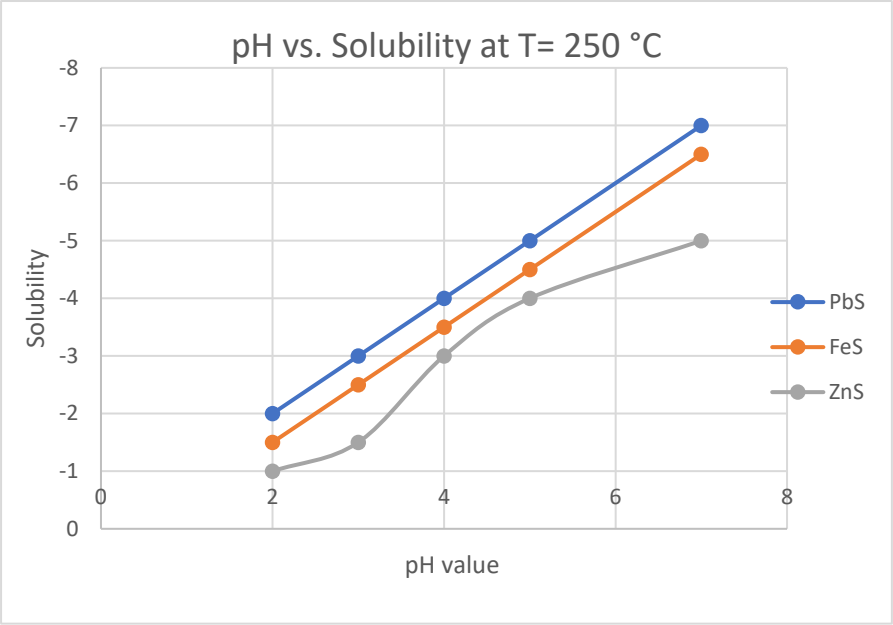

4B

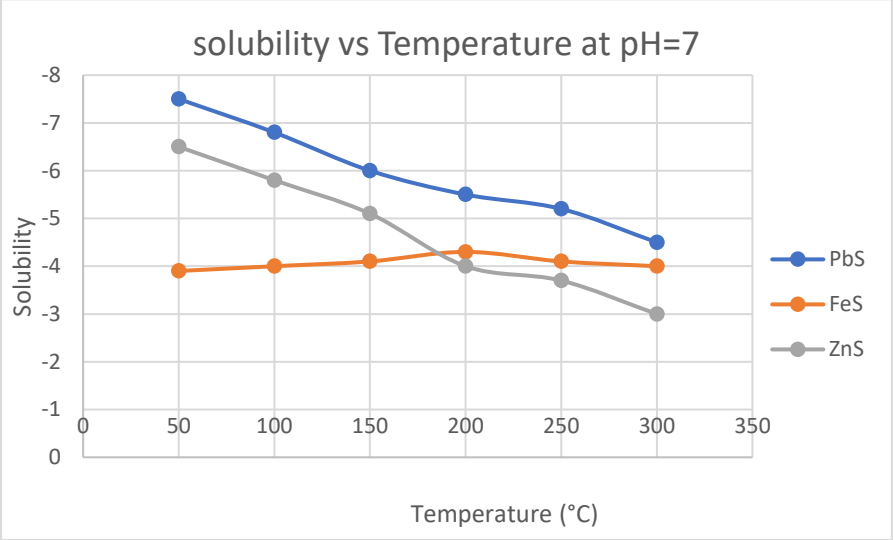

Figure 4: Relation between (A) Solubility and pH (T=250 °C) ,(B) Solubility and temperature (pH=7) (Andritsos et al., 2002)

Geothermal fields in Iceland

Sulfide scaling occurs in Iceland on both Reykjanes and Krafla fields. Both fields are high-temperature geothermal areas in Iceland. The system is a spreading zone with much volcanic and tectonic activities.

Reykjanes field is located in South-West Iceland. It is the subaerial continuation of the Reykjanes Ridge section of the Mid-Atlantic Ridge, and the boundary between the European and American tectonic plates (Altamirano, 2006). Reykjanes is a high enthalpy geothermal field. It is a liquid dominated system with a brine constitution Influenced by seawater. The usual initial reservoir temperature is over 295°C. Iron, Zinc and Copper sulfide scales were observed in the wells. These precipitations blocked the wells (Hrefna Kristmannsdttir, 1989).

Krafla is located in North-East Iceland and is characterized by glacier-based water. The Krafla volcanic system forms part of the Northern volcanic rift zone in Iceland, which is a N-S trending region of active spreading along the axial rift boundary between European and American plates. Iron-silicates precipitated from the magmatic rock and changed the geothermal fluid in the Krafla field. In addition, metallic sulfides and oxides were also present in the scales blocking the wells. In one of the wells scales are found consisting mainly of: quartz and cristobalite, pyrite (FeS_2), magnetite (Fe_2O_4) and anhydrite ($CaSO_4$). Iron sulfides are most common from 1550 to 1700 m depth and the iron oxides are dominant in the bottom 300 m. Pyrrhotite is the dominant iron sulfide phase in the scales in KJ-7.

The main solution for scale in the wells is the injection of amine corrosion inhibitors at the production side of the facility to prevent corrosion of the casing with the other advantage of preventing formation of metal sulfides (Honegger et al., 1989).

Lead Sulfide scaling the Permian

Lead scaling may include radioactive nuclides such as Pb-210, that are a hazard to health and environment. Not only geothermal operations have lead scaling, natural gas production from Dutch Rotliegend and Coppershale sediments also create sulfate scale original from lead deposits (Hartog et al., 2002). The serious threat is when it tends to block production equipment, injection pumps or tubing. The concern about Pb-210 is that it might precipitate at concentration levels above regulatory allowed values.

Hartog et al., (2002) explains the presence of galena, PbS, by local supersaturation where bisulfide anions react with lead cations in the produced water. The supersaturation is caused by a sudden drop in temperature and an increase in pH. It was also observed that corrosion of the tube walls influences the oxidation of lead ions in the solution resulting in more deposition of lead scales.

Their recommendation is to use pipes with a chromium coating to prevent redox reactions. Another option is the application of an electric potential high enough to prevent electron transfer of iron to lead ions.

Lead scaling in a geothermal project producing from the Slochteren formation in the Netherlands also experiences lead scaling (P.M.M.C. Bressers & F. Wilschut, 2014). By using corrosion inhibitors, the prevention or decrease of lead scaling was made possible. Material selection of the installation is also a way to reduce precipitation. Concentration of the deposits by absorption of anodic/cathodic protection is an option. However, there has to be taken care of the disposal of radioactive deposits.

Lead scale in the Nanmushu plant, China.

Nanmushu is a large Mississippi Valley-Type (MVT) Zn-Pb deposit in recent years discovered on the northern margin of the Yangtze block. The deposits formed by diagenetic recrystallization of carbonates creating low-temperature hydrothermal solution that migrates to suitable stratigraphic traps like fold hinge and faults at the continental margin and intra-cratonic basin setting (J.J. Wilkinson, 2014). In the dolostone formation of the Ediacaren Denying Zn-Pb deposits are found in combination with bitumen. The Zn-Pb deposits were horizontally located above and below the hydrocarbon reservoir.

In order for Zn-Pb mineralization to occur, ore metals from the reservoir were provided through the formation. The big drive behind Zn-Pb mineralization could be the result of the destruction process of

the hydrocarbon reservoir and the transformation from paleo oil to paleo gas reservoir. Decompression and cooling during the paleo-gas reservoir destruction may have formed extensive metal sulfide precipitation and mineralization (Huang et al., 2021).

In cases like this, where deep burial of palea-oil reservoir has occurred, there is no clear solution to reduce the amount of lead scaling because of the enormous mineral supply in the reservoir. The best way would be to have a well, which is not that deep (and not in the same reservoir) or replacing the wells to a field with geothermal qualified circumstances without the same geological background.

2.2.7 Scale mitigation methods based on geological examples

After discussing the different kinds of scaling in different geological settings, with different chemical compositions, here I present common scale minimizing solutions.

- Chemical removal of scale in an installation (Brown, 2013)
- Controlling pH value of the brine (Brown, 2013; Thomas & Gudmundsson, 1989)
- Using calcite anti-scalant (in case of having calcite scaling) (Brown, 2013)
- Lowering the production rates would affect the efficiency but decrease scaling along the pomp casing(Wanner et al., 2017)
- Adding inhibitors dependent on the brine (Andritsos & Karabelas, 1991; Hartog et al., 2002)
- Increase the minimum brine temperature (V.N. Kashpura, V.V. Patopov, 2001)
- Separate the geothermal fluid (V.N. Kashpura, V.V. Patopov, 2001)
- Controlled brine freezing and removing the scale afterwards from the installation (Ed Mroczek et al., 2017)
- Controlling concentration of the deposits by absorption of anodic/cathodic protection is an option (P.M.M.C. Bressers & F. Wilschut, 2014)

However, the mitigation methods depend on the brine, minerals, chemical composition, pressure, temperature, pH value and geological history (volcanic, burial, diageneses, tectonic etc.).

2.3 Geological history

Our case-study field is located in the Dutch province “South-Holland” within the West Netherlands Basin (WNB). The WNB is bound by the following geological structures: Zandvoort ridge, Roer Valley graben, Broad Fourteens basin and London-Brabant Massif as can be seen in Figure 5. The geological elements have been continuously changing in response to changing tectonic conditions. Van Balen et al. (2000) divided the tectonic history of the West Netherlands Basin into four stages from the Late Carboniferous to the Tertiary (350 Ma- 66 Ma)(van Balen et al., 2000).

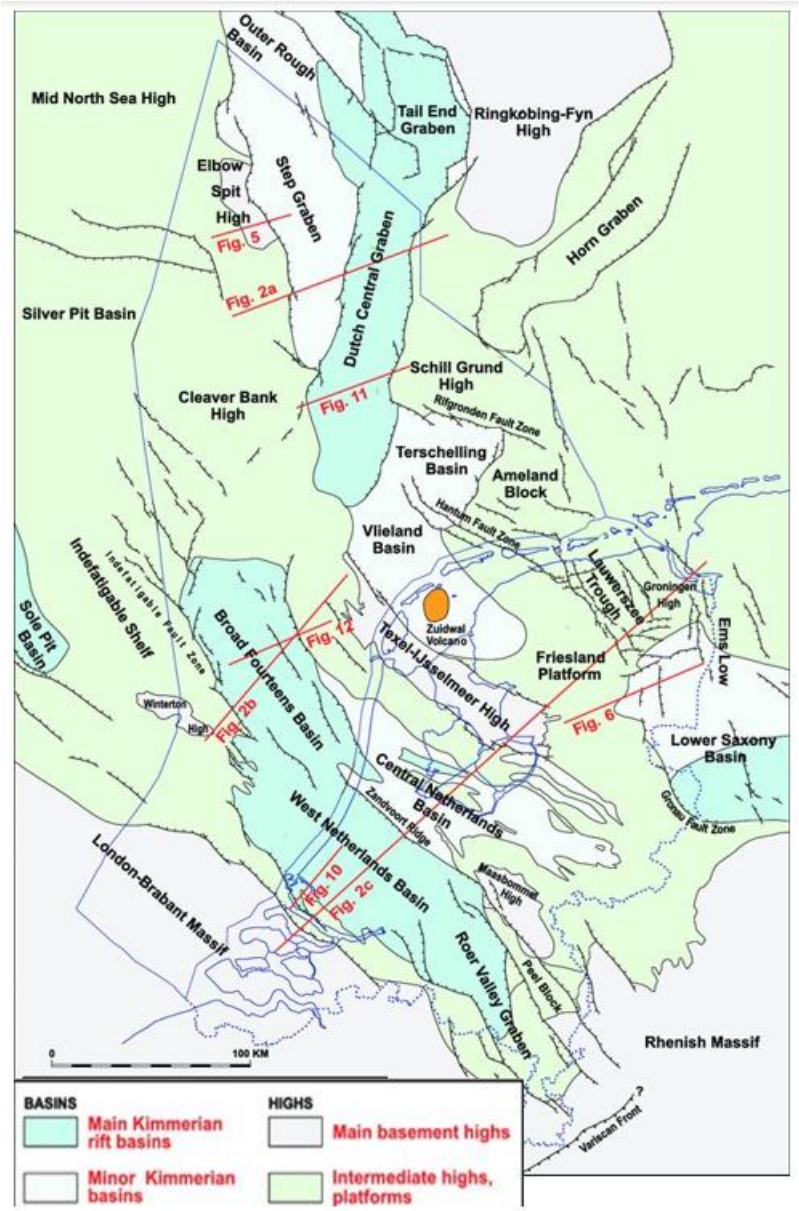

Figure 5: Basin overview in the Netherlands. (De Jager, 2007)

Late Carboniferous Early Permian stage (350 Ma- 300Ma)

The Mesozoic WNB is of Variscan origin and developed upon the Campine Basin. The basin is situated north of the London-Brabant Massif and displayed strong subsidence from the Namurian onwards (Langenaeker, 2000). This was followed by an uplift and erosion that took place during the Variscan orogeny from the Westphalian to the Early Permian. Up to 500m of sediments were eroded around the Zandvoort Ridge, which can be partly explained by the strong uplift it experienced. The Late Carboniferous basin was filled with a predominantly fine-grained succession, compromising a basal hot-shale and coal-bearing strata in the middle part (Adrichem-Boogaert & Kouwe, 1993).

Late Permian – Middle Jurassic 'early syn-rift' stage (300 Ma- 260 Ma)

During the Late Permian, sedimentation resumed and the WNB formed a stable block. The sedimentation consists of fluvial and aeolian sandstones, clay stones, siltstones and carbonates. During the Late Permian rift pulse the basin was uplifted followed by regional thermal subsidence in the Early

Triassic. The WSB (West Siberian Basin) got a deposition of lacustrine sediments followed by fluvial and aeolian successions derived from the London-Brabant Massif and was dipping gently northwards. Tectonic movements occurred during the Early Kimmerian tectonic phase (Middle to Late Triassic) and made the WNB form a structurally regular, large-scale half-graben. In the Early Jurassic, faulting caused differential subsidence of various subunits of the basin (van Balen et al., 2000).

Late Jurassic – Early Cretaceous 'synrift' stage (200 Ma- 145 Ma)
During the Late Jurassic to Early Cretaceous the strongest lifting occurred causing the breaking-up of the basin into subunits. The rifting occurred on several discrete pulses of short duration in timespan from Kimmeridgian to Barremian. The highs in the basin were uplifted and eroded during the Middle Jurassic and Early Cretaceous rifting phases, while the basins accumulated very thick syn-rift sediment packages (de Jager, 2007). Igneous activity accompanied the rifting, as is evidenced by the occurrence of volcanic rocks and intrusive sills (de Jager, 2007). The subsidence of the WNB continued into the Late Cretaceous (van Balen et al., 2000).

Late Cretaceous – Quaternary 'post rift' and inversion stages (100 Ma- 2.5 Ma)
The syn-rift phase has stopped in this period. The WNB was then located in the hinterland of the Alps where inversion resulted in a peak in its stresses. As a result of the compressive forces during the Alpine orogeny inversion has occurred in the WNB. The inversion also caused uplift of layers and sedimentation was limited to marginal troughs that formed to the north and south of the basin. Mayor fault zones display reverse movements. Many hydrocarbon-bearing structures have been formed in this phase. Afterwards, during Maastrichtian-Danian, the whole basin was covered by sediments because of ceasing inversion movements. Renewed uplift occurred again during the end of early Paleocene and Eocene-Oligocene resulting in removal of all Paleogene sediments. The uplift was followed in the Neogene by another subsidence phase (van Balen et al., 2000).

During all these geological deformations the subsurface changed. Faults, inversion, uplift, erosion, and sedimentation were all factors that played a big role in transportation of metals within organic material. Organic material can be found at the Aalburg Formation (200 Ma). This formation consists of a sequence of dark grey, occasionally calcareous, locally silty to sandy clay stones containing occasional thin argillaceous limestone beds. Heavy metals have the behavior of adsorbing to organic material. When brine with dissolved metals flows through the formation, the metals can be transported to the geothermal installation.

The Cretaceous in the Netherlands represented by the Marine, Early Cretaceous Rijnland Group and Late Cretaceous to Earliest (100 Ma) Chalk Group. The rifting tectonics of the Jurassic changed into regional subsidence. As a result of rising sea level, the sedimentation, previously restricted to the basins, extended over the adjacent platforms and highs. This long-term transgression was not continuous; sea level fluctuation resulted in various transgressive basal sands or pro-grading coastal-barrier sands of the Vlieland Sandstone Formation. During the Late Cretaceous, the influx of fine grained clastic into the marine realm diminished. A fairly uniform succession of marls and limestone of Texel and Ommelanden formations developed. Numerous oil and gas fields produce from lower cretaceous sandstones. In contrast, only one oil field and one gas field are produced from the Chalk Group. A few quarries and aquifers in Cretaceous rocks locally yield limestone for cement production and water, respectively.

When the Valanginian (139 Ma) transgression simultaneously reached the Vlieland, the first transgressive and coastal barrier sands of the Vlieland Sandstone were deposited.

The WMO, Waterleiding Maatschappij Overijsel, derives parts of this groundwater from Bentheim and Gildehaus sandstones. The permeabilities of these sandstones vary significantly, depending on the sedimentological properties. Most of the groundwater was retrieved from the south of the Netherlands at the chalks.

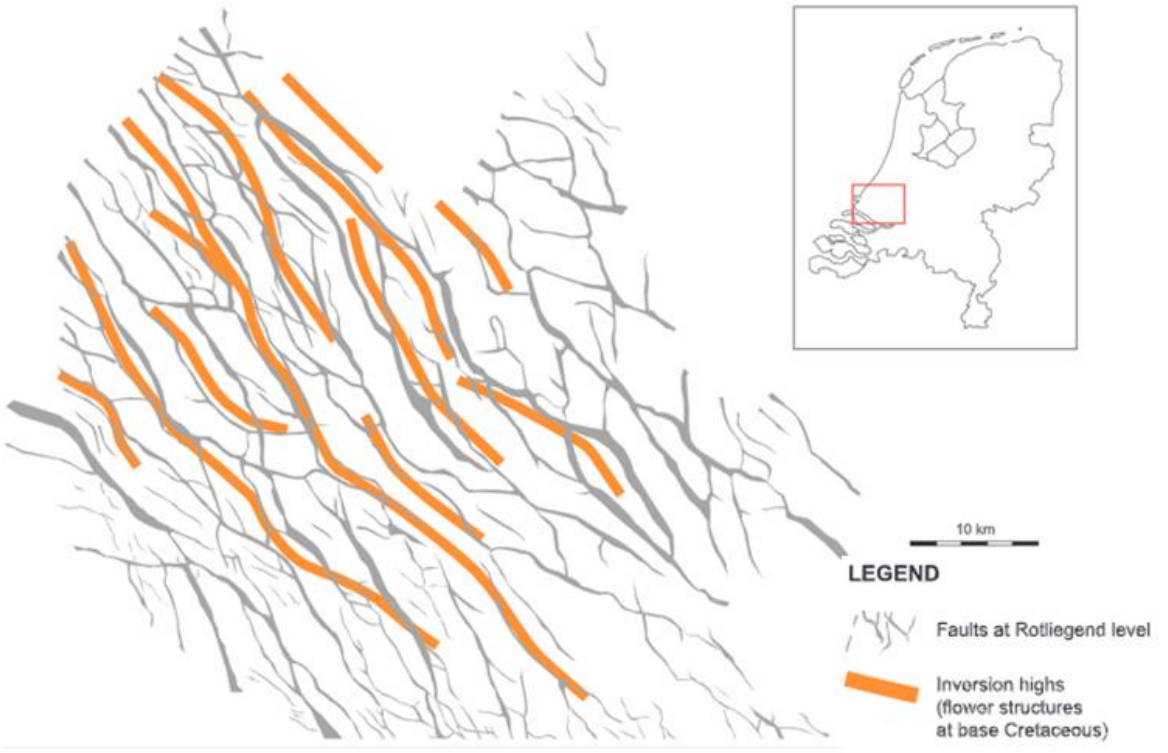

Figure 6: Fault pattern at Rotliegend Leves. West Netherlands Basin based on 3D seismic data (Wong et al., 2007)

During the Late Cretaceous compressional flower-structures were formed through reactivation of both NNW-SSE and WNW-ESE fault trends. What at first sight looks like an alignment of continuous flower structures at Cretaceous levels, can be seen to follow different fault trends at Rotliegend level. Changing from the one to the other as can be seen in Figure 6. Apparently, none of the pre-existing fault trends was ideally oriented to be preferentially reactivated. Therefore, present-day fault trends cannot be really interpreted in terms of paleo-stress directions. Reliable indicators to determine the accumulated amount of lateral displacement are rare. It is impossible to unravel amount of displacement during the various evolutionary phases of individual faults (de Jager, 2007).

Zooming in on the area of interest two cross sections are made. One from north to south and the other from east to west. These figures can be found in Appendix I. As can be seen in Figure 7 the area of interest (4-6 km on the x-axis), there is an anticline structure at a depth of 3300m. Some nearby faults can be seen on these cross sections near the case study area. Because of the wide step ranges 50-100m it is not too precise to see the faults present in that area.

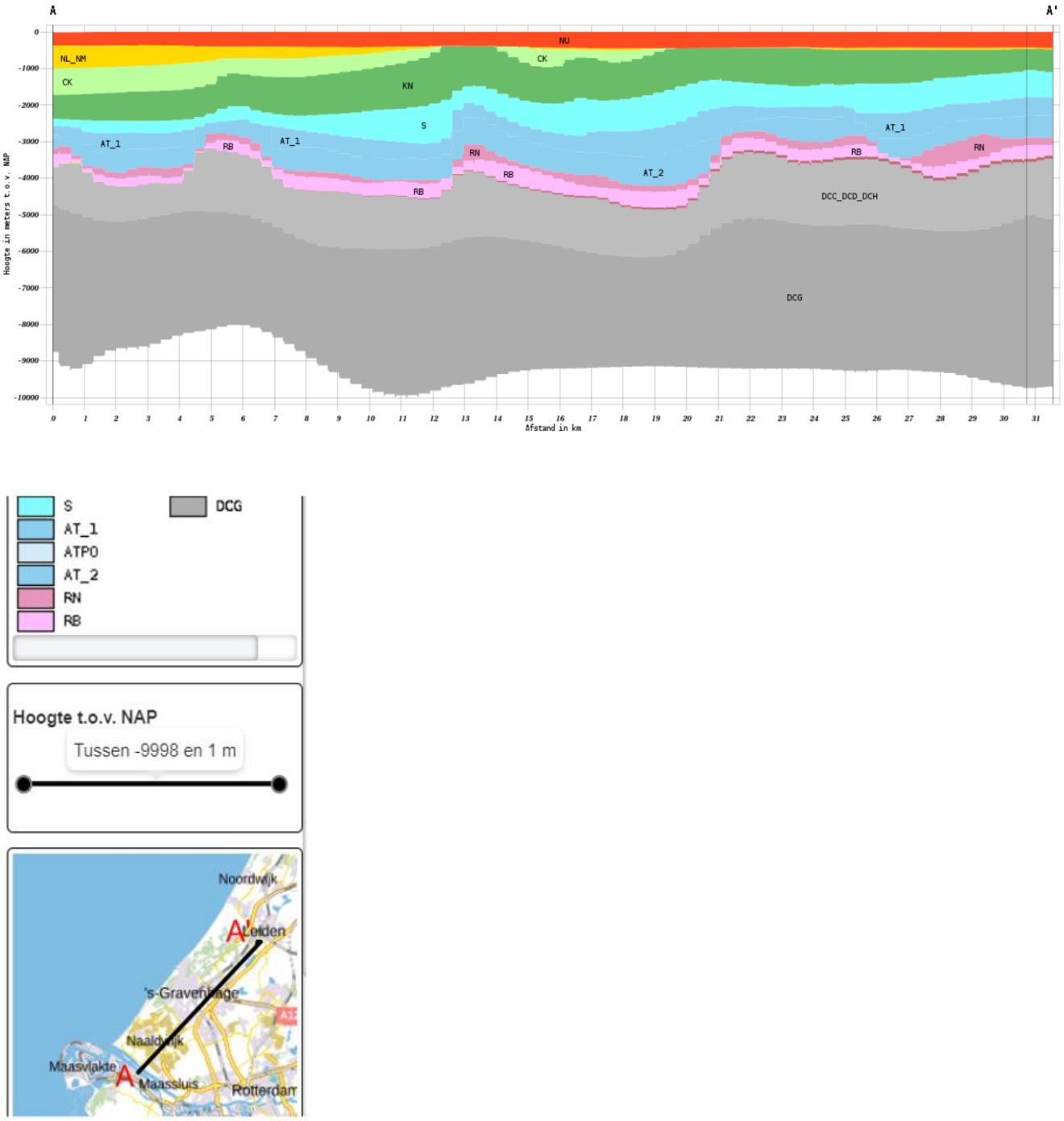

Figure 7: TNO-GDN (2022). Vertical Cross section DGMdeep v5.0 in subsurface models, Accessed on 20-07-2022 from http://www.dinoloket.nl/ondergrondmodellen

2.4 Origin and transport of radioactive Pb-210 in the facilities.

There is an interest in the origin, transport and deposition of Pb-210 from the U-238 decay series, since Pb-210 bearing production water and scale form an important part in the Dutch gas and geothermal industry. Radioactive elements have been a primary source to internal earth heat (Plant & Saunders, 1996). With the driving force of volcanism and plate movements it is transported through fluid transport to the upper layers of the earth crust. It is clear that the radioactive elements can be produced together with hydrocarbons and can be found in the hydrocarbons themselves or in the coproduced water.

Radium, radon and lead are highly mobile elements under reducing oil and gas reservoir conditions: radon being a gas, radium and lead being very soluble in salty waters which dominate hydrocarbon reservoir formation waters. Since these elements are all from the uranium natural decay series, it is plausible that uranium bearing sediments are the source of produced radioactive elements. However, different wells producing from one reservoir can still differ significantly in Bq/kg of produced radioactive elements, which underlines the very local scale of uranium enriched sediments (Schmidt, 2000).

Uranium concentration in reservoir rock
There are two possible options for how reservoir rocks became uranium bearing. The first one is a slow accumulation of uranium in organic rich sediments due to slow sorption from ground waters. Most organic rich sediments are found near reservoirs descending from the Rotliegend and Zechstein formations. A likely source of radioactive elements might be the organic-rich Copper-shale marking the boundary between Rotliegend and Zechstein especially when Rotliegend gas reservoirs are sealed by faults placing the Copper-shale next to the Rotliegend. Another source may be the organic rich Carboniferous Coal measures underlying the Rotliegend when it is placed next to the Rotliegend gas reservoirs. However, in the northern Netherlands area no Carboniferous formations are found next to Rotliegend formations, although it occurs in the northwestern Germany (Schmidt, 2000). Figure 8 and Figure 9 represent a map of the Netherlands were the Zechstein and Rotliegend formations can be found in the subsurface.

As is mentioned in the geological history section a lot of rifting has happened over the years. Times of sedimentation resumed frequently resulting in a formed stable block consisting of fluvial and aeolian sandstones, clay stones, siltstones and carbonates. Followed by the volcanic activities in the north part of the Netherlands and at the South-East border with Germany. During volcano eruption a cocktail of gases, consisting of mostly carbon dioxide and sulfur dioxide, exhales with evaporated heavy metals. These heavy metals can also be radioactive. After the period of volcanic activities inversion caused uplift of layers and mayor faults zones displayed reverse movement. Many hydrocarbon-bearing structures have been formed in this phase. The heavy metals might have been attached to the organic layers and are transported during production for geothermal brine into the facility.

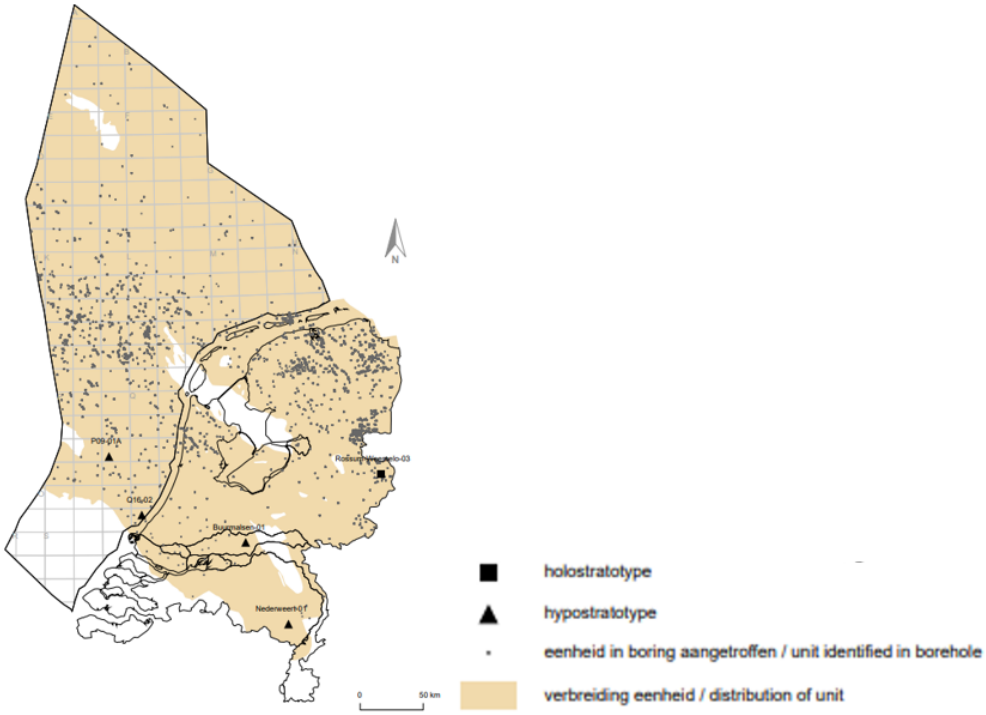

Figure 8: TNO-GDN (2022). Zechstein Group. In: Stratigraphic Nomenclature of the Netherlands, TNO – Geological Survey of the Netherlands. Accessed on 23-07-2022 from http://www.dinoloket.nl/en/stratigraphic-nomenclature/zechstein-group.

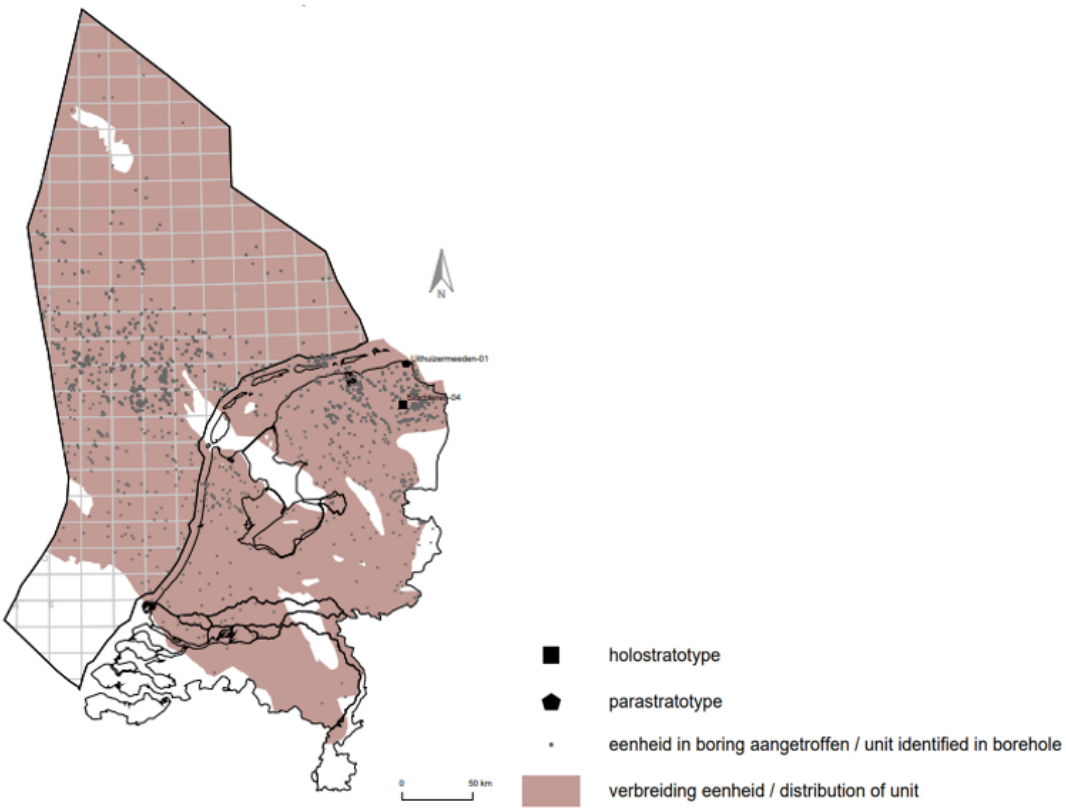

Figure 9: TNO-GDN (2022). Upper Rotliegend Group. In: Stratigraphic Nomenclature of the Netherlands, TNO – Geological Survey of the Netherlands. Accessed on 23-07-2022 from http://www.dinoloket.nl/en/stratigraphic-nomenclature/upper-rotliegend-group.

A positive correlation between organic carbon and uranium contents of the sandstones showed that uranium and bitumen entered the Rotliegend sandstones together. The two other natural decay series, with parent nuclides 235U and 232Th, also contain isotopes of Radium, Radon and Lead. According to geochemical and physical investigations, these isotopes do not contribute significantly to Dutch oil and gas industry. For example, U-235 accounts for only 0.7% while U-238 forms the remaining 99.3% (Eggeling et al., 2013).

Lead originating from the uranium decay in Zechstein Copper-shale

The transport of radioactive elements can occur by producing formation water containing different salts, metals and soluble radioactive elements. Because of the high salinity and acid of the produced water high amounts of radioactive elements can be pumped up into the installations. It can also be transported within saturated water. During the first major gas emplacement in Rotliegend and Zechstein reservoirs in the Northeastern Netherlands, between about 200 Ma and 150 Ma, volatile organic acids accompanying natural gas from Carboniferous source rocks mobilized Pb by dissolving feldspars and Fe-oxides in Rotliegend sediments. These sediments, but especially feldspars in the sediments, contain enough Pb to explain Pb concentrations of 100 ppm or more as currently observed in Rotliegend gas reservoir brines (Schmidt, 2000). Since most Dutch Rotliegend sediments consist of redeposited Late Carboniferous sediments, large amounts of Pb with a Late Carboniferous isotopic signature were added to Rotliegend formation waters. This Pb has been mixed with younger Pb already present and/or flowing in from the overlying Zechstein formation. This Pb probably originated from decay of U in the Zechstein Copper-shale (Schmidt, 2000).

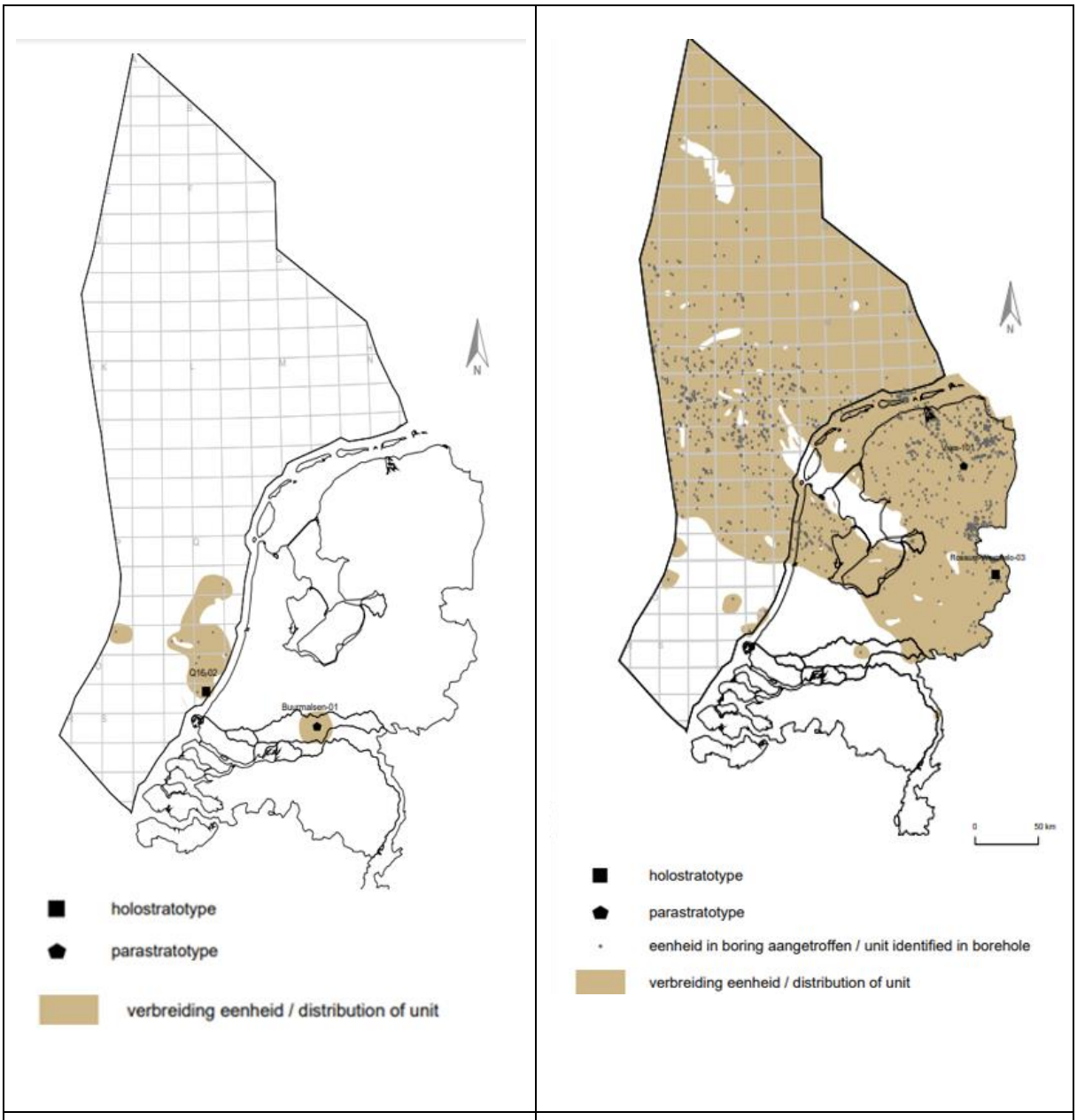

10A 10B

Figure 10: TNO-GDN (2022). Copper-shale Member. (Copper-shale Member | DINOloket, 2022)

As can be seen in Figure 10 a map is illustrated with the places where the Copper-shale Member can be expected. As can be seen in 10A and 10B it is near the coast of our place of interest. Two different maps are made. One of them (10A) has only small local places where Copper-shale can be found. However, it could be migrating through faults along with groundwater flow.

Geological history gave more insight on the layers and forming of the west Netherlands basin and the origin of heavy metals. Iron ores of the Netherlands can be found on the borders of Belgium and Germany, with formations from the Carbon and Pre-Carbon. Volcanic sedimentations can originate from beneath the Wadden sea. And the Lead originating from the uranium decay in Zechstein Copper-shale.

3. Well-logs and scale analysis

3.1 Data introduction

This report is set up because of the radioactive scale, PbS, captured in the injection and production filters of the geothermal installation. In order to find a mitigation strategy, it is important to have all the available data. Water, filter and scale analysis are necessary for understanding the quantity of the scale, chemical brine composition and the scale composition. The well logs will give information of the layers along the well. Logs like gamma ray can be used to identify where radioactive compositions are present in depth. In order to start with the analysis a flowchart is made (Figure 11). First the materials and experimental set-up will be discussed. Followed by analyses and well logs.

Figure 11: Flowchart of water and filter analysis regarding lead scale characterization.

3.1 Materials and experimental set-up for scale analysis

A schematic overview of the geothermal process facility can be seen in Figure 12. Glass reinforced epoxy (GRE) piping systems are used in this installation. In the case study project, hot brine (87°C) is produced from the reservoir (location 1); a Delft Sandstone Member at 2300m depth with a pressure of approximately 230 bar and a flowrate of 450 m^3/h. At the surface the brine pressure is reduced to 10.4 bar. Thereafter, it goes through the degasser to separate the produced gas from the brine. The bulk gas composition consists of methane (70 vol.%), CO_2 (20 vol.%) and N_2 (10 vol.%) leaving the brine at a fluid pressure of 9.2 bar after degassing. The brine then flows through the production- bag filters which hold particles over 5 µm mesh-size. From the production-filters the warm brine goes through the heat-exchanger, made of titanium, where heat from produced water is extracted. Thereafter, the colder brine (35°C) goes through the injection-filters, capturing particles with bag and candle filters. These bag filters have a mesh size of 5 µm and the alternative, candle filters, have a mesh size of 1 µm. The used filters consist of specially selected polypropylene and borosilicate glass fiber material providing an absolute rating of beta 5000 (99.98%removal) and a wide range of micron ratings from which we use the 1 and 5 micron meters (Dutch filtration Maxflow, 2022). Afterwards, the particle free brine is re-injected into the reservoir via the injection well.

PVT analyses are used to determine the phases behavior and properties of brine and gas samples from the well. This sample from location 1 (Figure 12) has been degassed by pumping from the sample cylinder into a trap connected to a gas meter through lowering the pressure and temperature. Then the gas composition has been analyzed as mentioned in the previous paragraph. The remaining fluid consists of a single liquid phase, which has been acidified to a lower pH of circa 2, with the assumption that all solids are dissolved. The outcome of the PVT analysis can be found in Appendix II.

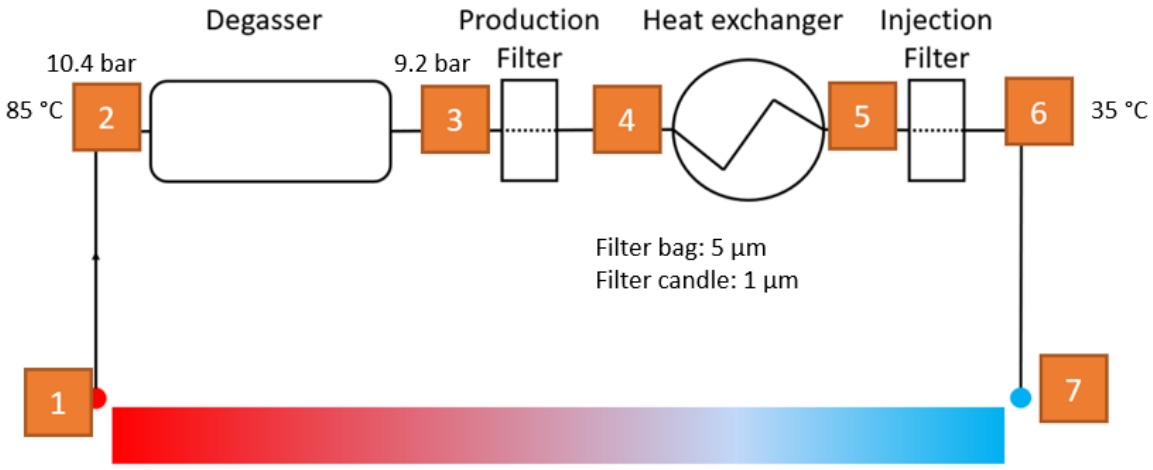

Figure 12: Schematic overview of the geothermal process.

The injection and production filter residue were sampled and sent to a laboratory to analyze for scale mineral composition and possible radioactive additions. The radiation measurements are done by spectral analyses of the total radiation and sorting on frequencies relevant for specific isotopes.

A compositional analysis was performed on a scale sample taken from the injection tubing, between location 6 and 7 in Figure 12. This is done by scraping the scale from the inside of the injection well during a process stop.

In order to get an overview of the available elements in the subsurface and in the geothermal installation, water analyses are conducted besides the one in the PVT analysis.

3.2 Filter scale analysis

3.2.1 Filter scale analysis set-up

Filters.

The first sets of filters are the filter bags located before the heat exchanger. There are 3 filter rows, each row consisting of 8 filter bags. Only 2 rows are in production at the same time.
The second set of filters are located after the heat exchanger. These consist of two filter bag rows and two candle filter rows, where each candle filter row has 5 candle filters. The filter bags and candle filters are located before and after the heat exchanger to prevent clogging in the heat exchanger.

Specifying and quantifying radioactivity.

The results of measured radioactivity analysis of filter residue are given in becquerel per kg of scale solids (Bq/kg). The unit Bq/kg refers to the specific activity, i.e., the activity per unit mass. The activity is given in decays per second (1 decay per second is 1 Becquerel or Bq), while the specific activity is given in Bq per kg (Bq/kg). Each nuclide presents decays with a certain number of disintegrations per unit time. Therefore, the activities (and hence the specific activities) may be different from nuclide to nuclide. If the activities of nuclides within a decay chain (e.g., Pb-210 and Po-210) are equal, this is referred to as radioactive equilibrium. The radioactivity is then given as the total activity of a sample in Bq divided by the mass of the sample.

Capturing radioactive particles.

The total captured scale by these filters is 2 kg per 3 months, which is equal to 8 kg per year of scale. A sample is then taken from this scale and sent to the laboratory. They dry the scale and test the radioactivity of certain elements.

3.2.2 Result filter analysis

The radioactivity of scale samples is shown in Figure 13. As can be seen there are two kinds of filters: filter bags and filter candles. As is mentioned in section 3.1 the difference between these filters are the mesh sizes. However, the filters provide an absolute ration of beta 5000 (99.98% removal). This would mean that the maximum captured scale in the first filter bag would be 99.98% of the total scale with a size larger than 5-micron meters. The second filter bag would theoretically be capturing a maximum of 0.02% of the total scale with a size larger than 5-micron meters. The same would hold for the filter candles, but then only the scale with a size between 1- and 5-micron meters would be captured.

Note that there is no logged data of process time of the filters and the period they are used in. Only the analysis day is logged. In the meantime, fluctuations could occur that have an influence on the flow and scale. Presuming that all filters had the same process time in the system and were used in the same period, one may assume having a scale ratio according to the filter specifics.

There is a difference between the radioactivity of the two production filter bags from January 2021. Looking at the production filters bag of Figure 13B, it can be seen that one filter bag captures around 1 million Bq/kg while the second captures around 10000 Bq/kg. This is about 1%. Since there are

several production filter rows, water can be pumped first into the first row and then be separated towards the second row. It is not known whether they are both one of the first filters or the follow up filters. Also, the samples are taken randomly.

Having a closer look at the Pb-210 results in Figure 13B it can be seen that the injection filter bag and filter candles of the same date of analysis do not represent the ratio given by the specifics of the filters. It can be that if Pb scaling occurs within the installation after the first filters or if the scale size is smaller the 5-micron meters, it will be mostly captured in the filter candles. Also, the analysis of the other radioactive elements are not close to the 99.89%-0.02% ratio of the filters. The conclusion can be that downstream the first filters scale can be formed which would then be captured in the second filter pair.

It can be seen that the measured Bq/kg of lead (Pb-210) is a factor one thousand greater than Uranium, Radium, Thorium, and Potassium. Here, Radium emits less Bq/kg, which indicates that there is a relatively small amount of radium in the analyzed residue. In general, it is a factor of one-million more radioactive than uranium per weight unit. The measured radioactivity of uranium is approximately half of radium, which indicates that there is quantitatively more uranium in the filter residue. Since lead is a decay product of uranium it emits more than 10000 Bq/kg radioactivity. Figure 13 shows that the radioactive emission of thorium is more than four times larger than the that of uranium.

The measured radioactivity of the production and injection filter residue differ from each other up to a factor 5. The radioactive material captured in the candle filters (mesh size 1 µm) are smaller than 5 µm and might therefore flow through the production filter. Next to that smalls scale parts can be formed between the production filters and injection filters.

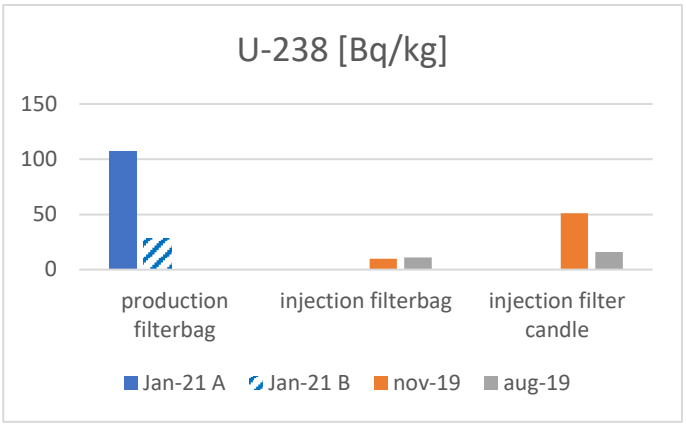

A

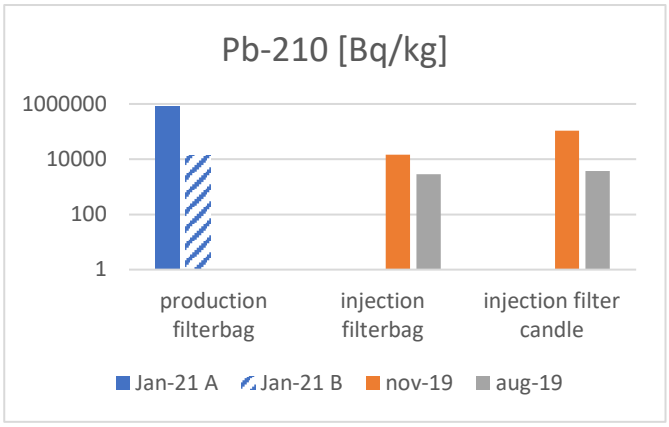

B

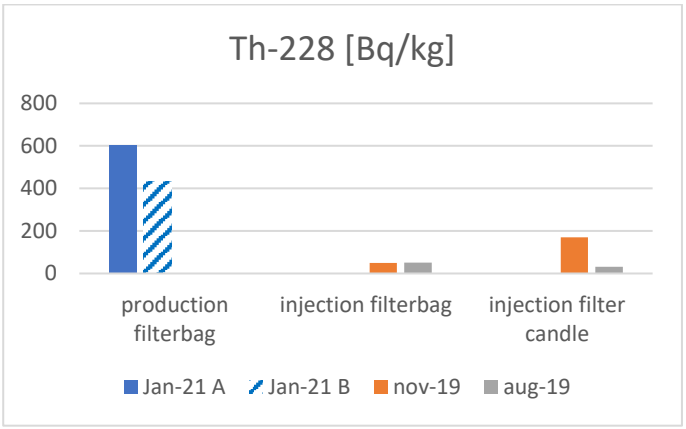

C

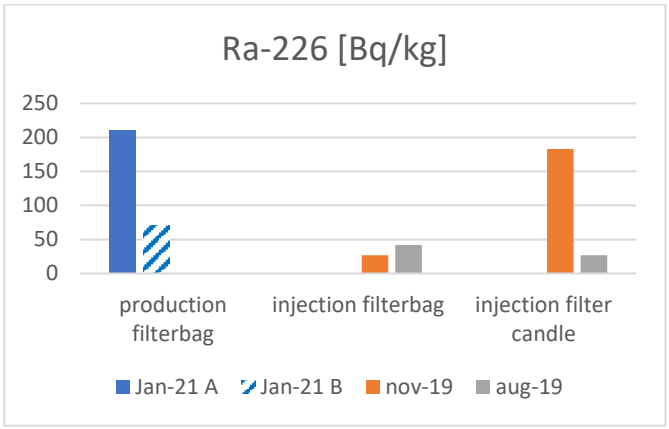

D

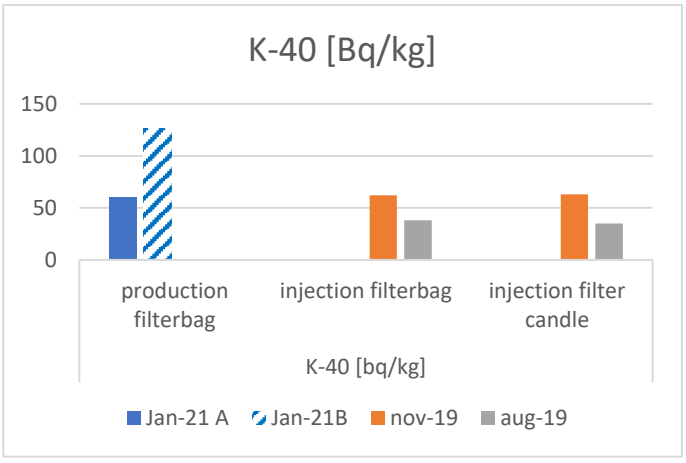

E

Figure 13: Radioactive radiation of Pb, K, Th, Ra and U of the analyzed filter scale in Bq/kg.

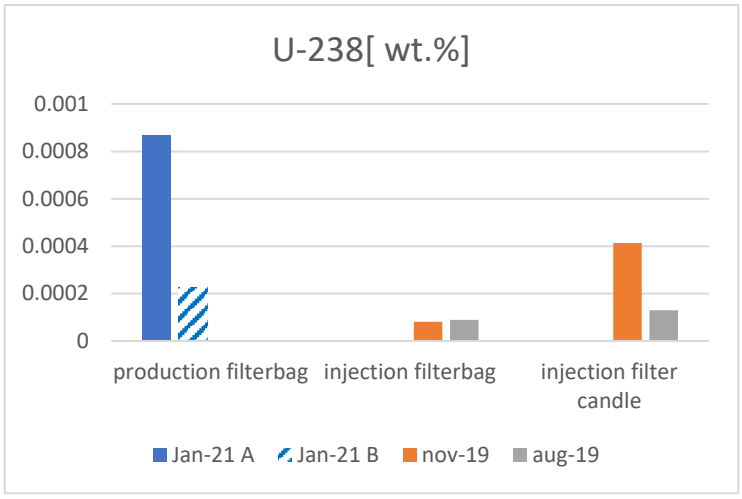

A

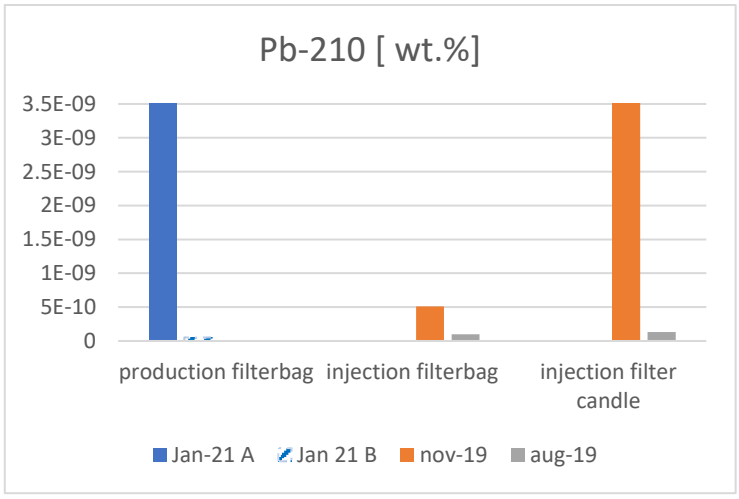

B

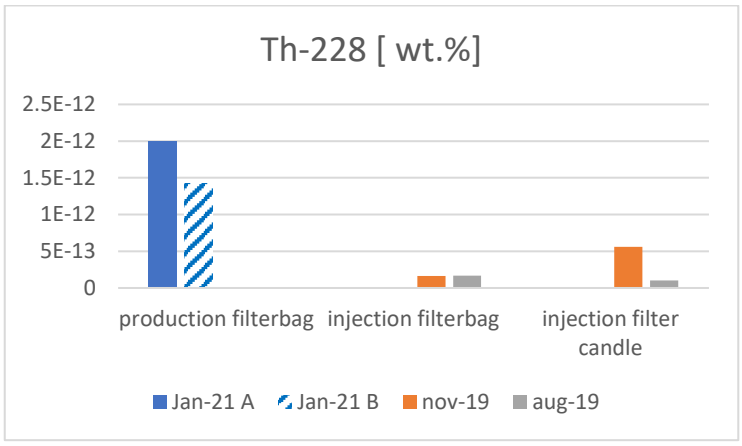

C

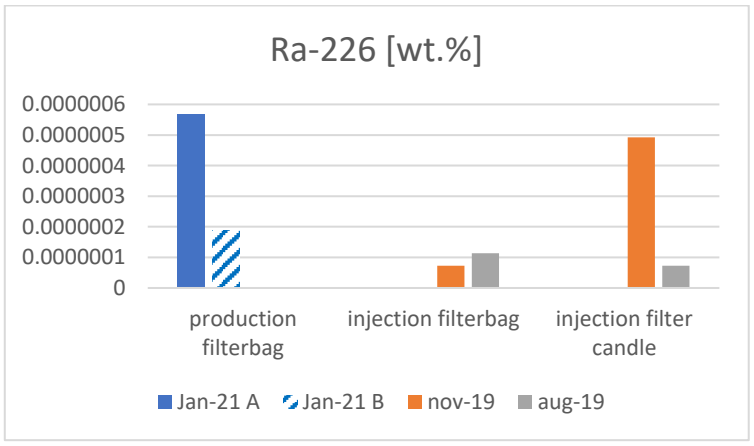

D

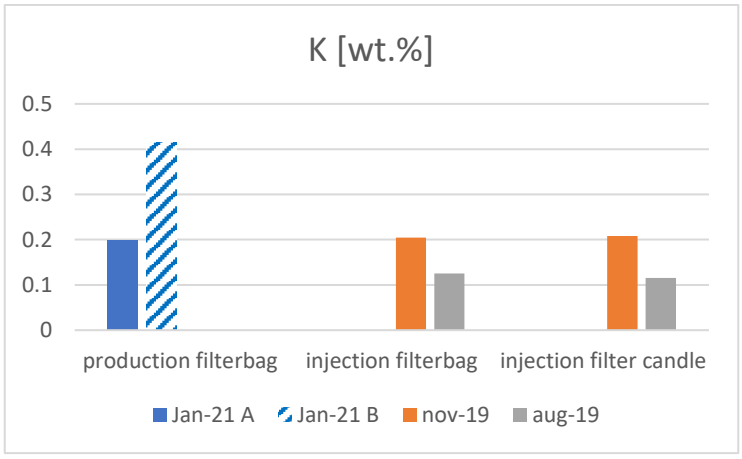

E

Figure 14: Weight percentage of radioactive elements of the analyzed scale in %. (A) U, (B) Pb (C) Th, (D) Ra and (E) K.

In Figure 14 it can be seen that the weight fraction of radioactive potassium present in the scale is a factor 10 000 000 greater than the lead-210. The higher levels of radiation in shale are caused by absorption of thorium by clay minerals, the potassium content of clay minerals, and uranium fixed by associated organic material. Normally, you would see this back in weight percentages according to the following relation:

Gr API = 8* Ur (ppm) + 4* Th (ppm) +16 *K (%)

Referring this back to a spectral gamma ray log, you would see peeks at certain depths where the uranium, thorium, potassium radiation is high. Uranium and thorium can then be referred back to radioactive lead. In addition, other layers could be the suppliers of radioactive material captured in the filters. If so, the re-injected brine needs to pass this layer or the minerals are transported through a fault nearby the reservoir layer where the minerals enter the geothermal brine and are pumped together back into the geothermal surface facility.

The maintenance can also be planned more often to change the filters before reaching radiation limits. This can be done in the subsurface or at the filter locations in the geothermal installations.

3.3 Results compositional analysis of scale from the injection tubing

Between location 6 and location 7 of Figure 12 grey scale was found inside the tubing. A sample of this scale was sent to the laboratory for compositional analysis.

The result of the injection well scale analysis (Table 2), provides the weight percentages of the different minerals in the sample, as presented in the right column.

Table 2: Scale analysis of the injection tubing sample.

Mineral	Chemical formula	Weight percentage (wt.%)
Quartz	SiO_2	25.3
Magnesioferrite	Fe_2MgO_4	8.8
Hematite	Fe_2O_3	1.7
Chalk	$Mg_3(OH)_2(Si_4O_{10})$	3.5
Galena	PbS	15.1
Lead	Pb	6.9
Fluorite	CaF_2	6.8
Halite	NaCl	5.7
Chalcopyrite	$CuFeS_2$	4.4
Lepidocrocite	FeO (OH)	8.3
Zink	Zn	2
Montetrisait	$Cu_6(SO_4)$ $(OH)_{10}$ $2H_2O$	2.9
Goethite	FeO (OH)	6.8
Muscovite	$KAl_3(OH)_2Si_4O_{10}$	1.9

What can be seen from this table is that the total weight percentage of lead-scale is 22 wt.% consisting of lead and galena. This does not necessarily mean that 22 wt.% is radioactive lead, but a part of the weight percentages is from the sulfide of galena and the remaining is lead wt.%. However not all present lead is radioactive. The exact wt.% of radioactive lead is not stated in this analysis. Knowing

that the total captured scale per year is 8 kg, and 15.1 wt.% is galena, equals to 1.21 kg, galena scale per year. Re-calculating this to mol/m^3 gives $1.34 \cdot 10^{-6}$ mol/m^3 of galena scale and $7.07 \cdot 10^{-7}$ mol/m^3 of lead scale.

In addition, some accessory minerals (minerals characteristically formed during the solidification of the rocks and present in small amount) like montetrisait are present in this scale. It is a secondary mineral formed near oxidizing sulfide minerals. Its occurrence is usually associated to kaolinite, galena, sphalerite, chalcopyrite, cerussite, anglesite, goethite, langite, posnjakite, linarite, redgillite in natural hydrothermal systems (Orlandi & Bonaccorsi, 2009). From the scale analysis it can be seen that goethite, chalcopyrite and galena are also present.
Table 2 shows the availability of muscovite in the analyzed scale. However, it is doubtable whether muscovite or its weathering product illite is present. Muscovite is a deep igneous type of mineral while illite is a weathering product created during metamorphism and weathering processes.

3.4 Results Water analysis data

As mentioned in paragraph 3.1, PVT analysis is done and the outcomes are the composition of gas and brine. The brine sample is taken at from location 1 (Figure 12). The results can be seen in appendix ll.

In addition, other water analysis has been done several times, with samples taken between the injection filters and the injection pumps. The samples are sent to the laboratory where all the solids present in the brine were dissolved following NEN EN 15216. The results can be seen in Table 3 and the measurements are given in micron gram per liter sample fluid.

	date	23-7-2019	18-2-2020	25-2-2020	15-6-2020	6-8-2020	14-1-2021	6-5-2021	1-7-2021	28-1-2022	22-6-2022
at 20C	pH	5.80									5.7
at 20C	ρ			1.0917	1.0917	1.0918	1.0917	1.0917	1.0911	1.0909	1.0908
mg/L	Cl	$8.1 \cdot 10^{+4}$		$8.6 \cdot 10^{+4}$	$8.05 \cdot 10^{+4}$	$8.03 \cdot 10^{+4}$	$8.4 \cdot 10^{+4}$	$8.23 \cdot 10^{+4}$	$7.68 \cdot 10^{+4}$	$8.28 \cdot 10^{+4}$	$8.08 \cdot 10^{+4}$
µg/l	NO_{3-}			18	18	<10	130	<10	<10	<10	150
µg/l	SO_4^{2-}	190		220	185	150	160	190	190	190	180
µg/l	Ba	$7.5 \cdot 10^{+3}$		$7.8 \cdot 10^{+3}$	$7.7 \cdot 10^{+3}$	$8.0 \cdot 10^{+3}$	$7.5 \cdot 10^{+3}$	$7.1 \cdot 10^{+3}$		$6.8 \cdot 10^{+3}$	$8.5 \cdot 10^{+3}$
µg/l	Cd	<1	<1				<1		<1		<1
µg/l	Ca	$6.1 \cdot 10^{+6}$		$5.9 \cdot 10^{+6}$	$6.1 \cdot 10^{+8}$	$7.2 \cdot 10^{+5}$	$7.5 \cdot 10^{+6}$	$6.3 \cdot 10^{+6}$	$6.09 \cdot 10^{+6}$	$6.61 \cdot 10^{+6}$	$6.86 \cdot 10^{+6}$
µg/l	Cr	<5	18				<5		63		<5
µg/l	Fe	$6.1 \cdot 10^{+4}$		$6.2 \cdot 10^{+4}$	$4.1 \cdot 10^{+4}$	$3.85 \cdot 10^{+4}$	$5.2 \cdot 10^{+4}$	$5.5 \cdot 10^{+4}$	$4.4 \cdot 10^{+4}$	$6.1 \cdot 10^{+4}$	$5.73 \cdot 10^{+4}$
µg/l	Pb	12	60				30		<1		<5
µg/l	Mg	$8.6 \cdot 10^{+5}$		$8.5 \cdot 10^{+5}$	$9.65 \cdot 10^{+5}$	$8.5 \cdot 10^{+5}$	$1 \cdot 10^{+6}$	$9.3 \cdot 10^{+5}$	$11.3 \cdot 10^{+5}$	$8.55 \cdot 10^{+5}$	$8.8 \cdot 10^{+5}$
µg/l	Mn	1500		1500	1700	1200	1510	1400		2300	1310
µg/l	Ni	<10	11				230		130		<5
µg/l	K	$2.6 \cdot 10^{+5}$		$2.6 \cdot 10^{+5}$	$2.82 \cdot 10^{+5}$	$2.6 \cdot 10^{+5}$	$3.0 \cdot 10^{+5}$		$3.3 \cdot 10^{+5}$	$3.5 \cdot 10^{+5}$	$2.867 \cdot 10^{+5}$
µg/l	Si	$1.5 \cdot 10^{+4}$		$1.5 \cdot 10^{+4}$	$1.3 \cdot 10^{+4}$	$1.28 \cdot 10^{+4}$	250	$1.6 \cdot 10^{+4}$	$1.18 \cdot 10^{+4}$	$1.55 \cdot 10^{+4}$	$4.6 \cdot 10^{+3}$
µg/l	Na	$4.2 \cdot 10^{+7}$		$4.5 \cdot 10^{+7}$	$4.35 \cdot 10^{+7}$	$5.35 \cdot 10^{+7}$	$5.1 \cdot 10^{+7}$	$4.4 \cdot 10^{+7}$	$5.94 \cdot 10^{+7}$	$5.4 \cdot 10^{+7}$	$5.07 \cdot 10^{+7}$
µg/l	Sr	$3.8 \cdot 10^{+5}$		$4.0 \cdot 10^{+5}$	$3.85 \cdot 10^{+5}$	$3.93 \cdot 10^{+5}$	$4.73 \cdot 10^{+5}$	$4.0 \cdot 10^{+5}$	$3.3 \cdot 10^{+5}$	$5.35 \cdot 10^{+5}$	$4.65 \cdot 10^{+5}$
µg/l	Zn	240	130				<20		175		660
µg/l	Hg		0.11								
µg/l	Al								65		

Table 3: Water composition of samples collected downstream from the injection filters and upstream of the injection pumps.

In Table 3 it can be seen that the water composition is in general (+/- 15%) the same over the years with some exceptions. One exception is the amount of present lead which drops from 60 to <1 µg/l. This could be the case when a very small concentration is present and/or the detection limit has been reached, thus a measurement accuracy issue. However, within the time frame from 2019 to 2022, the other elements stay within range.

The water composition analyses in table 3 show all the dissolved elements in the brine. In our case I am interested in the amount of lead available in the brine. Therefore, Figure 15 has been prepared to get a clear overview of the lead content in the water composition over time. As can be seen it increased from the year 2019 to the year 2020; thereafter it seems to slowly decrease towards 2022. However, there is also a possibility that it fluctuates throughout the time significantly. Lack of interval measurements and data errors / resolution issues can influence the results.

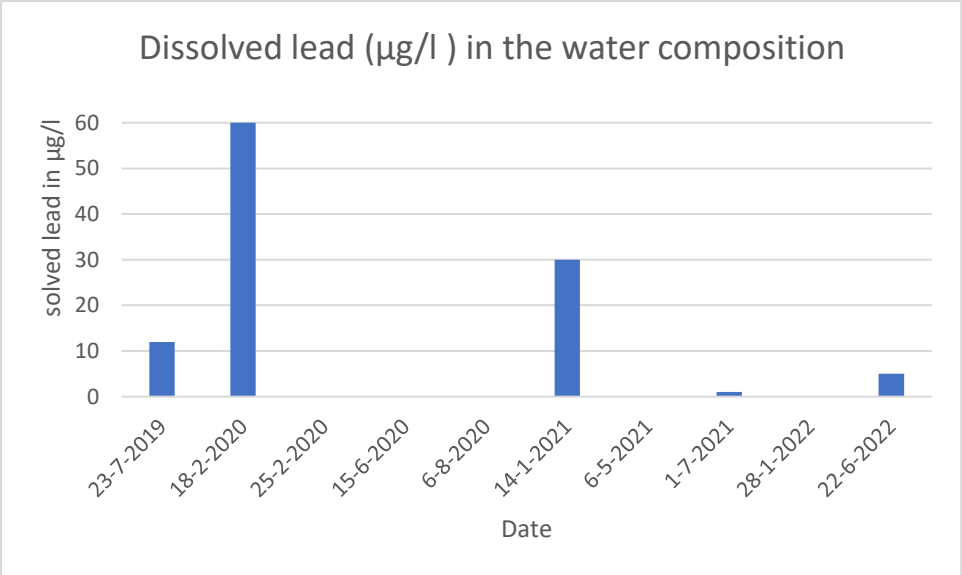

Figure 15: Dissolved lead in the water composition over a period of three years (2019-2022).

Comparing the amount of dissolved lead with radioactivity of Pb-210 (Figure 13), it can be seen that the radioactivity in the injection filter bags and candles increase in 2019. Note that the production filter bags are analyzed at the same moment but still differ from each other. The reason can be that the high radioactive filter is the first filter where the brine flows through. It captures more residue than the filters after it. Or one filter captured more radioactive Lead while the other captures more non-radioactive lead. However, it does not capture every solid lead particle causing radioactive residue in the subsequent filters, but still in a smaller amount. The detection limit and by that measurement inaccuracy may also be a reason.

The measured radioactivity and the amount of lead in the brine are not directly connected to each other. It can be the case that the lead content in the brine is high but also the amount of lead captured in the filters is high. However, a low dissolved lead content in the brine does not mean the presence of a low radioactive lead content in the filter residue. In 2022 the radioactive filter analysis is not done, because of the high measured radioactivity during filter changes. The amount of solved lead in the brine are low in 2022 (see Figure 15), while the captured solid parts in the filters are so high that is could not be analyzed safely.

3.5 Results gamma ray logs and core data analysis

In this report several documents and data on well logs of different wells in the area of interest have been examined to find useful data. An overview of these documents can be found in Appendix IV. For this well, called Well 1, the reservoir formation, Delft Sandstone Member, can be found along a depth range of 2600m-2700m, which is in line with a true vertical depth of 2400-2500m. In order to get a clear overview of the properties in depth, the logs need to be quantified (Figure 16). The depth presented along the y-axis of Figure 16 is the measured depth and not the true vertical depth. The solid blue lines in Figure 16 represent the top and bottom of the Delft Sandstone member. The gamma ray, shale volume fraction, porosity and permeability logs are present, however, only the gamma ray log is directly measured from the well. All others are derived from a V_{sh}/k/phi-relation based on adjacent appraisal wells, i.e., Well 1, Well 2, Well 3 and are based on the Regression of Nieuwerkerk formation. The data of Well 1 is not publicly available on www.NLOG.nl.

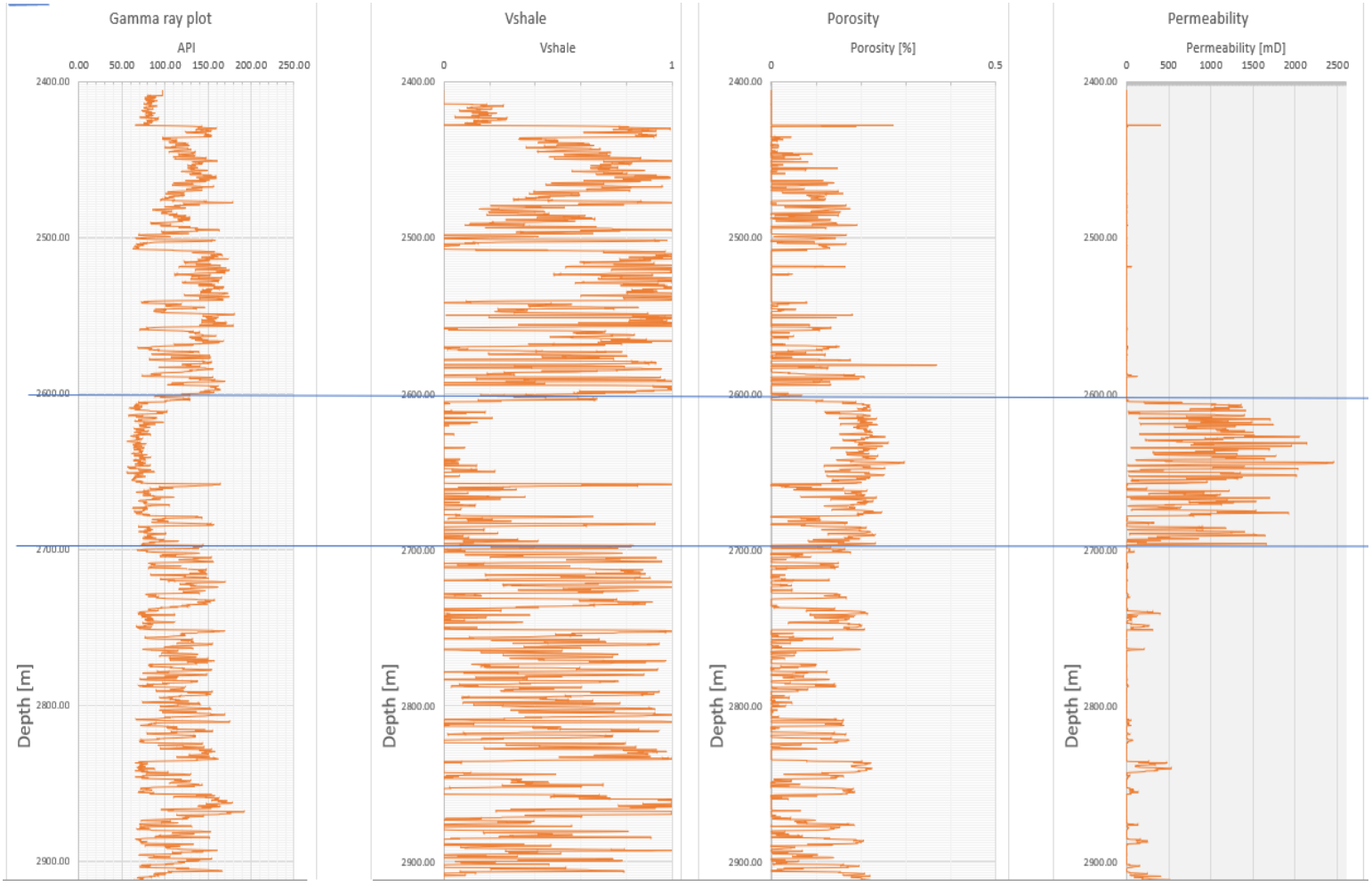

Figure 16: Petrophysical logs off Well 1

Gamma ray

The leftmost log in Figure 16 is the gamma ray log. Gamma ray logging is a wireline logging method used to measure gamma radiation in the subsurface to characterize a rock or sediment. Different sediments and minerals emit different amounts of gamma radiation. Shales emit more gamma rays than other sedimentary rocks like sandstone because of the radioactive potassium which is present in the clay. As can be seen, the gamma ray values of the layers above and below the reservoir are higher than the ones in the reservoir itself. High gamma ray values indicate possible presence of shales or hydrocarbons. These peaks also may indicate radioactive minerals but also a layer of organic material which acts as a sieve for heavy element-ions. The reservoir seems to have average gamma ray around 75 API, except the high peaks at a depth of 2650m, 2675m and 2690m depth. Those can be an indication of radioactive material, highly organic material or a combination of both.

Shale fraction volume, permeability and porosity

The shale volume fraction over the depth of the reservoir, porosity and permeability is provided by PanTerra Geoconsultants B.V. (PanTerra) and is calculated based on the gamma ray and the neutron density logs. As far as I am aware the neutron density logs were not publicly available, nor were they shared for this research.

The shale volume fraction log indicates the high shale concentration at the same depths of the gamma ray peaks. A confined clay layer can be used as a caprock of a good reservoir in the subsurface. The porosity and permeability logs are also presented in the same figure. The porosity log in Figure 16 shows the effective porosity calculated from the neutron density logs and according to PanTerra, verified with the density and sonic logs. The permeability log is calculated from the por-perm relations derived from core plugs presented in Appendix VI.

In addition, a scatter plot is made of the average porosity versus average permeability. This can be seen in Figure 17. This plot is made based on the correlation to other places with the same Delft sandstone layer according to PanTerra. The Swanson Mean regression was used to calculate the expected permeability curve as derived from those core plugs. The linear regression line is made through, however, note that the y-axis of the resulting plot is logarithmic. The presented porosities vary between 12-24%, which proves that the pay zone corresponds to a porous layer.

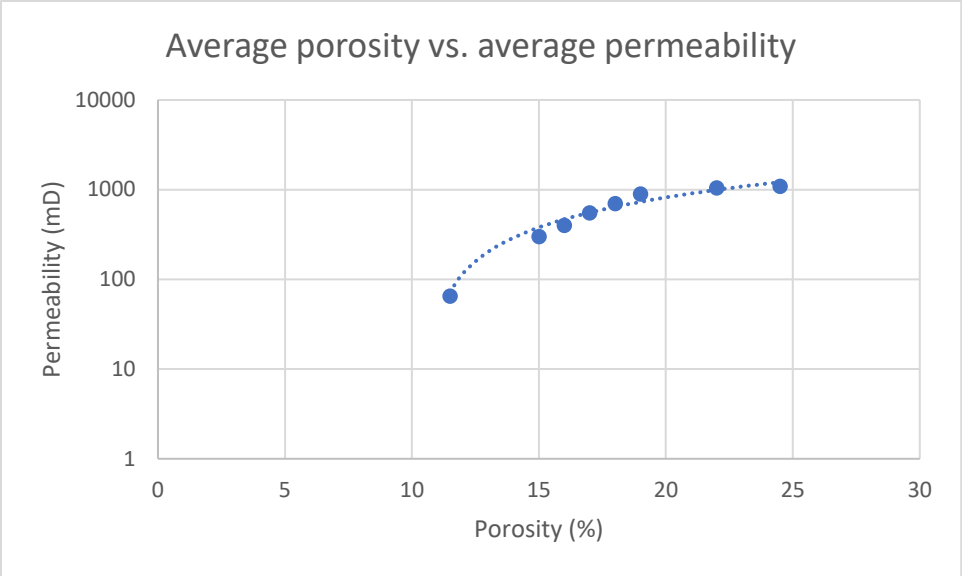

Figure 17: Average porosity vs average permeability of the Delft sandstone layer (PanTerra, 2020). Swanson mean regression line: y = 87.925x - 939.79

Spectral gamma ray

Since radioactive lead, Pb-210, is a decay product of Uranium, it is useful to plot the spectral gamma ray, where Uranium (U), Thorium (Th) and Potassium (K) are separately plotted according to the following relation:

Gr API = 8* U (ppm) + 4* Th (ppm) +16 *K (wt.%).

Note the different multiplication factors used in order to bring the separate element values to a comparable radiation level for summation.

Then, it can be determined where these elements are present in the subsurface. With the half-life time of the elements, it can be reconnected to the radioactive lead which is found in the scale with having the uranium-lead dating in mind. Topmost of the isotopes related to heavy metals have the tendency of sticking to organic clay (Chen et al., 2016).

In the available data there were two types of gamma rays: total gamma ray and a corrected gamma ray without uranium rays. When these were plotted against each other, we found that a multiplication factor was used to create one trendline and thus no spectral gamma ray can be made out of it (Figure 18). The only conclusion can be that over the entire vertical range of gamma-ray measurements, the K+Th contribution is ca. 0.82 the U contribution, assuming that the given “ppm” and “%” factors have been used.

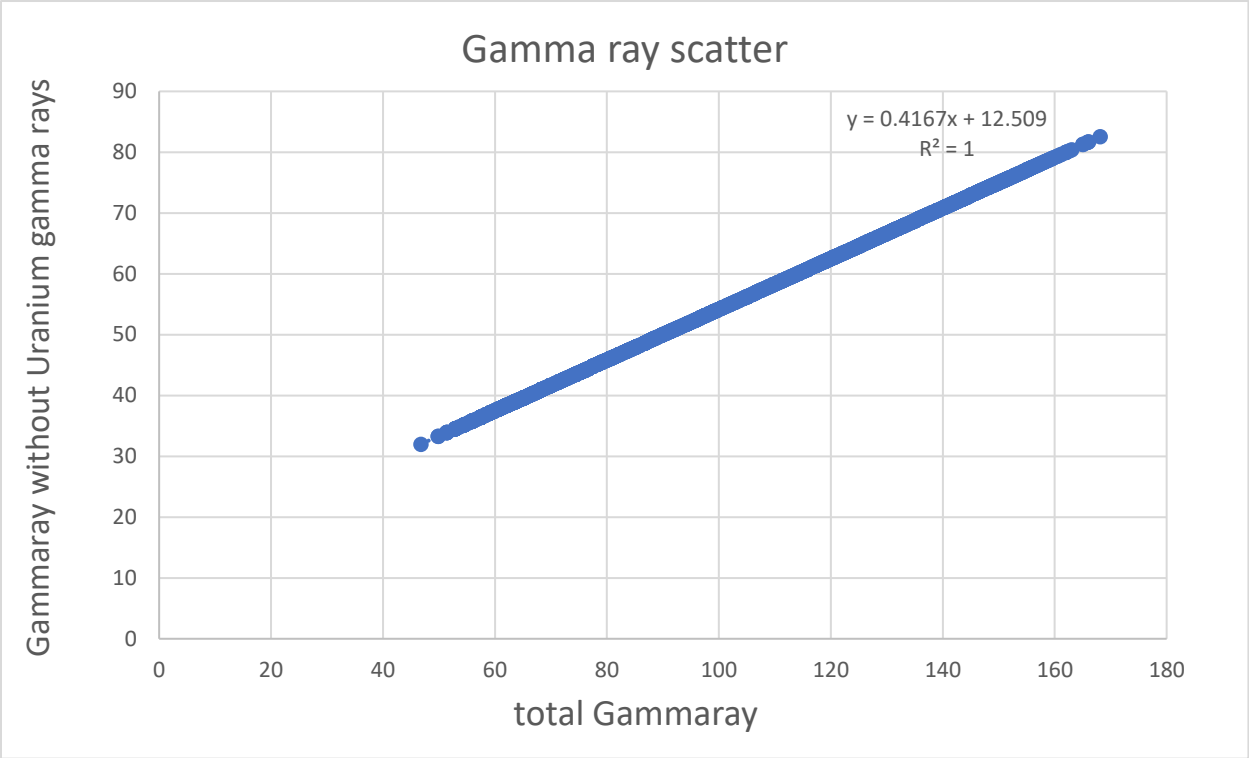

Figure 18: Gamma ray scatter (total vs total-U)

4. PHREEQC

4.1 Introduction

PHREEQC™ is a computer program that can be used for geochemical calculations. Here it is used to do geochemical calculations with the following parameters;

- saturation-Index (SI),
- equilibrium reactions (reaction where precipitations and dissolution happen instantaneously until equilibrium),
- speciation and mixing of solutions calculations (User's Guide to PHREEQC, 2012).

The PVT sample is taken from location [1]. This is done by following the procedures from NEN6966, ISO11885 and NEN-EN-ISO 9377-2. The PVT sample is degassed, and the pH value of the composition has been lowered up to a pH value of 2. In this way only dissolved particles remain in the composition of the water sample. It is assumed that nothing is filtered out of this sample. Afterwards the water has been analyzed and the results are recorded. In order to get a clear overview of the gas composition, the filtered gas has also been analyzed. At location [1] the water analysis and gas analysis are both returned to downhole pressure and temperature.

Modelling is done according to the flowchart represented in Figure 19. Modelling starts with the PVT results and ends at the injection side of the facility.

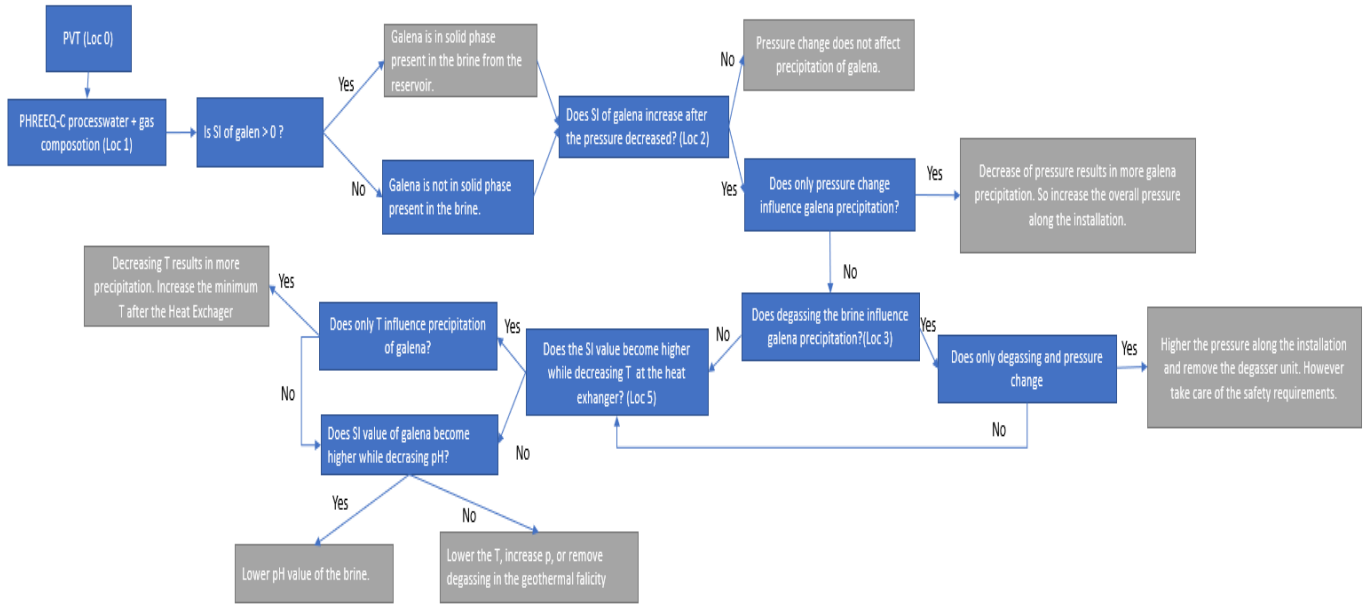

Figure 19: PHREEQC flowchart

Possible mineral precipitation in the geothermal installation is estimated in the following way:

Calculation on galena precipitation is done from the production well [1] towards the injection well [7] of the facility and vice versa (Figure 20):

- I started with the provided PVT-data, gathered downhole at the production perforation of the installation. The sample has been analyzed in a laboratory in such a way that the environmental parameter has been set to simulate the in-situ conditions. The laboratory data needs to be calculated under the right pressure and temperature when "putting' it back in the installation (from [1A] to [1]).
- Afterwards it goes from the production point in the subsurface to the point at the surface before the degasser [2], where it undergoes a pressure drop from 230 to 10.4 bar.
- After going to the degasser, the pressure at [3] becomes 9.2 bar.
- Then it goes through the heat exchanger, where the temperature changes from 85 °C to 35 °C.
- From that point at the surface, it again is pumped into the subsurface at the injection side of the installation [7].

To find out whether or not the same minerals are formed as scale and what can be done to reduce the amount of galena in the installation, different simulation iterations are performed.

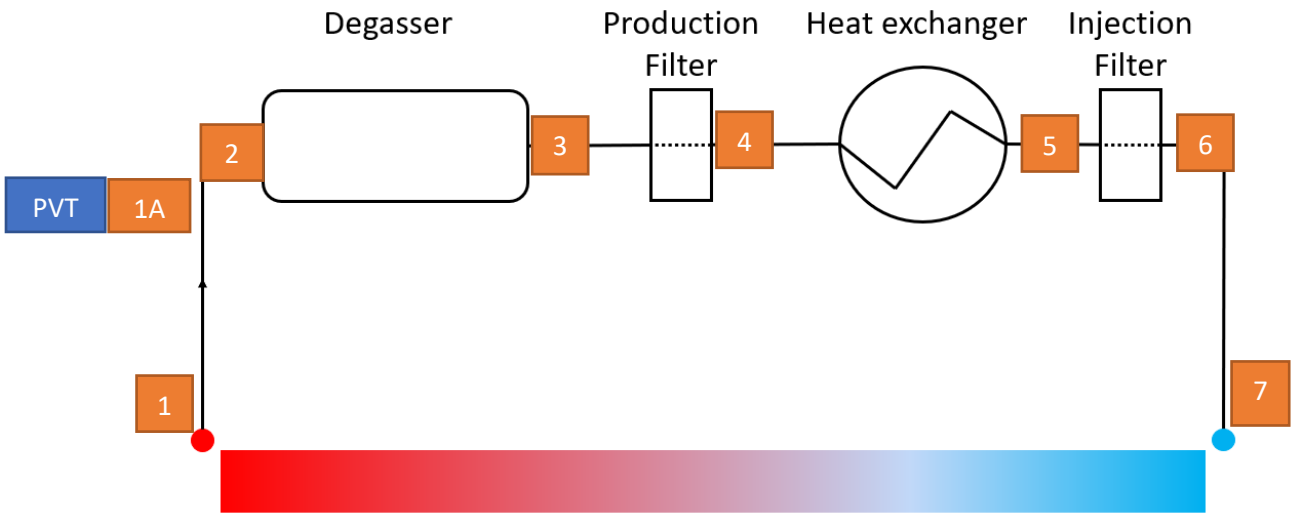

Figure 20: Simulation order in PHREEQC

For different stages in the modelling, different multi-phase compositions for gases and water have been used:

- The brine composition has been simulated through the different locations of the facility. This is done in order to use the right database, which includes all elements present in the brine. The used dataset is llnl.dat available from the PHREEQC package software.
- During the second simulation gas is added. However, gas is considered to be N_2 (g) with CO_2(g). In order to minimize the change of redox reactions, methane gas is considered to be absent in the simulation. However, it is known that methane can be present at amounts up to 1 m^3 per ton of brine.
- In the third simulation, the real gas composition is used in combination with the brine composition. Simulations are done for the locations [1],[2], [3], [5] and [7]. It is done to

compare the effect in each part of the surface facility, of both the brine and potential scale composition.

- During the last simulation series, the same brine and gas compositions, as from the third simulation series have been used. In addition, the solubility of galena is set as a “Saturation Index”, SI=0, at location 1.

Note that it is done with the assumption that the solution subtracted from the reservoir has already reached equilibrium over many years of geological stability. By doing so, it can be detected whether or not the installation facilities have an effect on galena scale formation. If so, what will be the degree of galena formation? At location 3 all the gas is removed as a part of the simulation. The results from the different locations will be recorded and compared to each other; is the geothermal installation causing galena scale formation, or is it transported from the subsurface and passing through the installation. An alternative option could be that it is transported from the subsurface and originate by interaction with parts from the production line in the installation.

Further, it is assumed that in the subsurface, the gases and the aqueous solutions are one phase, which are separated by pressure drop. The desorption provides two separate phases during transport towards the surface. The relevant physical change is caused by a pressure reduction of approximately 220 bar.

During these simulations, several properties, such as the pH value of the solution, pressure and temperature, are changing. In addition, the electronic conductivity (pe) is taken as default during the four simulations.

4.2 Simulations

The first two described simulations in section 4.1 are performed to set the right database and conditions. The third and fourth simulations are performed in order to recognize the influence of pressure, temperature, pH changes and degasification of the brine on precipitation of galena.

- At location 1A, the PVT results are under ambient laboratory conditions
- Then they are changed to comparable in-situ reservoir conditions, considering that water and gas are in one phase (location 1).
- When it is pumped up towards the degasser the pressure decreases, inducing desorption (location 2).
- In the degasser degasification takes place (location 3).
- Afterwards it goes through the heat exchanger where the temperature drops with 50 °C (location 5).
- Finally, the brine is pumped back into the reservoir at location 7 (increasing pressure to 230 bar).

In addition, to see the influence of the injection temperature change it is increased by 10 degrees to 45 °C.

4.3 Results PHREEQC

The results of this simulation can be found in Appendix VII and from these results the SI value of galena is present in Table 4. During the last simulations SI is set to be zero at location 1 as the mineral is considered to be thermodynamically in equilibrium with the fluid. The SI values of galena are stated under the column "SI of galena after equilibrium state".

Table 4: SI value of galena during simulation along the geothermal facility

Location	Pressure (bar)	Temperature (°C)	SI of galena	SI of galena after equilibrium state
[1A] PVT analysis	1	20	-	-
[1] Subsurface production side	230	85	6.33	0
[2] Surface before degasser	10.4	85	6.46	0.13
[3] Surface after degasser	9.2	85	6.43	0.10
[5] After heat exchanger	9.2	35	8.29	1.84
[7] Subsurface injection side	230	35	8.13	1.67

As can be seen, the SI value of galena at location 1 is 6.33. A positive SI value means oversaturation and mineral precipitation has most likely occurred in the subsurface and is transported within the brine into the facility. From the last column of Table 4 it can be seen that the heat exchanger has the most influence on the precipitation of galena (SI=1.84). The decrease in temperature from 85 to 35 °C supports galena precipitation. It can also be seen that pressure decrease (from 230 bar to 10.4 bar) influences precipitation positively, and pressure rise at location 7 supports dissolution of the mineral.

When changing the temperature after the heat exchanger from 35 to 45 °C the influence on SI value decreased by 30% of log SI (from 1.84 to 1.30). This is in line with an actual decrease of influence of 49% based on the calculated log values.

5. The SKID

5.1 What is the SKID

There are still limited possibilities for monitoring the subsurface and facility tubes in the geothermal doublet. All the data and analysis are done based on samples gathered from different places in the geothermal facility and are analyzed under different pressure and temperature. It gives a good impression about the brine quality; however, it is not precise enough for the estimation of minerals present or to be created in the subsurface, tubing and filters.

In chapters 2 to 4 we presented an overview of the variety in geothermal systems at various P, T-values, in different geological settings, with different mineral suits and for different enthalpy changes. To predict the change in fluid/gas composition and associated degrees of corrosion/mineralization, the phase changes should be connected to physio-chemical properties which are directly measured online or parallel to the main tubing of the system. In other words, to monitor the minerals and possible scale formation from the brine, a mobile monitoring station should be available. Several sensors in this monitoring station can be used to make an approximation of the brine composition during instant measured P, V.T-data directly at the injection and production well and in between.

A previous generation of the mobile monitoring station, called the SKID, was not able to measure and monitor the requested information in the progressing brine. Therefore, we propose to design a new SKID with additional measurement and monitoring options, that is able to provide the requested input parameters for the PHREEQC model (Figure 21) Both, Figure 21 and Table 5 show the dimensions of the SKID piping and options for ad-in monitoring/measurement equipment . Requested data acquisition for long term monitoring includes fluid pressure, flowrate, temperature and pH values. The mobile function makes it possible to sample at several surface locations along the line of the geothermal facility. The obtained and stored data can be analyzed and compared to other locations in order to find out whether or not the brine and its composition change, and if so, how it changes.

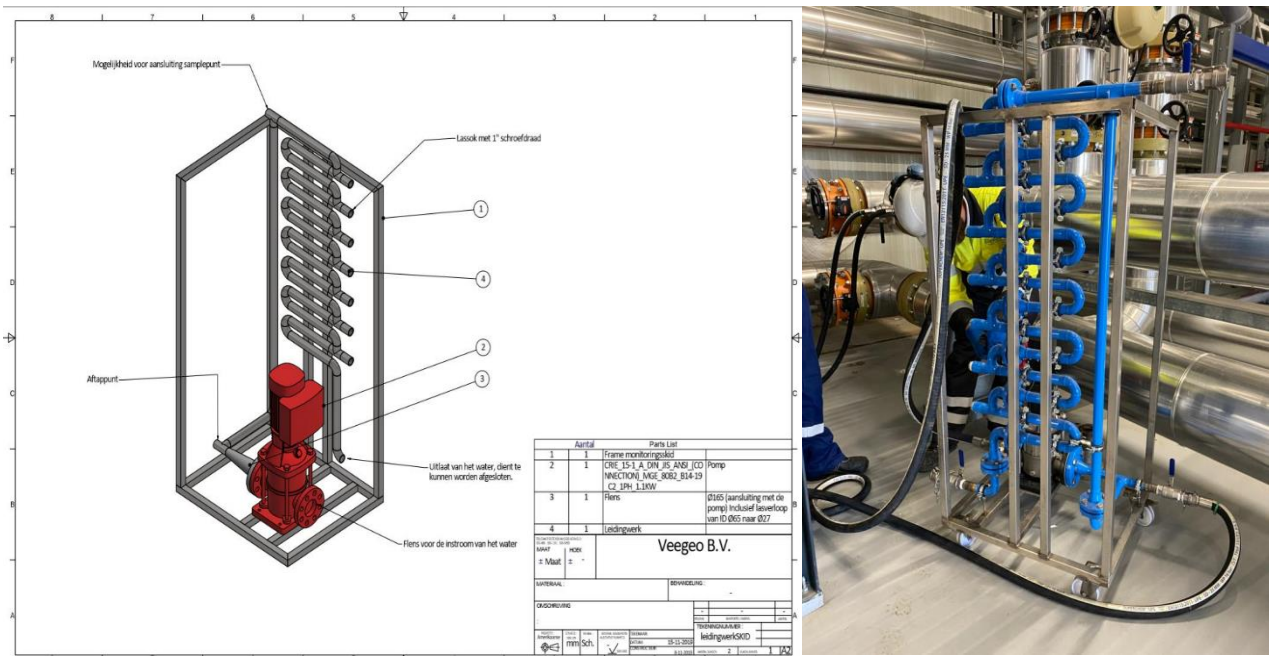

Figure 21: Schematics of the unit (left) and the placement at the surface installation of the geothermal power plant.

As shown in Figure 21, the SKID runs parallel to the main flow lines connected via backpressure valves. For safety reasons and specs of the measurement equipment, the fluid pressures are lower than the wellhead pressure. The pressure and temperature in the measurement part are kept below respectively 10 bars and 90°C. In addition, an expansion vessel helps to instant-degasify the brine within the parallel tubing system. Therefore, new equilibria caused by changing the partial pressures are minimal. In addition, all dissolved ions are in the measured brine and determined for scaling/clogging prediction.

The SKID tubing is coated with CP PHENOLICS ® 210 Red Series. It is a heat cured duroplast coating, resistant to strong alkaline to weak acid media, including all type of cooling waters (containing brackish-, river- and sea-water, salt solutions, greases, oils solvents, gases, food, physiological harmless, in CP phenolics, 2022).

Table 5: SKID piping dimensions

Kind of pipes	Amount	dimensions [mm]	Material
Knee 90 degrees	24	L x W =50 x 50, ID Ø27, OD Ø34	RVS 316
T-part	8	L x W =75 x 55, ID Ø27, OD Ø34	RVS 316
Tube	8	L =255, ID Ø27, OD Ø34	RVS 316
Tube	7	L =259.5, ID Ø27, OD Ø34	RVS 316
Tube	1	L =325, ID Ø27, OD Ø34	RVS 316
Tube	1	L =346, ID Ø27, OD Ø34	RVS 316
Tube	1	L =1300, ID Ø27, OD Ø34	RVS 316
Connection point	7	L =50, OD Ø34, wire 1 inch	RVS 316
welding progress	1	L =/, ID Ø27, from pump to piping	RVS 316
flange for pump connection to piping	1	L =50, OD Ø165, ID Ø65, gaps: Ø18.5 x 21.750	RVS 316

Reynolds number is calculated for several cases and tube sizes. The density of the brine is used and the temperature of at 80 °C, salinity of 120 and the dynamic viscosity of $0{,}485*10^{-3}$ has been taken into account. Calculations with the smallest and largest diameter are performed. The results were all above 6000, which means that the flow in the SKID and in the installation are both turbulent.

5.2 SKID measurement features.

As mentioned in section 5.1 different measurement tools can be used. Some can be used for general water properties, mineral in-situ compositions and for discriminating the solved and unsolved solids in the brine.

The SKID is a tool that can be installed at t-type valves in the facility where the water will flow through the tubes of the SKID and then back into the installation. With this small interruption in the waterflow the brine and the facility circumstances can be analyzed by plugging several sensors into the SKID. Hence for safety, fluid and gas pressure release valves, a possible pump and back-pressure transducer are essential in order to avoid systems breach during a gas kick or sudden rise of fluid flow rate in the main system.

For scaling several parameters need to be measured to get a standard overview of the general water properties. These data are the input for a PHREEQC prediction, followed by a confirmation of lab analysis and progressing SKID measurements.

- *Temperature measuring tool*: The temperature sensor is needed for measuring the brine temperature flowing through the SKID at the certain location. The temperature is important for scale formation as well as corrosion forming. It can also influence properties of liquid and minerals like solubility, conductivity etc. The temperature sensor measuring range is between -50 °C and 150 °C.
- *Pressure gauge:* By measuring the pressure the change of and the effect on potential scale formation can be determined. These in-situ measurements are of interest and are in this way not lowered by temperature or by the escape of gases. PMC11 sensor is chosen that gives a 4-20 mA signal to RSG35 data-logger.
- *pH measuring tool:* Measuring the pH at different locations of the geothermal facility gives a better impression on the total ionic change by mineralization through the system. Current pH values are calculated based on values measured on samples which are already degassed and under a non-in-situ temperature and PHREEQC calculations. These aspects influence the pH value of the brine and can influence the change of scale occurring in the brine. The pH measuring tool will be in combination with the redox equipment This will have CPA442 built-in appliance with a CPS16E sensor connected to a CYK10 cable, which is linked to a CM42 transmitter to convert the signal to 2x 4-20 mA for the RSG35 data-logger.

Next to those measurements also dissolved solids in the brine can influence the analysis. Therefore, the density, electrical conductivity and oxygen/ redox potential need to be measured.

- *Coriolis measurement tool:* this is a density/flux meter. It measures the liquid mass flow, volume flow, gas mass flow and liquid density which gives a better understanding of the formation brine. The flow range is 0 – 300 m^3/day.
- *Electrical conductivity measurement tool:* these tools measurements are used to determine the number of ions or total dissolved solids in the brine. In combination with the density and the ISE (Ion Selective Electrodes) a closer look can be taken at certain ions during the flow through the geothermal facility. The SKID will use CLS21 sensor with a CM82 transmitter to convert measurement data to a 4-20 mA signal to be read by the RSG35 data-logger.
- *Oxygen sensor or Redox potential feature:* This is used to measure whether the liquid is in anaerobic conditions. A value below 0 indicates that there is no oxygen. However, it may contain sulphate or nitrate.

Scale analysis

Up to now, scale only has been captured at the production and injection filters and not on sampling points at other places. From all the residue a random sample is taken to the laboratory for analysis. The results are described in chapter 3, viewed in table 2 and table 3, consist of considerable amounts of scale minerals that may enter the SKID and hamper the flow measurements. To improve the brine quality by removing solid fines via a filter, provides, the measurement accuracy enhances since less or no dirt touch the sensors. Then, the SKID can sample at different locations along the main flow line in the facility. Then samples, for time and flow windows can be compared

to filtered scales analyzed by spectral gamma ray measurements. As a result, the variation of element specific fluorescing results (XRF) of Potassium, Thorium and Uranium can be quantified, and their minerals be qualified (XRD). The results can be related to the in-situ strata holding radioactive lead.

It is preferable to use for this filter bag the same mesh grid sizes as in the filter bags and candles, i.e., 5 µm and 1 µm.

6. Discussion

Geological history

After I did some literature study on the geological history, I found that radioactive lead originates from the Rotliegend and the Zechstein. Through faults, the ions may have travelled to the Delft sandstone layer. The reservoir has two faults on the north-west and south-east side of the reservoir which may have been used as the transportation path into the reservoir. The heavy minerals could also attach to the clay layers above and under the reservoir and mix with the brine by the flow from injection side to production pump.

Upon entering the pores, NORs (Natural Occurring Radioactive materials) may be removed from their source by diffusion and formation water transport. In contrast, under stagnant flow conditions (no current or flow) 226Ra and 210Pb will be preferentially retained within the sediment because of re-adsorption onto sediment grains.

Geothermal facility

In this report it is assumed that the tubing is all GRE. However, a part of the tubing on the production side of the facility consists of steel with an inside coating. It would have the same effect, except when it is damaged. Corrosion may occur at these locations, which can result in galena and elemental lead scaling (Hartog et al., 2002). In addition, the effect of redox reactions is not considered.

Well logs

After searching for well log data I made an illustration of well logs over depth with an indication of the reservoir. In order to use the well logs properly and to determine the depths where radioactive Uranium, Thorium or Potassium are present, a spectral gamma ray is needed. I have searched for a spectral gamma ray of the same layer, at the area of interest and afterwards at other locations. One gamma ray without the uranium rays has been found and used. After I analyzed this data, it is recognized to be calculated data – a fudge factor - rather than measured data. Further, no relevant spectral gamma ray is found in general databases.

Data analysis

As mentioned in section 3.4, the measured amount of lead dissolved in the brine has dropped significantly (60 to <5 µg/l) from the year 2019 to the year 2022. Since samples are taken, the results are very sensitive to human mistakes, measurement errors, flowrate changes or the moment of taking a sample. From the filter scale analysis, it is found that more radioactive scale is captured in the filters. Galena could be transported within the geothermal installation in a solid phase where it is filtered out. However, water analyses are snapshots in time, while scale is captured over a time period. The water samples do not represent a certain (fixed) time frame. The scale analyses are done based on the amount scale captured over time and represent an average captured amount of (radioactive) lead over a given time.

The overview of the amount of filter changes over time could not be discovered. There is no information available about which filter is used where and how long it has been in the production line. In addition, the last captured scale is not analyzed by the laboratory because of the very high radioactivity measured in counts per minute. Because of the high radioactivity of scale captured in the filters, it is less likely that the amount of radioactive lead in the installation dropped. Since it has not been analyzed it is not clear whether the amount of radioactive lead increased or if other radioactive

elements are captured in the filters. On the contrary, water analysis present a decrease of dissolved lead in the brine.

In order to have a clear overview of the amount of radioactive lead captured in the filters over time and how it changes we need to know how long the filters have been used in the geothermal facility before the analysis are carried out. Based on that we can conclude “whether or not it changes over time” and “how it changes over time”. Also, the different measurements can be compared to each other when looking at the lead content over time. This can be facilitated by the use of the SKID. At several locations along the geothermal facilities measurements can be done. The logged data can be analyzed and compared with each other over the same time frame. In this way, brine fluctuations, time dependent physio-chemical results, sample stability and sensitivity are minimized or might be excluded.

Since the filters capture the radioactive scale it is also possible to plan more maintenance stops to change the filters in time before reaching the radioactive limits as is mentioned in section 3.2. However this will only lower the amount of radioactive scale captured per filter, but does not mitigate the problem. A filter system upstream the injection well can also be an option to explore. In this way the solid radioactive elements will be filtered out of the brine before entering the surface geothermal facility.

PHREEQC

When I did the PHREEQC analysis, I performed several simulations in order to test if galena is transported in solid phase from the subsurface and if the geothermal facilities influence galena precipitation. The results indicate that galena is pumped up from the subsurface into the production side of the facility. The SI value of galena was 6.33. The SI value increased by the pressure drop from the subsurface towards the surface by 0.10. It did not change significantly after the degasser but increased with 1.84 after the heat exchanger. This means that galena is formed in the subsurface and transported into the geothermal facility where primarily the heat exchanger favors the forming of galena. Since the residence time of brine flowing through the heat exchanger is short (seconds), the PHREEQC simulations are done based on simultaneous reaction where the reaction speed has not been considered. The results can be influenced by the chosen database (llnl.dat). The software program PHREEQC can be performed based on different databases. It is important to choose the most suitable database for the simulation. In this case I used the database that included all the present elements of the brine.

The heat exchanger can favor scale formation. When changing the minimum temperature of 35 degrees to 45 degrees, the influence of temperature is measured by the change of SI of galena that decreases from 1.84 to 1.29, with a difference of 30% in Log SI and 49% in the actual calculated SI value. In addition, the efficiency of the process also decreases by 10 degrees.

Changing pH value of the brine

In our model, decreasing the pH value of the brine to pH 3, results in galena dissolution. The way of implementing it would be by adding a very acid liquid into the facility. Galena may then dissolve, and less radioactive material will be captured and concentrated in the filters. However, lowering pH by adding chemicals could have an impact on the occurrence of other chemical reactions in the installation and in the reservoir, resulting in acidification and affecting the reservoir conditions. In

addition, chemicals need to be mixed with the brine and the tubing will corrode faster and by that more maintenance time is needed.

Instead of adding chemicals to lower the pH value, the overall facility pressure could be increased and the degasser can be removed. The gas and fluid are then under a higher pressure, but the brine will have a lower pH value because of the partially solved gas by absorption. High pressure installation needs more safety measurements.

7. Conclusion

After investigating the local geological history, literature study, filter-scale analyses, PVT, well logs, water analyses and doing simulations with PHREEQC, I have found some answers to the research questions. My model shows that radioactive lead, in the form of galena, is present in the subsurface in solid and dissolved phase. It is transported into the geothermal installation where galena precipitation is favored under the conditions downstream of the heat exchanger.

Since a large fraction of the collected galena is produced in solid form coming from the subsurface and a small fraction is formed within or by the effect of the heat exchanger, it is good to mitigate the problem from the reservoir by regulating the temperature. There are several methods that can be looked further in to, like:

- pH change: By lowering the pH value of the brine from 5 to 2, galena can be dissolved and would not be captured in the filters. This method is used during the PVT analysis described in section 3.1. It can be done by adding acid to the brine on the production side of the geothermal facility. Research has to be done on the speed of dissolving galena compared to the time available before going through the set of filters.
- More frequently filter changes at the production and injection filter rows. As mentioned in the discussion, the amount of captured radioactive material will be lower and within the obligatory radioactive emission boundaries. It does not mitigate the problem, but it ensures the process proceeds safely.
- Osmose diffusion methods in the subsurface at the bottom hole tubing of the production well. In that way no or less radioactive scale can be pumped up into the installation because it is then already separated in the subsurface at the beginning of the production well. A side tubing can capture the scale or a small pump can pump the scale back into the reservoir. However, more research needs to be done in order to make this solution practical and efficient without causing clogging.
- Underground filters which have frequently maintenance. This means that more stops need to be planned. But it prevents the amount of radiation to reach the regulatory limit, above which more procedures are needed. There are some options as metal mesh screen products that can be applied underground without having to plan stops frequently (*Well Screens | Weatherford International*, 2022).
- Increasing the injected-brine temperature (i.e., to 45 °C) after the heat exchanger will decrease the likelihood of galena precipitation (see paragraph 4.3).

8. References

Adrichem-Boogaert, H. A., & Kouwe, W. (1993). Stratigraphic nomenclature of the Netherlands; revision and update by RGD and NOGEPA. TNO-NITG, Mededelingen Rijks Geologische Dienst. *Haarlem*, *50*.

Altamirano, J. I. C. (2006). *SAMPLING AND ANALYSES OF GEOTHERMAL STEAM AND GEOTHERMOMETER APPLICATIONS IN KRAFLA, THEISTAREYKIR, REYKJANES AND SVARTSENGI, ICELAND*. 17.

Andrews-Speed, P. (2016). Applying institutional theory to the low-carbon energy transition. *Energy Research & Social Science*, *13*, 216–225. https://doi.org/10.1016/j.erss.2015.12.011

Andritsos, N., & Karabelas, A. J. (1991). Sulfide scale formation and control: The case of lead sulfide. *Geothermics*, *20*(5), 343–353. https://doi.org/10.1016/0375-6505(91)90025-Q

Andritsos, N., Karabelas, A., & Koutsoukos, P. (2002, January 1). *SCALE FORMATION IN GEOTHERMAL PLANTS*.

Appelo, C. A. J., & Postma, D. (2005). *Geochemistry, groundwater and pollution* (2nd edition). CRC Press, Taylor & Francis Group.

Bayer, P., Saner, D., Bolay, S., Rybach, L., & Blum, P. (2012). Greenhouse gas emission savings of ground source heat pump systems in Europe: A review. *Renewable and Sustainable Energy Reviews*, *16*(2), 1256–1267. https://doi.org/10.1016/j.rser.2011.09.027

Brown, K. (2013). *Mineral scaling in geothermal power production*. ORKUSTOFNUN.

Chen, Y.-M., Gao, J., Yuan, Y., Ma, J., & Yu, S. (2016). Relationship between heavy metal contents and clay mineral properties in surface sediments: Implications for metal pollution assessment. *Continental Shelf Research*, *124*. https://doi.org/10.1016/j.csr.2016.06.002

Coppershale Member | DINOloket. (2022). https://www.dinoloket.nl/en/stratigraphic-nomenclature/coppershale-member

CP phenolics. (2022). *Cp Phenolics tubing*.

de Jager, J. (2007). *Geology of the Netherlands*. 23.

Dijkstra, H., Dinkelman, D., Hanegraaf, M., Veldkamp, H., van Wees, J.-D., Arkesteijn, R., Braal, R., Clarijs, M., Exalto, H., Huygen, A., Kalkman, A., Meijers, C., & Rösingh, J. W. (2020). *DUURZAAMHEID VAN GEOTHERMIE IN WARMTENETTEN*. 36.

Dutch filtration Maxflow. (2022). *High flow pleated filter cartridge*.

Ed Mroczek, Duncan Graham, Christine Siega, & Lew Bacon. (2017). *Silica scaling in cooled silica saturated geothermal water_ Comparison between Wairakei and Ohaaki geothermal fields, New Zealand | Elsevier Enhanced Reader*. https://doi.org/10.1016/j.geothermics.2017.05.006

Eggeling, L., Genter, A., Kölbel, T., & Münch, W. (2013). Impact of natural radionuclides on geothermal exploitation in the Upper Rhine Graben. *Geothermics*, *47*, 80–88. https://doi.org/10.1016/j.geothermics.2013.03.002

Fridleifsson, I. B. (2001). Geothermal energy for the benefit of the people. *Renewable and Sustainable Energy Reviews*, *5*(3), 299–312. https://doi.org/10.1016/S1364-0321(01)00002-8

García, A. V., Thomsen, K., & Stenby, E. H. (2006). Prediction of mineral scale formation in geothermal and oilfield operations using the Extended UNIQUAC model: Part II. Carbonate-scaling minerals. *Geothermics*, *35*(3), 239–284. https://doi.org/10.1016/j.geothermics.2006.03.001

Hartog, F. A., Jonkers, G., Schmidt, A. P., & Schuiling, R. D. (2002). *Lead Deposits in Dutch Natural Gas Systems*. 7.

Hrefna Kristmannsdttir. (1989). *Types of scaling occuring by geothermal utilization in iceland*. https://doi.org/10.1016/0375-6505(89)90026-6

Huang, Z., Wang, G., Li, N., Fu, Y., Lei, Q., & Mao, X. (2021). Genetic link between Mississippi Valley-Type (MVT) Zn-Pb mineralization and hydrocarbon accumulation in the Nanmushu, northern margin of Sichuan Basin, SW China. *Geochemistry*, 125805. https://doi.org/10.1016/j.chemer.2021.125805

J.H.M. Beerens. (2015). *Binas* (6th ed.). noordhoff uitgevers.

J.J. Wilkinson. (2014). *Mississippi Valley-Type Deposit—An overview | ScienceDirect Topics*. https://www.sciencedirect.com/topics/earth-and-planetary-sciences/mississippi-valley-type-deposit

Langenaeker, V. (2000). The Campine Basin: Stratigraphy, structural geology, coalification and hydrocarbon potential for the Devonian to Jurassic. *Aardkundige Mededelingen*, *9*, 139–142.

Martín-Gamboa, M., Iribarren, D., & Dufour, J. (2015). On the environmental suitability of high- and low-enthalpy geothermal systems. *Geothermics*, *53*, 27–37. https://doi.org/10.1016/j.geothermics.2014.03.012

Mayrhofer, C., Niessner, R., & Baumann, T. (2014). Hydrochemistry and hydrogen sulfide generating processes in the Malm aquifer, Bavarian Molasse Basin, Germany. *Hydrogeology Journal*, *22*(1), 151–162. https://doi.org/10.1007/s10040-013-1064-2

Orlandi, P., & Bonaccorsi, E. (2009). MONTETRISAITE, A NEW HYDROXY-HYDRATED COPPER SULFATE SPECIES FROM MONTE TRISA, VICENZA, ITALY. *The Canadian Mineralogist*, *47*(1), 143–151. https://doi.org/10.3749/canmin.47.1.143

Owen, L. B., & Michels, D. E. (1984). *Geochemical engineering reference manual* (DOE/SF/11520-T1, 6412033; p. DOE/SF/11520-T1, 6412033). https://doi.org/10.2172/6412033

Paul Flowers. (2019, October 15). *Radioactive Decay*. Chemistry LibreTexts. https://chem.libretexts.org/Courses/City_College_of_San_Francisco/Chemistry_101B/10%3A_Nuclear_Chemistry/10.3%3A_Radioactive_Decay

Plant, J. A., & Saunders, A. D. (1996). The Radioactive Earth. *Radiation Protection Dosimetry*, *68*(1–2), 25–36. https://doi.org/10.1093/oxfordjournals.rpd.a031847

P.M.M.C. Bressers & F. Wilschut. (2014). *Lead deposition in geothermal installations*.

Rimstidt, J. D. (2014). *Geochemical Rate Models: An Introduction to Geochemical Kinetics*. 244.

Saidoun, M., Mateen, K., Baraka-Lokmane, S., & Hurtevent, C. (2016, May 11). *Prediction of Sulphide Scales—Improvement of Our Understanding of Heavy Metal Sulphide Solubility*. SPE International Oilfield Scale Conference and Exhibition. https://doi.org/10.2118/179904-MS

Schmidt, A. P. (2000). *Naturally occuring radioactive materials in the gas and oil industry: Origin, transport and deposition of stable lead and 210Pb from Dutch gas reservoirs = Natuurlijk voorkomende radioactieve materialen in de gas- en olie-industrie*. Univ.

Scott, S., Driesner, T., & Weis, P. (2016). The thermal structure and temporal evolution of high-enthalpy geothermal systems. *Geothermics*, *62*, 33–47. https://doi.org/10.1016/j.geothermics.2016.02.004

The System of Environmental Regulations in the Netherlands. (2020). Rijkswaterstaat Environment. https://rwsenvironment.eu/subjects/environmental-0/system-environmental/

Thomas, D. M., & Gudmundsson, J. S. (1989). Advances in the study of solids deposition in geothermal systems. *Geothermics*, *18*(1), 5–15. https://doi.org/10.1016/0375-6505(89)90004-7

van Balen, R. T., van Bergen, F., de Leeuw, C., Pagnier, H., Simmelink, H., van Wees, J. D., & Verweij, J. M. (2000). Modelling the hydrocarbon generation and migration in the West Netherlands Basin, the Netherlands. *Netherlands Journal of Geosciences - Geologie En Mijnbouw*, *79*(1), 29–44. https://doi.org/10.1017/S0016774600021557

V.N. Kashpura, V.V. Patopov. (2001). *Silica Extraction from Geothermal Solution*. https://link.springer.com/article/10.1023/A:1015139628350

Wanner, C., Eichinger, F., Jahrfeld, T., & Diamond, L. W. (2017). Causes of abundant calcite scaling in geothermal wells in the Bavarian Molasse Basin, Southern Germany. *Geothermics*, *70*, 324–338. https://doi.org/10.1016/j.geothermics.2017.05.001

Well Screens | Weatherford International. (2022). https://www.weatherford.com/products-and-services/well-construction-and-completions/sand-face-solutions/sand-control/well-screens/

Willems, C. J. L., Vondrak, A., Mijnlieff, H. F., Donselaar, M. E., & Kempen, B. M. M. van. (2020). Geology of the Upper Jurassic to Lower Cretaceous geothermal aquifers in the West Netherlands Basin – an overview. *Netherlands Journal of Geosciences*, *99*. https://doi.org/10.1017/njg.2020.1

9. Appendix

Appendix I: Subsurface cross sections

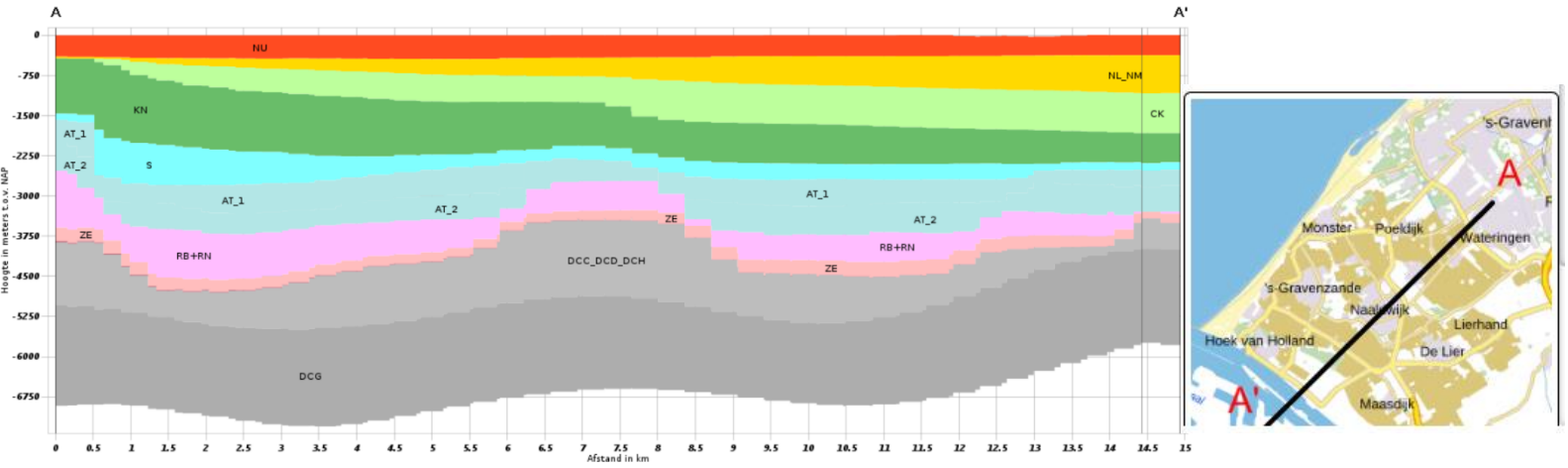

Figure 22: North-South cross section through the area of interest. Vertical Cross section DGMdeep v5.0 in subsurface models, Accessed on 20-07-2022 from http://www.dinoloket.nl/ondergrondmodellen

Cross sections from the subsurface through the area of interest are made from Nort-south, Figure 22 , and East-West, Figure 23. Different subsurface layers can be seen in these cross sections. Also, the lateral progress of layers is illustrated.

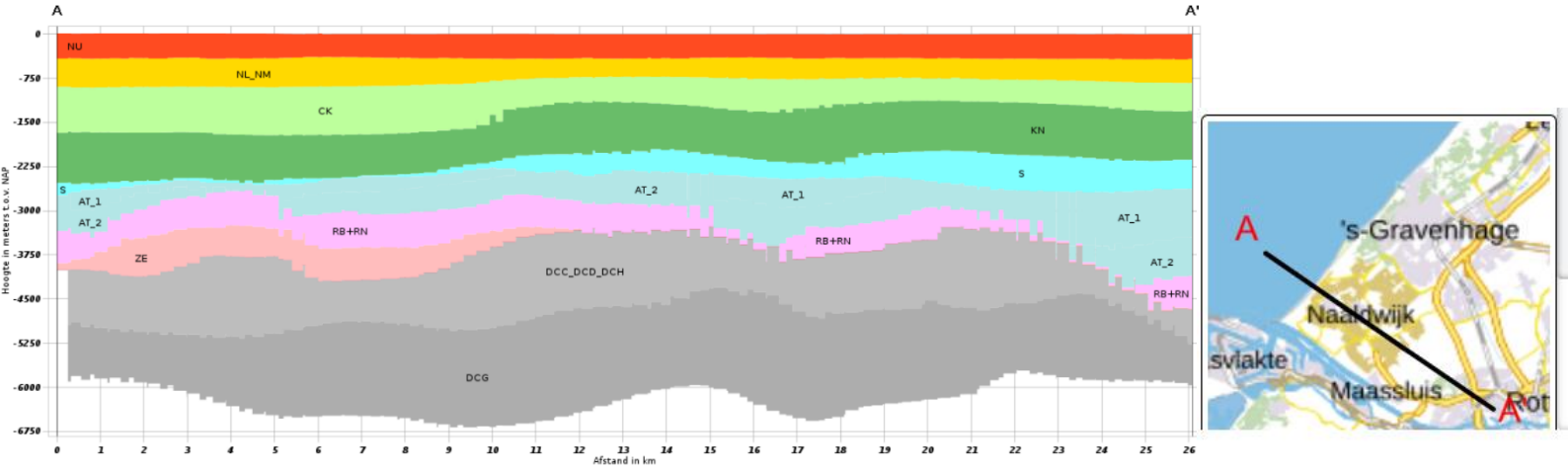

Figure 23: East-West through the area of interest Vertical Cross section DGMdeep v5.0 in subsurface models, Accessed on 20-07-2022 from http://www.dinoloket.nl/ondergrondmodellen

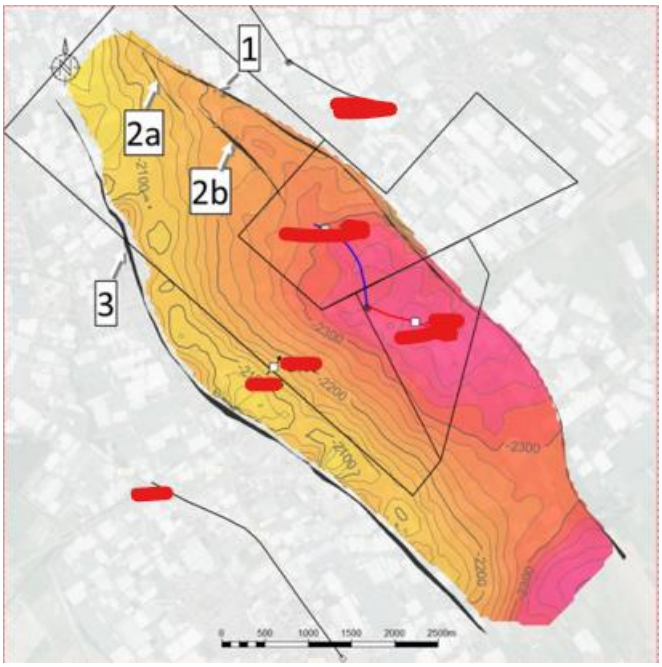

This figure shows a top view of the place of interest where faults are illustrated with the dark grey lines and its numbering 1, 2a, 2b and 3. It can be seen that the production wells are within two major faults. These faults may serve as a transport way for radioactive elements from the deeper subsurface towards the reservoir.

Appendix II PVT

PVT Gas analysis from July 17, 2018.

Flashed Gas Composition

A volume of single-phase water was pumped from the sample cylinder into a trap connected to a gas meter at atmospheric conditions of pressure and temperature. The flashed water and gas volumes, separation temperatures and atmospheric pressures are accurately recorded. The composition of gas is subsequently measured using the procedure described below. The flash GWR (gas water ratio) is calculated as the ratio between the flashed water and the collected gas.

The resulting gas fraction purged from the cylinder was analyzed using the gas chromatography procedure. Compositions up to C11+were measured. Components: porous polymer and mole sieve columns, TCD detector (for C1- C3, permanent gases), capillary column and FID detector (for C4 to C11+).

Resistivity

First the water sample is filtered and degassed. The resistivity must be measured by using a fluid resistivity cell connected to an impedance analyzer. The fluid resistance is converted into resistivity by multiplication by the cell constant.

Density

The density of the water was measured using a digital u-tube handheld densitometer, model Anton Paar DMA 35. A sample causes a change in the oscillation frequency of a vibrating glass U tube. The change is directly proportional to the density of the sample. The embedded software allows for temperature correction when the ambient temperature is different than standard.

pH

The pH meter used is an Orion 370 pH meter. Before any measurement, a 3-point calibration measurement is run for the standard buffers that will correspond with the selected calibration pH mode (pH 4/7/10). After calibration, the pH electrodes are rinsed with deionized (D.I.) H2O and blot dry. For the actual measurement, the bottom part of the electrode is immersed in the sample, and when the "ready" light comes up a stable pH value is obtained and frozen and the display can be read. For each new sample, the step above is repeated and the electrode is rinsed every time in deionized water.

Water Compositional Analysis

ICP is used to identify and quantify the positive ions present in water samples.

- The content of chloride, carbonate and bicarbonate is measured by titration.
- The sulfate content is measured by turbidity method or a spectrophotometer.
- The hardness of the water samples is calculated by based on the content of Calcium and Magnesium. Values will be reported as CaCO3 content in ppm, grains per gallon and Degrees German (G.D.H.)

Component		Mole%	Weight%
H_2	Hydrogen	0.000	0.000
H_2S	Hydrogen Sulphide	0.000	0.000
CO_2	Carbon Dioxide	8.574	19.055
N_2	Nitrogen	6.395	9.046
C1	Methane	83.322	67.501
C2	Ethane	1.014	1.539
C3	Propane	0.105	0.233
C4	i-Butane	0.022	0.064
C4	n-Butane	0.019	0.054
C5	i-Pentane	0.074	0.268
C5	n-Pentane	0.021	0.078
C6	Hexanes	0.119	0.506
	MC Pentane	0.003	0.012
	Benzene	0.036	0.140
	Cyclohexane	0.004	0.019
C7	Heptanes	0.015	0.073
	MC Hexane	0.007	0.034
	Toluene	0.201	0.936
C8	Octanes	0.015	0.080
	E-Benzene	0.001	0.007
	M/P Xylene	0.003	0.016
	O-Xylene	0.001	0.003
C9	Nonanes	0.013	0.082
	1,2,4 TMB	0.002	0.015
C10	Decanes	0.030	0.205
C11+	Undecanes +	0.004	0.033
	Total	100.000	100.000

Calculated Gas Properties	
Gas Density (kg m^{-3} @ 15°C)	0.886
Gas Mole Weight (g mol^{-1})	19.803
Real Relative (to air) Density of Gas	0.685
Mole weight of Heptanes Plus (g mol^{-1})	97.561
Density of Heptanes plus (g cm^{-3} at 60°F)	0.834
Mole Weight of Undecanes plus (g mol^{-1})	147.000
Density of Undecanes plus (g cm^{-3} at 60°F)	0.789
Calorific Value (MJ m^{-3})	35.082

Air Content: 12.77 %

Parameter	Unit	Result
Metals [According to ISO 17294-2] (A)		
Nickel	µg/l	620
Uranium	µg/l	<1.0
Metals [According to NEN 6966 (EN-ISO 11885)] (A)		
Aluminium	µg/l	130
Arsenic	µg/l	<10
Barium	µg/l	7200
Boron	µg/l	29000
Cadmium	µg/l	29
Calcium	µg/l	5900000
Copper	µg/l	230
Iron	µg/l	130000
Lead	µg/l	92
Lithium	µg/l	9100
Magnesium	µg/l	830000
Manganese	µg/l	2500
Potassium	µg/l	350000
Selene	µg/l	<20
Silicium	µg/l	14000
Sodium	µg/l	39000000
Strontium	µg/l	370000
Zinc	µg/l	2200
Acidity/Alkalinity [According to WAC/III/A/006 (based on ISO 9963-1)]		
Alkalinity up to pH 4.5	mmol/l	2.0
Alkalinity up to pH 8.3	mmol/l	<0.050
Bicarbonate same as HCO3	mg/l	130
Carbonate same as CO3	mg/l	<2.5
Anionen [According to ISO 10304-1]		
Bromide	mg/l	300
Chloride	mg/l	88000
Nitrate as N	mg/l	<10 *
Sulphate	mg/l	200
Fluoride	mg/l	<10 *
Discrete analyser [According to ISO 15923-1]		
Phosphate	mg/l	<0.050
Volatile compounds BTEX [According to ISO 11423-2]		
Benzene	mg/l	0.083
Toluene	mg/l	<0.040
Ethylbenzene	mg/l	<0.040
M/P-Xylene	mg/l	<0.080
O-Xylene	mg/l	<0.040
Sum BTEX	mg/l	<0.29
Mineral Oil Fractions [According to OSPAR 2005-15]		
Gedispergeerde olie	mg/l	14
Hardness (Calculated)	mg CaCO3/L	18024
pH [According to ISO 10523]		
pH	-	6.0
Temperature pH-measurement	C	22.5

Appendix III Results scale analyses

		01	02
Galenit	PbS	XX	-
Quarz	SiO_2	X	X
Calcit	$CaCO_3$	X	X
Phosgenit	$Pb_2Cl_2CO_3$	X	-
Wulfenit	$PbMnO_4$	X	-
Kaolinit	$Al_4(OH)_8Si_4O_{10}$	X	X
Nontronit	$Na_{0,41}Fe_2Si_4O_{10,01}$	X	-
Biotit	$KMg_3Al(OH,F)Si_3O_{10}$	X	-
Halit	NaCl	-	XX
Sylvin	KCl	-	X
Dolomit	$CaMg(CO_3)_2$	-	X
Aragonit	$CaCO_3$	-	X
Phengit	$K(AlMg)_2(OH)_2(SiAl)_4O_{10}$	-	X
Melilith	$AlCaNaSi_2O_7$	-	X

		01
Quarz	SiO_2	25,3
Magnesioferrit	Fe_2MgO_4	8,8
Hämatit	Fe_2O_3	1,7
Talk	$Mg_3(OH)_2(Si_4O_{10})$	3,5
Galenit	PbS	15,1
Blei	Pb	6,9
Fluorit	CaF_2	6,8
Halit	NaCl	5,7
Chalkopyrit	$CuFeS_2$	4,4
Lepidokrokit	FeO(OH)	8,3
Zink	Zn	2,0
Montetrisait	$Cu_6(SO_4)(OH)_{10}{\cdot}2\ H_2O$	2,9
Goethit	FeO(OH)	6,8
Muskovit	$KAl_3(OH)_2Si_4O_{10}$	1,9

Filter change data

Next to that some additional data on the change of filter bags and filter candles in the geothermal installation are found. CPM (counts per minute) measurements are done on the residue found in the filters. These measurements has been done twice. The first time the residue is still wet and could have some radon gas in it. During the second measurements the residue has been set for some time and is dryer than before. However, the second measurement turned out to be higher than the first measurements, which is odd since the radon gas is gone and no extra elements are added. A reason could be that another measurement tool is used which is calibrated at a different level. Or there is a change in the way of measuring CPM's during the first and second measurements. No conclusions could be made from this data because of incomplete registrations. This data can be found in the external data which is an excel file named: 'Filterwissels'.

Appendix IV Searched files for petrophysical logs.

			depth
MAP	File	Description	
EOWR	EOWR_NLW-GT-01	performation, DSST depth	
	EOWR_NLW-GT-02	performation, DSST depth	
Core analysis	core analysis	2 files, core data at 4000m depth	
Evaluatie_OK	G1340_petrophysics_NLW-GT-01_Delft.pd	gr, neu-den & sonic log made by panterra in pdf	
	G1340_petrophysics_NLW-GT-01_KNSL.pd	same as above with additional porosity, perm, lithology	
	LSL-GT-01_Kh .las	GT-01 data perm, phi & vshale panterra	0-2700
	NLW-GT-01_Lithologie .las	gammaray from Trias_NLW-GT-01_Run1B_NeutronDensityLog_MainPass_11-Jan-2017.dlis, vshale porosity, permeability	0-4500
Fieldprint	usit	Graphical data of cementation	
	Trias	D. Opened zipfiles. But data is to deep	4000+m
	Survey	No log data	
	Onderkrijt	Gamma ray gt-01 :Trias_NLW-GT-01_Run1A_SonicCo	2389-2536
		Gamma ray gt-01 : Trias_NLW-GT-01_Run1A_SonicCc	2394-3204
		porosity, density, gammaray. Trias_NLW-GT-01_Run1B_NeutronDensityLog_MainPass_11-Jan-2017	2405-3180
		Trias_NLW-GT-01_Run1B_NeutronDensityLog_RepeatPass_11-Jan-2017	2420-2534
Filteranalyse		No log data	
Gas analyse		No log data	
Missing MDW	NLW-GT-01_TeleScope-GR_8.5in_RT_LAS_N	Too deep GT-01	4085-4446
	NLW-GT-01_TeleScope-GR_17.5in_RM_LAS	Too shallow GT-01	1197-2351
	Trias_Westland_24in_GR_LAS_RM_19Nov	Too shallow GT-01	131-1293
	NLW-GT-02-S1_12.25in_MWD-Gamma_Ra	GT-02S gamma ray	2335-2679
	NLW-GT-02-S1_17.5in_MWD-Gamma_Ray	Too shallow GT-02	1081-2384
olie analyse	no log data		
scale analys	no log data		
water analyse	no lg data		
wireline log NLW-GT-01		NLW-GT-01_8_5in_Triple Combo logs output.las Too	4000+m
	OK run 1 A en 1B see fieldprint		
	Trias	Too deep	
ireline log NLW-GT-02-S	missing mDW see section above		
	EOW already handles		
	Test data	about sensors	
	Zipfiles	extracted, and also belong to missing mdw	

Putten	Beschrijving
GAAG-06	ondiep
GAAG-06 sid	diep genoeg, maar geen delft zandsteen pakket
GAAG-05	gag05t03.a2 dichtheid, maar lastig af te lezen
GAAG-03	diep genoeg, maar geen delft zandsteen pakket
GAAG-01	gag01t01.s2 Lisfile density moet nog geopend worden.
GAAG-02	diep genoeg, maar geen delft zandsteen pakket
DE LIER-42	ondiep
DE LIER-41	ondiep
DE LIER-39	ondiep
DE LIER-48	ondiep
DE LIER-49	ondiep
DE LIER-32	ondiep
DE LIER-31	ondiep
DE LIER-33	ondiep
DE-LIER-14	ondiep
DE-LIER-15	ondiep
DE-LIER-13	ondiep
DE-LIER-04	ondiep
DE-LIER-11	ondiep
DE-LIER-7	ondiep
DE-LIER-8	ondiep
DE-LIER-29	ondiep
DE-LIER-2	ondiep
DE-LIER-10	ondiep
MNZ-01	gamma ray in pr_gr_ccl_19jan14-lf4-frm1.las
DE-LIER-05	ondiep
DE-LIER-40	ondiep
DE-LIER-25	ondiep
DE-LIER-23+	ondiep
SGZ-01	diep genoeg, maar geen delft zandsteen pakket
Q16-08	diep genoeg. Density in 8379_q1608_1988_com.las . Alleen met gaten. Controleren of de laar er daadwerkelijk tussen zit

Velden		
Rijswijk	Niet diep genoeg	
De lier	3739_mor density	monster-03
Gaag	1322_gag density	
schravenz	geen delft sst	
berkel	ondiep	
Moerkape	geen delft sst	
zoetermee	geen delft sst data	
Wassenaa	ondiep	
Wassenaa	ondiep	
rotterdam	geen delft sst	
Pernis	Geen delft sst	
pernis we	geen data	
botlek	dichtheid	
Papenkop	geen delft sst	
Q16-FA	geen delft sst	
P18-2	wel aanwezig, maar 5 meter	
Wassenaa	geen data	
Q14	geen delft sst	
Brakel-01	density & neutron log	

Dropbox	
EOWR GT-01	perforaties TVD en depth
EOWR GT-02	perforaties TVD and depth
Trias_NLW-GT-01_Run1B_NeutronDensityLog_RepeatPass_11-Jan-2017	ondiep
Trias_NLW-GT-01_Run1A_SonicCompressional_MainPass_11-Jan-2017	alleen gamma ray
Trias_NLW-GT-01_Run1A_SonicCompressional_RepeatPass_11-Jan-2017 (1	alleen gamma ray
NLW-GT-01_TeleScope-GR_8.5in_RT_LAS_MD_Field_4105-4447m	Te diep 4000+ meter
NLW-GT-01_8_5in_Triple Combo logs output (1)	Te diep
Trias_Westland_24in_GR_LAS_RM_19Nov17	Ondiep -1200 m
NLW-GT-02-S1_17.5in Section (1)	Zipfile, geen bruikbare info

Appendix V Well logs

The spectral uranium gamma ray data of Well 1 is calculated by a factor and not generated/ measured. Therefore, the ratio of K, TH and U is not reliable. In addition, for further analyses only the total gamma ray can be used.

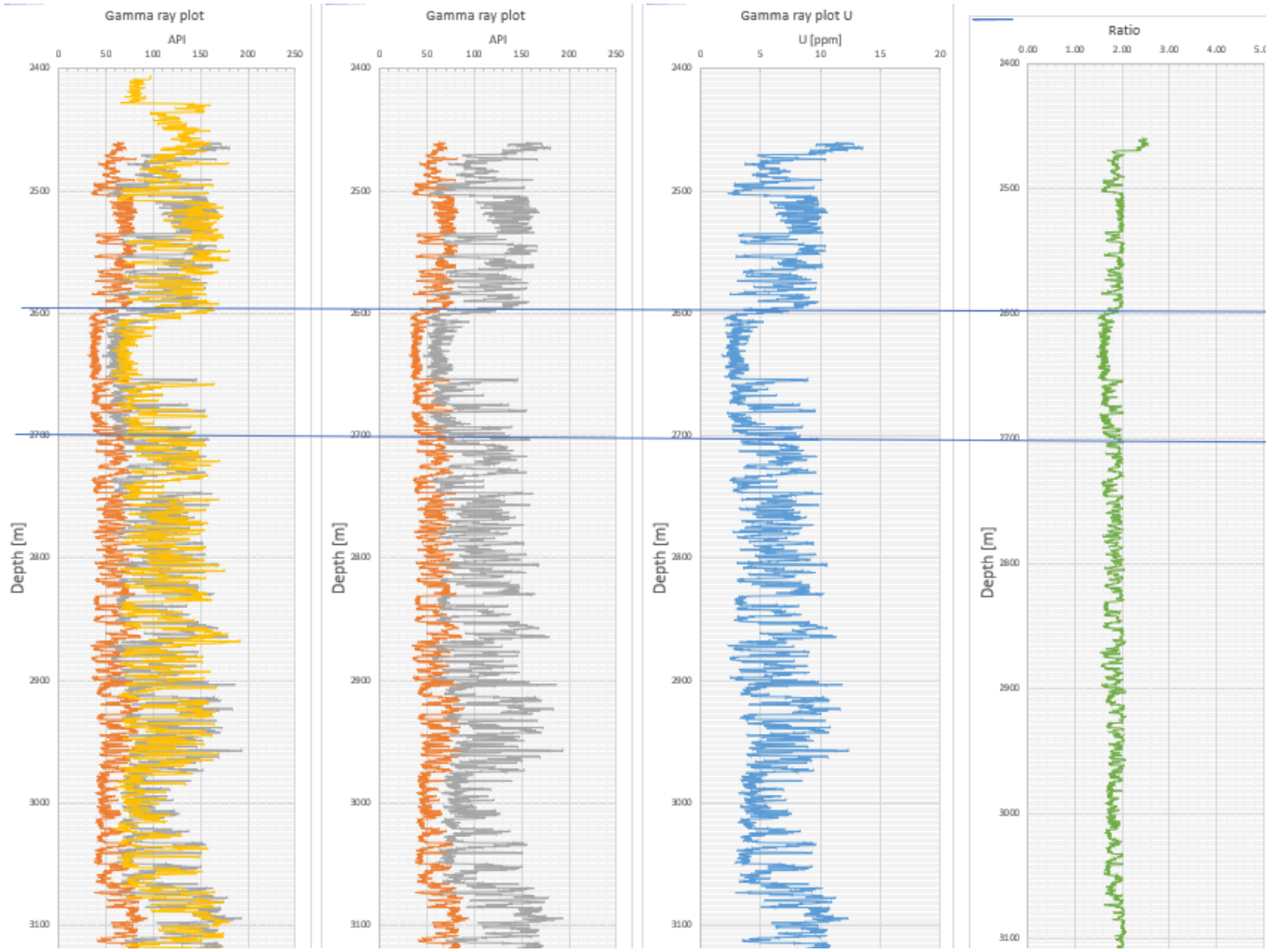

Poro-perm relations from core plugs

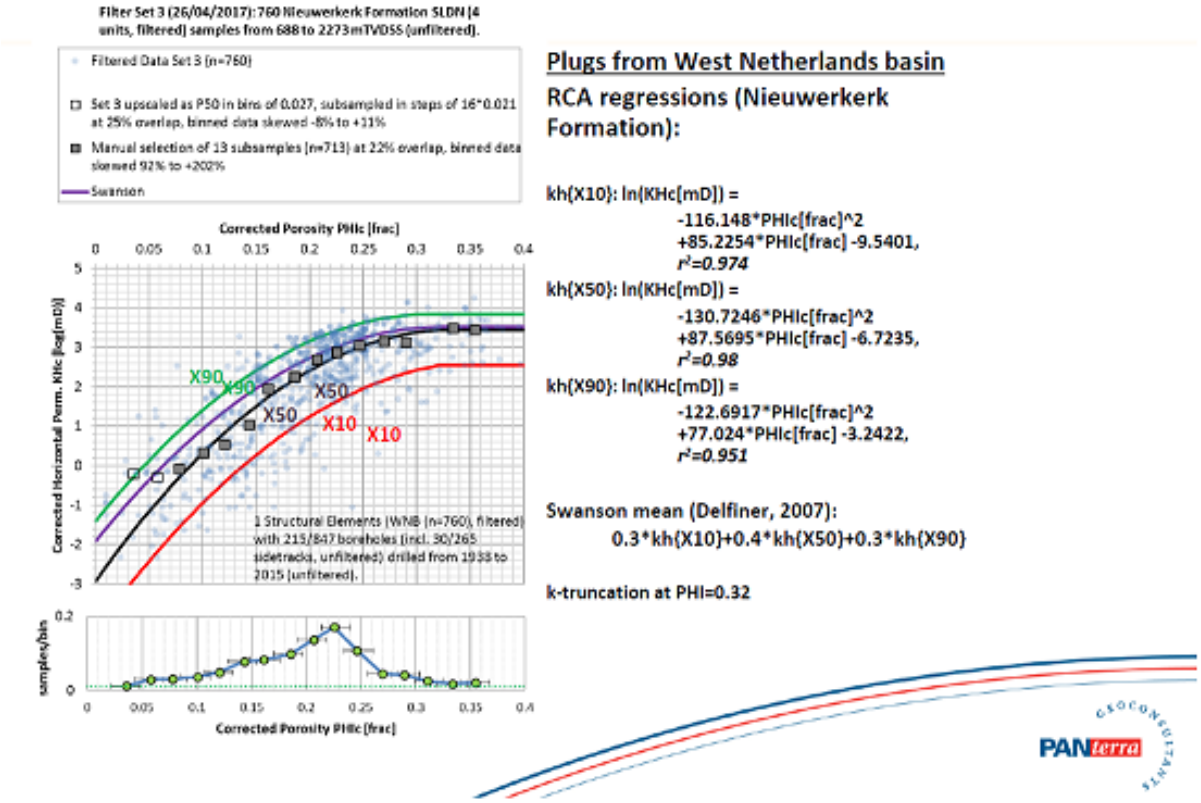

Plugs from West Netherlands basin

RCA regressions (Nieuwerkerk Formation):

kh(X10): ln(KHc[mD]) =
-116.148*PHIc[frac]^2
+85.2254*PHIc[frac] -9.5401,
r²=0.974

kh(X50): ln(KHc[mD]) =
-130.7246*PHIc[frac]^2
+87.5695*PHIc[frac] -6.7235,
r²=0.98

kh(X90): ln(KHc[mD]) =
-122.6917*PHIc[frac]^2
+77.024*PHIc[frac] -3.2422,
r²=0.951

Swanson mean (Delfiner, 2007):
0.3*kh(X10)+0.4*kh(X50)+0.3*kh(X90)

k-truncation at PHI=0.32

Appendix VII PHREEQC

Input file

```
#DATABASE C:\Program Files (x86)\USGS\Phreeqc Interactive 3.6.2-
15100\database\llnl.dat
#TITLE Example 2.--Temperature dependence of solubility

#Punt 11 alleen lab water
SOLUTION 1 Process water
        pressure  1
        pH      6
        density 1.0917
        temp    22.5
        units   mg/l

        Cl              80300
        N               10
        S(6)            200
        Ba              7.2
        Ca              5900
        Fe              130
```

```
        Mg              830
        Mn              2.5
        K               350
        Si              14
        Na              39000
        Sr              370
        Pb              0.092
        Ni              0.62
        Zn              2.2
        C               130
        U               0.001
        Al              0.13
        B               29

PITZER
      -macinnes         true
      -use_etheta       true
      -redox            true

SAVE SOLUTION 1
END

PHASES
Galena
      PbS + 1.0000 H+ = 1.0000 HS- + 1.0000 Pb+2
      -analytic   1.909920e+003     6.546249e-001     -7.577074e+004    -
7.575379e+002     2.733540e+006     -2.484938e-004
      -Vm    31.4900
      #-steps 1 day 24 steps


Fix_H+
H+ = H+
log_K 0

GAS_PHASE 1 Gas phase
      temperature 0 C
      pressure    1 bar
      volume      1.3909406 L
      N2(g)       0.06395
      CO2(g)      0.08574
      CH4(g)      0.85030


SAVE GAS_PHASE 1
END

#Punt 12 Gas+Water in de ondergrond waarbij si van galena op 0 staat.

USE SOLUTION 1


REACTION_TEMPERATURE 1
      85
REACTION_PRESSURE 1
      230
USE GAS_PHASE 1

#EQUILIBRIUM_PHASES
#     Galena      0.0
```

```
SAVE SOLUTION 2
END

#Punt 13 voor de degasser

USE SOLUTION 2

REACTION_PRESSURE 2
      10.4
SAVE SOLUTION 3
EQUILIBRIUM_PHASES
      Galena      0.0
END

# PUNT 14 na de degasser

USE SOLUTION 3

REACTION_PRESSURE 3
      9.2
EQUILIBRIUM_PHASES
      CH4(g)      0.0
#EQUILIBRIUM_PHASES
#     Galena      0.0

SAVE SOLUTION 4
END

# PUNT 15 na de Heat exchanger

USE SOLUTION 4

REACTION_TEMPERATURE 4
      35
EQUILIBRIUM_PHASES
      Calcite     0.0 10 precipitate_only


#EQUILIBRIUM_PHASES
#     Greenalite        0.0

SAVE SOLUTION 5
END

USE SOLUTION 5

EQUILIBRIUM_PHASES
       Aragonite  0.0 10 precipitate_only

#EQUILIBRIUM_PHASES
#     Greenalite        0.0

SAVE SOLUTION 6
END

# PUNT 16 injection point
#EQUILIBRIUM_PHASES
#     Galena      0.0
USE SOLUTION 6
```

```
REACTION_PRESSURE 6
      230
SAVE SOLUTION 7
END

#EQUILIBRIUM_PHASES 1
#     Fix_H+      -8 NaOH 10.0
```

Result PHREEQC after simulation at location 5

Phase	SI**	log IAP	log K(308 K, 9 atm)	
(UO2)2Cl3	-66.65	-54.78	11.86	(UO2)2Cl3
Afwillite	-32.84	25.31	58.15	Ca3Si2O4(OH)6
Akermanite	-18.83	24.75	43.58	Ca2MgSi2O7
Al	-82.31	62.15	144.46	Al
Al(g)	-131.14	62.15	193.29	Al
Al2(SO4)3	-67.26	-50.47	16.79	Al2(SO4)3
Al2(SO4)3:6H2O	-50.94	-50.62	0.32	Al2(SO4)3:6H2O
Alabandite	-2.07	-2.63	-0.56	MnS
Alamosite	-5.32	0.24	5.56	PbSiO3
Albite	0.95	3.30	2.35	NaAlSi3O8
Albite_high	-0.31	3.30	3.61	NaAlSi3O8
Albite_low	0.95	3.30	2.35	NaAlSi3O8
Alstonite	-2.68	-0.10	2.58	BaCa(CO3)2
Alum-K	-27.31	-32.24	-4.93	KAl(SO4)2:12H2O
Alunite	-14.87	-16.69	-1.82	KAl3(OH)6(SO4)2
Amesite-14A	-6.45	64.26	70.70	Mg4Al4Si2O10(OH)8
Analcime	0.57	6.19	5.62	Na.96Al.96Si2.04O6:H2O
Analcime-dehy	-5.54	6.21	11.75	Na.96Al.96Si2.04O6
Andalusite	-2.83	11.70	14.53	Al2SiO5
Andradite	-12.10	19.35	31.45	Ca3Fe2(SiO4)3
Anglesite	-10.21	-18.07	-7.85	PbSO4
Anhydrite	-6.59	-11.05	-4.47	CaSO4
Annite	0.30	28.13	27.83	KFe3AlSi3O10(OH)2
Anorthite	-5.78	18.95	24.74	CaAl2(SiO4)2
Antarcticite	-6.84	-2.76	4.08	CaCl2:6H2O
Anthophyllite	-21.06	42.64	63.70	Mg7Si8O22(OH)2
Antigorite	-88.89	367.42	456.31	Mg48Si34O85(OH)62
Aphthitalite	-20.68	-24.57	-3.89	NaK3(SO4)2
Aragonite	-0.15	1.67	1.82	CaCO3
Arcanite	-11.69	-13.41	-1.72	K2SO4
Artinite	-7.70	11.17	18.87	Mg2CO3(OH)2:3H2O
B	-53.97	51.97	105.94	B
B(g)	-142.04	51.97	194.01	B
B2O3	-10.50	-5.05	5.45	B2O3
Ba	-92.82	43.76	136.58	Ba
Ba(OH)2:8H2O	-16.96	7.21	24.17	Ba(OH)2:8H2O
Ba2Si3O8	-18.68	3.99	22.67	Ba2Si3O8
Ba2SiO4	-31.95	11.24	43.19	Ba2SiO4
Ba2U2O7	-55.84	-20.77	35.08	Ba2U2O7
Ba3UO6	-85.57	5.57	91.15	Ba3UO6
BaCl2	-8.20	-6.06	2.14	BaCl2
BaCl2:2H2O	-6.40	-6.11	0.29	BaCl2:2H2O
BaCl2:H2O	-6.91	-6.08	0.83	BaCl2:H2O
BaMnO4	-79.42	-89.51	-10.09	BaMnO4
BaO	-38.82	7.43	46.26	BaO
Barite	-4.62	-14.50	-9.88	BaSO4
Barytocalcite	-2.84	-0.10	2.74	BaCa(CO3)2
BaS	-18.23	-2.52	15.71	BaS
Bassanite	-7.24	-11.07	-3.82	CaSO4:0.5H2O
BaU2O7	-46.86	-26.02	20.84	BaU2O7
BaUO4	-26.72	-9.29	17.42	BaUO4
Beidellite-Ca	1.82	6.32	4.50	Ca.165Al2.33Si3.67O10(OH)2
Beidellite-H	0.93	4.52	3.59	H.33Al2.33Si3.67O10(OH)2
Beidellite-K	1.64	5.93	4.28	K.33Al2.33Si3.67O10(OH)2
Beidellite-Mg	1.77	6.21	4.44	Mg.165Al2.33Si3.67O10(OH)2
Beidellite-Na	2.08	6.67	4.59	Na.33Al2.33Si3.67O10(OH)2
Birnessite	-168.78	-254.35	-85.56	Mn8O14:5H2O

```
  Bischofite       -7.78     -3.40     4.38  MgCl2:6H2O
  Bixbyite        -28.53    -30.58    -2.05  Mn2O3
  Bloedite        -18.21    -20.70    -2.49  Na2Mg(SO4)2:4H2O
  Boehmite          0.75      7.65     6.90  AlO2H
  Boltwoodite     -31.01    -16.13    14.88  K(H3O)(UO2)SiO4
  Boltwoodite-Na  -29.15    -14.58    14.57  Na.7K.3(H3O)(UO2)SiO4:H2O
  Borax            -9.80      2.68    12.49  Na2(B4O5(OH)4):8H2O
  Boric_acid       -2.52     -2.56    -0.04  B(OH)3
  Brucite          -5.43     10.21    15.65  Mg(OH)2
  Bunsenite        -5.15      6.74    11.89  NiO
  Burkeite        -23.47    -13.98     9.49  Na6CO3(SO4)2
  C                 1.54     63.45    61.91  C
  C(g)           -112.01     63.45   175.46  C
  Ca              -87.94     47.21   135.15  Ca
  Ca(g)          -112.17     47.21   159.38  Ca
  Ca-Al_Pyroxene  -11.25     22.58    33.83  CaAl2SiO6
  Ca2Al2O5:8H2O   -22.65     36.89    59.54  Ca2Al2O5:8H2O
  Ca2Cl2(OH)2:H2O -18.07      8.22    26.28  Ca2Cl2(OH)2:H2O
  Ca3Al2O6        -60.32     47.97   108.29  Ca3Al2O6
  Ca4Al2Fe2O10    -77.55     56.44   133.99  Ca4Al2Fe2O10
  Ca4Al2O7:13H2O  -48.68     58.52   107.20  Ca4Al2O7:13H2O
  Ca4Al2O7:19H2O  -45.24     58.37   103.61  Ca4Al2O7:19H2O
  Ca4Cl2(OH)6:13H2O -38.65     29.63    68.28  Ca4Cl2(OH)6:13H2O
  CaAl2O4         -18.21     26.21    44.41  CaAl2O4
  CaAl2O4:10H2O   -12.00     25.96    37.96  CaAl2O4:10H2O
  CaAl4O7         -22.96     41.53    64.50  CaAl4O7
  Calcite          -0.00      1.67     1.67  CaCO3
  Carnallite      -10.15     -5.89     4.26  KMgCl3:6H2O
  CaSO4:0.5H2O(beta)  -7.40    -11.07    -3.67  CaSO4:0.5H2O
  CaUO4           -21.03     -5.85    15.18  CaUO4
  Celadonite        0.76      7.63     6.87  KMgAlSi4O10(OH)2
  Celestite        -6.83    -12.60    -5.77  SrSO4
  Cerussite        -2.18     -5.34    -3.16  PbCO3
  CH4(g)           -0.20     -3.11    -2.91  CH4
  Chalcedony       -0.05     -3.63    -3.58  SiO2
  Chamosite-7A     -0.94     29.72    30.67  Fe2Al2SiO5(OH)4
  Chloromagnesite -24.16     -3.25    20.90  MgCl2
  Chrysotile       -6.36     23.42    29.78  Mg3Si2O5(OH)4
  Cl2(g)          -52.50    -49.82     2.68  Cl2
  Clinochlore-14A  -7.99     55.54    63.54  Mg5Al2Si3O10(OH)8
  Clinochlore-7A  -11.29     55.54    66.84  Mg5Al2Si3O10(OH)8
  Clinoptilolite    2.83     -7.67   -10.49
Na.954K.543Ca.761Mg.124Sr.036Ba.062Mn.002Al3.45Fe.017Si14.533O46.922H21.84
4
  Clinoptilolite-Ca   0.33     -7.69    -8.03
Ca1.7335Al3.45Fe.017Si14.533O36:10.922H2O
  Clinoptilolite-dehy -31.12     -7.39    23.72
Sr.036Mg.124Ca.761Mn.002Ba.062K.543Na.954Al3.45Fe.017Si14.533O36
  Clinoptilolite-dehy-Ca -33.63     -7.42    26.21
Ca1.7335Al3.45Fe.017Si14.533O36
  Clinoptilolite-dehy-K -34.57    -11.51    23.06
K3.467Al3.45Fe.017Si14.533O36
  Clinoptilolite-dehy-Na -30.20     -3.70    26.51
Na3.467Al3.45Fe.017Si14.533O36
  Clinoptilolite-dehy-NH4 -35.75    -42.61    -6.86
(NH4)3.467Al3.45Fe.017Si14.533O36
  Clinoptilolite-dehy-Sr -36.20    -10.10    26.10
Sr1.7335Al3.45Fe.017Si14.533O36
  Clinoptilolite-hy-Ca   0.26     -7.71    -7.97
Ca1.7335Al3.45Fe.017Si14.533O36:11.645H2O
```

```
  Clinoptilolite-hy-K  -0.34    -11.70  -11.36
K3.467Al3.45Fe.017Si14.533O36:7.499H2O
  Clinoptilolite-hy-Na   3.75     -3.97   -7.72
Na3.467Al3.45Fe.017Si14.533O36:10.877H2O
  Clinoptilolite-hy-Sr  -2.51    -10.45   -7.93
Sr1.7335Al3.45Fe.017Si14.533O36:13.893H2O
  Clinoptilolite-K  -0.64    -11.79  -11.15
K3.467Al3.45Fe.017Si14.533O36:10.922H2O
  Clinoptilolite-Na   3.74     -3.97   -7.71
Na3.467Al3.45Fe.017Si14.533O36:10.922H2O
  Clinoptilolite-NH4  -0.36    -42.88  -42.52
(NH4)3.467Al3.45Fe.017Si14.533O36:10.922H2O
  Clinoptilolite-Sr  -2.25    -10.37   -8.12
Sr1.7335Al3.45Fe.017Si14.533O36:10.922H2O
  Clinozoisite     -6.61     33.86   40.47  Ca2Al3Si3O12(OH)
  CO(g)            -9.92    -12.97   -3.05  CO
  CO2(g)           -1.31     -9.21   -7.89  CO2
  Coesite          -0.57     -3.63   -3.06  SiO2
  Coffinite        -8.85    -17.20   -8.35  USiO4
  Colemanite      -15.03      6.49   21.52  Ca2B6O11:5H2O
  Cordierite_anhyd -15.48     33.00   48.48  Mg2Al4Si5O18
  Cordierite_hydr -13.11     32.97   46.09  Mg2Al4Si5O18:H2O
  Corundum         -1.47     15.33   16.80  Al2O3
  Cotunnite        -4.92     -9.63   -4.71  PbCl2
  Cristobalite(alpha)  -0.31     -3.63   -3.31  SiO2
  Cristobalite(beta)  -0.73     -3.63   -2.90  SiO2
  Cronstedtite-7A  -2.77     11.99   14.76  Fe2Fe2SiO5(OH)4
  Daphnite-14A      0.41     49.53   49.12  Fe5AlAlSi3O10(OH)8
  Daphnite-7A      -2.88     49.53   52.41  Fe5AlAlSi3O10(OH)8
  Dawsonite         1.04      4.95    3.91  NaAlCO3(OH)2
  Diaspore          1.14      7.65    6.51  AlHO2
  Dicalcium_silicate -17.75     18.13   35.88  Ca2SiO4
  Diopside         -6.25     13.87   20.12  CaMgSi2O6
  Dolomite          0.58      2.71    2.12  CaMg(CO3)2
  Dolomite-dis     -0.89      2.71    3.59  CaMg(CO3)2
  Dolomite-ord      0.59      2.71    2.12  CaMg(CO3)2
  Enstatite        -4.20      6.61   10.81  MgSiO3
  Epidote          -5.56     24.99   30.55  Ca2FeAl2Si3O12OH
  Epidote-ord      -5.55     24.99   30.54  FeCa2Al2(OH)(SiO4)3
  Epsomite         -9.89    -11.87   -1.98  MgSO4:7H2O
  Ettringite      -46.24     14.01   60.25  Ca6Al2(SO4)3(OH)12:26H2O
  Fayalite         -3.74     14.45   18.19  Fe2SiO4
  Fe              -11.53     45.36   56.90  Fe
  Fe(OH)2          -4.34      9.01   13.35  Fe(OH)2
  Fe(OH)3          -6.39     -1.24    5.15  Fe(OH)3
  Fe2(SO4)3       -69.79    -68.20    1.58  Fe2(SO4)3
  FeO              -3.88      9.04   12.92  FeO
  Ferrite-Ca      -11.50      8.47   19.98  CaFe2O4
  Ferrite-Dicalcium -34.73     19.35   54.08  Ca2Fe2O5
  Ferrite-Mg      -11.58      7.83   19.41  MgFe2O4
  Ferrite-Zn       -6.47      3.93   10.40  ZnFe2O4
  Ferrosilite      -1.66      5.41    7.08  FeSiO3
  FeSO4           -15.08    -12.90    2.18  FeSO4
  Fix_H+           -6.72     -6.72    0.00  H+
  Forsterite       -9.78     16.85   26.63  Mg2SiO4
  Foshagite       -31.13     32.60   63.73  Ca4Si3O9(OH)2:0.5H2O
  Galena            8.29     -6.09  -14.38  PbS
  Gaylussite       -5.78      5.37   11.15  CaNa2(CO3)2:5H2O
  Gehlenite       -19.96     33.46   53.42  Ca2Al2SiO7
  Gibbsite          0.48      7.63    7.15  Al(OH)3
  Gismondine       -3.99     37.68   41.67  Ca2Al4Si4O16:9H2O
```

Glauberite	-14.49	-19.96	-5.47	Na2Ca(SO4)2
Goethite	-1.39	-1.22	0.18	FeOOH
Greenalite	-1.82	19.81	21.63	Fe3Si2O5(OH)4
Grossular	-12.21	37.09	49.30	Ca3Al2(SiO4)3
Gypsum	-6.55	-11.10	-4.56	CaSO4:2H2O
Gyrolite	-11.50	10.82	22.31	Ca2Si3O7(OH)2:1.5H2O
H2(g)	-5.10	-8.22	-3.12	H2
H2O(g)	-1.36	-0.02	1.33	H2O
H2S(g)	-2.01	-9.98	-7.97	H2S
Haiweeite	-37.39	-44.45	-7.06	Ca(UO2)2(Si2O5)3:5H2O
Halite	-1.81	-0.23	1.58	NaCl
Hatrurite	-41.86	29.01	70.87	Ca3SiO5
Hausmannite	-31.87	-23.26	8.62	Mn3O4
HCl(g)	-12.63	-6.76	5.87	HCl
Heazlewoodite	10.02	36.65	26.63	Ni3S2
Hedenbergite	-6.15	12.66	18.81	CaFe(SiO3)2
Hematite	-1.74	-2.41	-0.67	Fe2O3
Hercynite	-2.46	24.36	26.82	FeAl2O4
Heulandite	0.69	3.20	2.51	Ba.065Sr.175Ca.585K.132Na.383Al2.165Si6.835O18:6H2O
Hexahydrite	-10.10	-11.84	-1.74	MgSO4:6H2O
Hillebrandite	-17.50	18.10	35.61	Ca2SiO3(OH)2:0.17H2O
Huntite	-4.46	4.77	9.23	CaMg3(CO3)4
Hydroboracite	-14.54	5.82	20.37	MgCaB6O11:6H2O
Hydrocerussite	-8.68	-6.84	1.84	Pb3(CO3)2(OH)2
Hydromagnesite	-14.76	14.25	29.00	Mg5(CO3)4(OH)2:4H2O
Hydrophilite	-13.89	-2.61	11.27	CaCl2
Hydrozincite	-17.10	13.19	30.29	Zn5(OH)6(CO3)2
Ice	-0.20	-0.02	0.18	H2O
Illite	2.14	10.02	7.88	K0.6Mg0.25Al1.8Al0.5Si3.5O10(OH)2
Jadeite	-0.90	6.93	7.82	NaAl(SiO3)2
Jarosite	-32.78	-43.29	-10.51	KFe3(SO4)2(OH)6
Jarosite-Na	-35.57	-41.04	-5.46	NaFe3(SO4)2(OH)6
K	-46.32	22.42	68.75	K
K(g)	-56.42	22.42	78.84	K
K-Feldspar	1.57	1.04	-0.53	KAlSi3O8
K2CO3:1.5H2O	-14.10	-0.72	13.37	K2CO3:1.5H2O
K2O	-73.09	8.52	81.61	K2O
K2UO4	-41.09	-8.21	32.88	K2UO4
K3H(SO4)2	-27.48	-31.10	-3.62	K3H(SO4)2
K8H4(CO3)6:3H2O	-48.98	-21.28	27.70	K8H4(CO3)6:3H2O
Kainite	-13.94	-14.26	-0.32	KMgClSO4:3H2O
KAl(SO4)2	-34.40	-31.94	2.46	KAl(SO4)2
Kalicinite	-5.24	-4.96	0.28	KHCO3
Kalsilite	-1.93	8.30	10.23	KAlSiO4
Kaolinite	2.19	8.02	5.84	Al2Si2O5(OH)4
Kasolite	-23.76	-16.51	7.24	Pb(UO2)SiO4:H2O
Katoite	-31.10	47.82	78.91	Ca3Al2H12O12
Kieserite	-11.45	-11.72	-0.27	MgSO4:H2O
KMgCl3	-26.23	-5.74	20.49	KMgCl3
KMgCl3:2H2O	-19.31	-5.79	13.52	KMgCl3:2H2O
KNaCO3:6H2O	-8.82	1.42	10.24	KNaCO3:6H2O
Kyanite	-2.58	11.70	14.28	Al2SiO5
Lanarkite	-13.59	-14.20	-0.61	Pb2(SO4)O
Lansfordite	-3.92	0.91	4.83	MgCO3:5H2O
Larnite	-18.99	18.13	37.12	Ca2SiO4
Laumontite	-0.83	11.60	12.43	CaAl2Si4O12:4H2O
Lawrencite	-13.02	-4.46	8.56	FeCl2
Lawsonite	-1.79	18.90	20.69	CaAl2Si2O7(OH)2:H2O
Leonite	-21.08	-25.21	-4.12	K2Mg(SO4)2:4H2O

Lime	-20.59	10.88	31.47	CaO
Litharge	-8.40	3.87	12.26	PbO
Magnesite	-0.98	1.03	2.02	MgCO3
Magnetite	-2.54	6.63	9.17	Fe3O4
Manganite	-15.13	-15.30	-0.17	MnO(OH)
Manganosite	-9.90	7.32	17.23	MnO
Margarite	-3.67	34.25	37.93	CaAl4Si2O10(OH)2
Massicot	-8.57	3.87	12.43	PbO
Maximum_Microcline	1.57	1.04	-0.53	KAlSi3O8
Mayenite	-233.21	237.84	471.05	Ca12Al14O33
Melanterite	-10.71	-13.07	-2.36	FeSO4:7H2O
Mercallite	-16.25	-17.69	-1.44	KHSO4
Merwinite	-30.32	35.63	65.95	MgCa3(SiO4)2
Mesolite	3.38	15.82	12.44	Na.676Ca.657Al1.99Si3.01O10:2.647H2O
Mg	-71.71	46.57	118.28	Mg
Mg(g)	-90.60	46.57	137.17	Mg
Mg1.25SO4(OH)0.5:0.5H2O	-13.78	-9.15	4.63	Mg1.25SO4(OH)0.5:0.5H2O
Mg1.5SO4(OH)	-15.07	-6.59	8.48	Mg1.5SO4(OH)
MgCl2:2H2O	-15.50	-3.30	12.19	MgCl2:2H2O
MgCl2:4H2O	-10.39	-3.35	7.03	MgCl2:4H2O
MgCl2:H2O	-18.66	-3.28	15.38	MgCl2:H2O
MgOHCl	-11.73	3.48	15.21	MgOHCl
MgSO4	-16.00	-11.69	4.30	MgSO4
MgUO4	-28.34	-6.49	21.86	MgUO4
Millerite	4.78	-3.21	-7.99	NiS
Minium	-55.16	-38.91	16.25	Pb3O4
Minnesotaite	-0.63	12.58	13.22	Fe3Si4O10(OH)2
Mirabilite	-8.44	-9.15	-0.71	Na2SO4:10H2O
Misenite	-108.45	-119.53	-11.08	K8H6(SO4)7
Mn	-36.44	43.65	80.08	Mn
Mn(OH)2(am)	-7.46	7.30	14.76	Mn(OH)2
Mn(OH)3	-21.66	-15.33	6.33	Mn(OH)3
MnCl2:2H2O	-10.02	-6.22	3.80	MnCl2:2H2O
MnCl2:4H2O	-8.96	-6.27	2.68	MnCl2:4H2O
MnCl2:H2O	-11.45	-6.20	5.25	MnCl2:H2O
MnO2(gamma)	-28.68	-44.81	-16.13	MnO2
MnSO4	-16.84	-14.61	2.23	MnSO4
Molysite	-34.03	-21.44	12.59	FeCl3
Monohydrocalcite	-0.91	1.65	2.56	CaCO3:H2O
Monticellite	-10.92	17.49	28.41	CaMgSiO4
Montmor-Ca	1.69	3.44	1.75	Ca.165Mg.33Al1.67Si4O10(OH)2
Montmor-K	1.59	3.05	1.47	K.33Mg.33Al1.67Si4O10(OH)2
Montmor-Mg	1.71	3.34	1.63	Mg.495Al1.67Si4O10(OH)2
Montmor-Na	2.02	3.80	1.78	Na.33Mg.33Al1.67Si4O10(OH)2
Mordenite	-0.44	-5.73	-5.29	Ca.2895Na.361Al.94Si5.06O12:3.468H2O
Mordenite-dehy	-14.90	-5.64	9.26	Ca.2895Na.361Al.94Si5.06O12
Morenosite	-13.35	-15.36	-2.02	NiSO4:7H2O
Muscovite	4.30	16.35	12.04	KAl3Si3O10(OH)2
N2(g)	-2.52	-5.75	-3.23	N2
Na	-40.53	24.68	65.21	Na
Na(g)	-53.41	24.68	78.09	Na
Na2CO3	-7.11	3.82	10.93	Na2CO3
Na2CO3:7H2O	-6.45	3.65	10.10	Na2CO3:7H2O
Na2O	-52.39	13.03	65.42	Na2O
Na2SiO3	-12.33	9.40	21.73	Na2SiO3
Na2U2O7	-42.03	-20.42	21.61	Na2U2O7
Na2UO4(alpha)	-32.72	-3.70	29.03	Na2UO4
Na3H(SO4)2	-23.44	-24.33	-0.89	Na3H(SO4)2
Na3UO4	-52.84	1.73	54.57	Na3UO4

Na4Ca(SO4)3:2H2O	-23.01	-28.91	-5.90	Na4Ca(SO4)3:2H2O
Na4SiO4	-46.30	22.43	68.73	Na4SiO4
Na4UO2(CO3)3	-22.32	-18.29	4.04	Na4UO2(CO3)3
Na6Si2O7	-67.01	31.84	98.84	Na6Si2O7
NaFeO2	-13.64	5.31	18.95	NaFeO2
Nahcolite	-2.65	-2.70	-0.05	NaHCO3
Natrolite	0.12	17.43	17.31	Na2Al2Si3O10:2H2O
Natron	-6.28	3.57	9.85	Na2CO3:10H2O
Natrosilite	-11.99	5.78	17.77	Na2Si2O5
NaUO3	-19.31	-11.30	8.01	NaUO3
Nepheline	-2.42	10.55	12.98	NaAlSiO4
Nesquehonite	-4.09	0.96	5.05	MgCO3:3H2O
NH3(g)	-6.29	-4.70	1.60	NH3
Ni	-6.00	43.07	49.07	Ni
Ni(OH)2	-5.48	6.72	12.20	Ni(OH)2
Ni2SiO4	-3.69	9.86	13.56	Ni2SiO4
Nickelbischofite	-10.05	-6.90	3.15	NiCl2:6H2O
NiCl2	-14.88	-6.75	8.13	NiCl2
NiCl2:2H2O	-10.50	-6.80	3.70	NiCl2:2H2O
NiCl2:4H2O	-10.60	-6.85	3.75	NiCl2:4H2O
NiCO3	-5.97	-2.46	3.51	NiCO3
NiSO4	-19.94	-15.19	4.75	NiSO4
NiSO4:6H2O(alpha)	-13.33	-15.34	-2.00	NiSO4:6H2O
Niter	-85.83	-85.86	-0.03	KNO3
Nitrobarite	-170.53	-172.80	-2.27	Ba(NO3)2
NO(g)	-50.73	-50.31	0.42	NO
NO2(g)	-79.68	-71.95	7.73	NO2
Nontronite-Ca	0.56	-11.42	-11.97	Ca.165Fe2Al.33Si3.67H2O12
Nontronite-H	-0.33	-13.21	-12.89	H.33Fe2Al.33Si3.67H2O12
Nontronite-K	0.38	-11.80	-12.19	K.33Fe2Al.33Si3.67H2O12
Nontronite-Mg	0.51	-11.52	-12.03	Mg.165Fe2Al.33Si3.67H2O12
Nontronite-Na	0.82	-11.06	-11.88	Na.33Fe2Al.33Si3.67H2O12
O2(g)	-69.70	-72.65	-2.96	O2
Okenite	-6.62	3.58	10.19	CaSi2O4(OH)2:H2O
Oxychloride-Mg	-12.22	13.59	25.81	Mg2Cl(OH)3:4H2O
Paragonite	2.81	18.60	15.79	NaAl3Si3O10(OH)2
Paralaurionite	-3.14	-2.89	0.24	PbClOH
Pargasite	-26.22	70.44	96.65	NaCa2Al3Mg4Si6O22(OH)2
Pb	-5.39	40.19	45.58	Pb
Pb(g)	-32.72	40.19	72.91	Pb
Pb(N3)2(mono)	-119.72	-127.68	-7.96	Pb(N3)2
Pb(N3)2(orth)	-119.29	-127.68	-8.39	Pb(N3)2
Pb2Cl2CO3	-5.35	-14.97	-9.62	Pb2Cl2CO3
Pb2Cl5NH4	-11.75	-30.71	-18.96	Pb2Cl5NH4
Pb2O(N3)2	-110.10	-123.81	-13.71	Pb2O(N3)2
Pb2SiO4	-13.42	4.10	17.53	Pb2SiO4
Pb3SO6	-20.46	-10.34	10.12	Pb3SO6
Pb4Cl2(OH)6	-15.37	1.89	17.26	Pb4Cl2(OH)6
Pb4SO7	-27.40	-6.47	20.93	Pb4SO7
PbCO3.PbO	-10.82	-1.48	9.35	PbCO3.PbO
PbSO4(NH3)2	-25.59	-27.46	-1.88	PbSO4(NH3)2
PbSO4(NH3)4	-38.52	-36.86	1.67	PbSO4(NH3)4
Pentahydrite	-10.42	-11.82	-1.40	MgSO4:5H2O
Periclase	-10.23	10.24	20.47	MgO
Phlogopite	-3.78	31.74	35.51	KAlMg3Si3O10(OH)2
Phosgenite	-5.59	-14.97	-9.38	Pb2(CO3)Cl2
Picromerite	-20.80	-25.26	-4.45	K2Mg(SO4)2:6H2O
Pirssonite	-5.87	5.45	11.32	Na2Ca(CO3)2:2H2O
Plattnerite	-38.67	-46.64	-7.97	PbO2
Polydymite	24.12	-23.89	-48.02	Ni3S4
Polyhalite	-32.95	-47.26	-14.32	K2MgCa2(SO4)4:2H2O

```
  Portlandite     -10.96     10.85   21.81  Ca(OH)2
  Prehnite         -4.81     26.18   31.00  Ca2Al2Si3O10(OH)2
  Pseudowollastonite  -6.25      7.25   13.51  CaSiO3
  Pyrite           10.22    -13.87  -24.09  FeS2
  Pyrolusite      -27.61    -44.81  -17.20  MnO2
  Pyrophyllite      1.11      0.80   -0.31  Al2Si4O10(OH)2
  Pyrrhotite        2.87     -0.92   -3.79  FeS
  Quartz            0.22     -3.63   -3.84  SiO2
  Rankinite       -24.70     25.39   50.09  Ca3Si2O7
  Rhodochrosite    -1.54     -1.88   -0.34  MnCO3
  Rhodonite        -5.62      3.70    9.32  MnSiO3
  Ripidolite-14A   -4.35     53.14   57.49  Mg3Fe2Al2Si3O10(OH)8
  Ripidolite-7A    -7.65     53.14   60.79  Mg3Fe2Al2Si3O10(OH)8
  Rutherfordine   -21.70    -25.93   -4.23  UO2CO3
  S                -2.67    -46.28  -43.61  S
  S2(g)           -18.50    -25.90   -7.40  S2
  Sanbornite       -9.04      0.18    9.22  BaSi2O5
  Sanidine_high     0.44      1.04    0.61  KAlSi3O8
  Saponite-Ca      -3.23     21.71   24.94  Ca.165Mg3Al.33Si3.67O10(OH)2
  Saponite-H       -4.12     19.91   24.03  H.33Mg3Al.33Si3.67O10(OH)2
  Saponite-K       -3.41     21.32   24.73  K.33Mg3Al.33Si3.67O10(OH)2
  Saponite-Mg      -3.28     21.60   24.88  Mg3.165Al.33Si3.67O10(OH)2
  Saponite-Na      -2.97     22.06   25.03  Na.33Mg3Al.33Si3.67O10(OH)2
  Scacchite       -14.49     -6.17    8.31  MnCl2
  Schoepite       -21.32    -16.78    4.54  UO3:2H2O
  Schoepite-dehy(.393) -23.07    -16.74    6.33  UO3:.393H2O
  Schoepite-dehy(.648) -22.58    -16.74    5.83  UO3:.648H2O
  Schoepite-dehy(.85) -21.52    -16.75    4.78  UO3:.85H2O
  Schoepite-dehy(.9) -21.45    -16.75    4.70  UO3:.9H2O
  Schoepite-dehy(1.0) -21.53    -16.75    4.78  UO3:H2O
  Scolecite         0.70     15.25   14.56  CaAl2Si3O10:3H2O
  Sepiolite       -10.27     19.03   29.30  Mg4Si6O15(OH)2:6H2O
  Si              -74.90     69.03  143.93  Si
  Si(g)          -143.43     69.03  212.46  Si
  Siderite          0.24     -0.17   -0.41  FeCO3
  Sillimanite      -3.18     11.70   14.88  Al2SiO5
  SiO2(am)         -1.00     -3.63   -2.63  SiO2
  Sklodowskite    -44.41    -30.64   13.77  Mg(H3O)2(UO2)2(SiO4)2:4H2O
  Smectite-high-Fe-Mg  -1.42     14.69   16.11
Ca.025Na.1K.2Fe.5Fe.2Mg1.15Al1.25Si3.5H2O12
  Smectite-low-Fe-Mg  -0.40      9.65   10.05
Ca.02Na.15K.2Fe.29Fe.16Mg.9Al1.25Si3.75H2O12
  Smithsonite      -3.14     -2.87    0.27  ZnCO3
  SO2(g)          -21.45    -21.42    0.03  SO2
  Soddyite        -37.51    -37.13    0.38  (UO2)2SiO4:2H2O
  Sphalerite        7.65     -3.62  -11.27  ZnS
  Spinel           -9.77     25.57   35.33  Al2MgO4
  Sr              -91.38     45.66  137.04  Sr
  Sr(NO3)2       -172.11   -170.90    1.22  Sr(NO3)2
  Sr(NO3)2:4H2O  -171.95   -171.00    0.96  Sr(NO3)2:4H2O
  Sr(OH)2         -17.34      9.31   26.65  Sr(OH)2
  Sr2SiO4         -26.32     15.04   41.36  Sr2SiO4
  SrCl2           -11.74     -4.16    7.58  SrCl2
  SrCl2:2H2O       -7.38     -4.21    3.17  SrCl2:2H2O
  SrCl2:6H2O       -5.93     -4.31    1.63  SrCl2:6H2O
  SrCl2:H2O        -8.72     -4.18    4.53  SrCl2:H2O
  SrO             -31.16      9.33   40.49  SrO
  SrS             -14.78     -0.62   14.16  SrS
  SrSiO3           -8.64      5.71   14.35  SrSiO3
  SrUO4(alpha)    -25.68     -7.39   18.29  SrUO4
  Starkeyite      -10.78    -11.79   -1.01  MgSO4:4H2O
```

Stilbite	3.50	3.79	0.29	Ca1.019Na.136K.006Al2.18Si6.82O18:7.33H2O
Strontianite	0.52	0.13	-0.39	SrCO3
Sylvite	-3.41	-2.49	0.92	KCl
Syngenite	-16.89	-24.49	-7.60	K2Ca(SO4)2:H2O
Tachyhydrite	-26.54	-9.42	17.11	Mg2CaCl6:12H2O
Talc	-3.94	16.19	20.13	Mg3Si4O10(OH)2
Tephroite	-11.09	11.02	22.11	Mn2SiO4
Thenardite	-8.52	-8.90	-0.38	Na2SO4
Thermonatrite	-6.98	3.80	10.78	Na2CO3:H2O
Tobermorite-11A	-31.22	32.50	63.72	Ca5Si6H11O22.5
Tobermorite-14A	-29.87	32.38	62.25	Ca5Si6H21O27.5
Tobermorite-9A	-34.38	32.57	66.95	Ca5Si6H6O20
Todorokite	-142.90	-188.75	-45.85	Mn7O12:3H2O
Tremolite	-14.67	43.92	58.59	Ca2Mg5Si8O22(OH)2
Trevorite	-4.21	4.34	8.55	NiFe2O4
Tridymite	0.04	-3.63	-3.66	SiO2
Troilite	2.97	-0.92	-3.89	FeS
Trona-K	-15.02	-3.44	11.58	K2NaH(CO3)2:2H2O
U	-113.18	92.25	205.44	U
U(CO3)2	-38.53	-31.99	6.55	U(CO3)2
U(g)	-195.71	92.25	287.97	U
U(OH)2SO4	-32.45	-35.53	-3.08	U(OH)2SO4
U(SO3)2	-38.31	-74.97	-36.66	U(SO3)2
U(SO4)2	-45.32	-57.44	-12.12	U(SO4)2
U(SO4)2:4H2O	-45.58	-57.54	-11.96	U(SO4)2:4H2O
U(SO4)2:8H2O	-44.86	-57.64	-12.78	U(SO4)2:8H2O
U2C3	-189.64	249.56	439.20	U2C3
U2Cl10(g)	-182.20	-103.10	79.10	U2Cl10
U2Cl8(g)	-158.98	-81.12	77.86	U2Cl8
U2O2Cl5	-82.84	-65.12	17.72	U2O2Cl5
U2S3	-85.25	-79.63	5.62	U2S3
U3S5	-111.48	-113.11	-1.63	U3S5
U5O12Cl	-76.99	-95.83	-18.84	U5O12Cl
UC	-94.88	93.06	187.94	UC
UC1.94(alpha)	-95.39	152.70	248.09	UC1.94
UCl(g)	-165.88	48.09	213.97	UCl
UCl2(g)	-134.60	42.43	177.03	UCl2
UCl3	-57.36	-45.12	12.23	UCl3
UCl3(g)	-101.11	-45.12	55.99	UCl3
UCl4	-61.09	-40.56	20.53	UCl4
UCl4(g)	-84.38	-40.56	43.82	UCl4
UCl5	-87.34	-51.55	35.79	UCl5
UCl5(g)	-103.67	-51.55	52.12	UCl5
UCl6	-112.50	-57.21	55.29	UCl6
UCl6(g)	-117.92	-57.21	60.71	UCl6
UH3(beta)	-108.87	84.06	192.93	UH3
UN	-69.69	-29.54	40.15	UN
UN1.59(alpha)	-58.10	-21.05	37.06	UN1.59
UN1.73(alpha)	-55.66	-29.33	26.34	UN1.73
UO(g)	-148.19	55.93	204.12	UO
UO2(am)	-13.68	-13.57	0.10	UO2
UO2(g)	-101.32	19.60	120.92	UO2
UO2(NO3)2	-208.45	-196.96	11.49	UO2(NO3)2
UO2(NO3)2:2H2O	-201.76	-197.01	4.75	UO2(NO3)2:2H2O
UO2(NO3)2:3H2O	-200.65	-197.03	3.61	UO2(NO3)2:3H2O
UO2(NO3)2:6H2O	-199.49	-197.11	2.38	UO2(NO3)2:6H2O
UO2(NO3)2:H2O	-205.18	-196.98	8.19	UO2(NO3)2:H2O
UO2(OH)2(beta)	-21.37	-16.75	4.62	UO2(OH)2
UO2.25	-10.64	-15.70	-5.05	UO2.25
UO2.25(beta)	-10.72	-15.70	-4.98	UO2.25

UO2.3333(beta)	-23.38	-51.36	-27.98	(UO2.3333)2
UO2.6667	-32.26	-75.59	-43.33	(UO2.6667)2
UO2Cl	-23.91	-24.56	-0.66	UO2Cl
UO2Cl2	-41.70	-30.22	11.48	UO2Cl2
UO2Cl2(g)	-75.97	-30.22	45.75	UO2Cl2
UO2Cl2:3H2O	-35.64	-30.30	5.34	UO2Cl2:3H2O
UO2Cl2:H2O	-38.07	-30.25	7.83	UO2Cl2:H2O
UO2ClOH:2H2O	-25.65	-23.54	2.11	UO2ClOH:2H2O
UO2CO3	-21.69	-25.93	-4.24	UO2CO3
UO2SO3	-31.47	-47.42	-15.96	UO2SO3
UO2SO4	-40.10	-38.66	1.44	UO2SO4
UO2SO4:2.5H2O	-37.01	-38.72	-1.71	UO2SO4:2.5H2O
UO2SO4:3.5H2O	-37.10	-38.75	-1.65	UO2SO4:3.5H2O
UO2SO4:3H2O	-37.12	-38.73	-1.61	UO2SO4:3H2O
UO2SO4:H2O	-32.38	-38.68	-6.30	UO2SO4:H2O
UO3(alpha)	-24.87	-16.73	8.14	UO3
UO3(beta)	-24.55	-16.73	7.83	UO3
UO3(g)	-84.80	-16.73	68.07	UO3
UO3(gamma)	-23.97	-16.73	7.24	UO3
UO3:.9H2O(alpha)	-21.45	-16.75	4.70	UO3:.9H2O
UO3:2H2O	-21.32	-16.78	4.54	UO3:2H2O
UOCl	-41.38	-31.63	9.75	UOCl
UOCl2	-31.67	-27.07	4.60	UOCl2
UOCl3	-50.06	-38.06	12.00	UOCl3
Uraninite	-8.29	-13.57	-5.28	UO2
Uranophane	-47.13	-29.85	17.27	Ca(UO2)2(SiO3)2(OH)2
US	-61.47	-16.67	44.80	US
US1.9	-31.91	-34.75	-2.84	US1.9
US2	-30.52	-33.48	-2.96	US2
US3	-30.14	-46.59	-16.45	US3
Vaesite	9.99	-16.16	-26.15	NiS2
Wairakite	-4.89	11.65	16.54	CaAl2Si4O10(OH)4
Weeksite	-62.15	-46.79	15.36	K2(UO2)2(Si2O5)3:4H2O
Witherite	1.16	-1.77	-2.93	BaCO3
Wollastonite	-6.03	7.25	13.29	CaSiO3
Wurtzite	5.43	-3.62	-9.05	ZnS
Wustite	-4.35	7.47	11.82	Fe.947O
Xonotlite	-45.42	43.50	88.92	Ca6Si6O17(OH)2
Zincite	-4.36	6.34	10.69	ZnO
Zn	-23.66	42.66	66.32	Zn
Zn(BO2)2	-7.03	1.29	8.32	Zn(BO2)2
Zn(ClO4)2:6H2O	-334.35	-328.68	5.67	Zn(ClO4)2:6H2O
Zn(g)	-39.54	42.66	82.20	Zn
Zn(NO3)2:6H2O	-177.58	-174.05	3.54	Zn(NO3)2:6H2O
Zn(OH)2(beta)	-5.15	6.31	11.46	Zn(OH)2
Zn(OH)2(epsilon)	-4.88	6.31	11.19	Zn(OH)2
Zn(OH)2(gamma)	-5.57	6.31	11.88	Zn(OH)2
Zn2(OH)3Cl	-9.40	5.89	15.28	Zn2(OH)3Cl
Zn2SiO4	-4.12	9.04	13.17	Zn2SiO4
Zn2SO4(OH)2	-16.86	-9.29	7.58	Zn2SO4(OH)2
Zn3O(SO4)2	-42.47	-24.86	17.62	Zn3O(SO4)2
Zn5(NO3)2(OH)8	-191.30	-148.65	42.65	Zn5(NO3)2(OH)8
ZnCl2	-13.82	-7.16	6.66	ZnCl2
ZnCl2(NH3)2	-9.70	-16.55	-6.85	ZnCl2(NH3)2
ZnCl2(NH3)4	-19.56	-25.95	-6.39	ZnCl2(NH3)4
ZnCl2(NH3)6	-31.04	-35.34	-4.30	ZnCl2(NH3)6
ZnCO3:H2O	-3.03	-2.90	0.14	ZnCO3:H2O
ZnSO4	-18.67	-15.60	3.07	ZnSO4
ZnSO4:6H2O	-14.04	-15.75	-1.71	ZnSO4:6H2O
ZnSO4:7H2O	-13.97	-15.77	-1.81	ZnSO4:7H2O
ZnSO4:H2O	-14.82	-15.62	-0.81	ZnSO4:H2O

```
  Zoisite           -6.65     33.86   40.50  Ca2Al3(SiO4)3OH

**For a gas, SI = log10(fugacity). Fugacity = pressure * phi / 1 atm.
  For ideal gases, phi = 1.
```

Appendix VIII Flowchart